

# **ELECTRONIC STRUCTURE OF COMPLEX CRYSTALLINE SOLIDS**

Thesis submitted for the degree of  
Doctor of Philosophy (Science)

in

Physics (Theoretical)

by

**Soumyajit Sarkar**

Department of Physics  
University of Calcutta  
July 2012

To my wife

---

## Acknowledgments

This thesis represents not only my work at the keyboard, a great many people have contributed to its production. I owe my gratitude to all those people who have made this dissertation possible and because of whom my graduate experience has been nothing short of amazing, that I will cherish forever. I would like to express my sincere respect and deepest gratitude to my thesis supervisor Prof. Tanusri Saha-Dasgupta. I have always benefited from her expertise supervision, brilliant ideas, continuous enthusiasm and rigorous attitude to science. Her enthusiastic and integral view on research have made a deep impression on me. I would also like to thank Prof. Indra Dasgupta for valuable discussions, an active collaboration with him helped me to expand my area of research. I have also enjoyed an active collaboration with Prof. Peter Oppeneer of Uppasala University on 'Magnetism in organic materials', and Prof. Sumit Mazumdar of Arizona University on 'Theory of complex ternary oxides and chalcogenides', although this is out of the interest of the present thesis but it helped me to grow up. I cannot ever forget the wonderful hospitality during my visit in their respective departments. During these years of study I have experienced an excellent environment for research, here at S N Bose Centre, and for that I would like to thank our director Prof. Arup Kumar Raychaudhuri. I am grateful to all the staff members of our centre for their unconditional support and help in the hour of need.

I had the pleasure to work with some of the most vibrant group-mates, like Badiur-da, Soumendu-da, Hena-di, Swastika, Sudipta, Santu and Swarnakamal. I owe my deep gratitude to them, for their genuine interest, prompt response and skilful comments that greatly contributed to my research career. A special thanks goes to Swastika, for her kind help in almost all practical matters that gave me a tough time in academic front during these years. I thank Dr. Mukul Kabir, Dr. Kartick Tarafder and Dr. Molly De Raychaudhuri, who have always extended their help and taught me many things during the years of study. Being a student in the field of computational material sciences, computation facility has been added to the list of my basic needs, and I must thank our system administrator Sudeep for providing the *supply* to my ever increasing *demand* of computing hours.

My stay at S N Bose Centre, will remain memorable for me, as I found myself most of the time cheerful (although *ideally* that should be, but for a graduate student, *ideal/expected* things happen not so frequently!), and the credit for that goes to all my SNB friends. From the very first day, when we started together our journey as graduate student, Prashant, Kapil, Swastika, Sujoy, Kinshuk, Hirak and Abhinav have been a great company. As the days gone, this list kept on increasing. I thank all of them for all those happy moments they shared with me. Many of them inspired me in different ways. I wish I could be as informative as Arghya, as dedicated as Prashant, as charismatic as Abhinav, as gregarious as Sudip, as precise as Debraj and many more. The outstanding ability of Jena has always shown me the way to get rid of almost all the technical problems related to computer. A special thanks to Abhijit, Sandeep-ji, Rajiv, Sumit, Debmallya and Sandeep for adding vital colours to the spectrum. I shall miss all those weekend evenings spend with you all which are not worth mentioning here! I must not miss the opportunity to thank Tamoghna and Sayanko, two of my old friends in my home-town Chandannagar, who always stand behind me through all thick and thin.

I have an amazing family, unique in many ways, and the stereotype of a perfect family in many others. Their support has been unconditional all these years. I would like to express my heart-felt gratitude to my parents, *bhai*, *didi* and my in-laws. The most special thanks I accord my wife Soumita, for her

unwavering understanding during all these years, her selfless love and support throughout, and her encouragement and companionship during the preparation of this thesis.

Finally, I appreciate the financial support from Council of Scientific and Industrial Research (CSIR) and I would like to thank everybody who was important to the successful realization of thesis, as well as expressing my apology that I could not mention personally one by one.

Soumyajit Sarkar  
Kolkata, India  
July, 2012

---

## List of Publications

1. **S. Sarkar**, T. Maitra, Roser Valentí and T. Saha-Dasgupta  
*Proposed Orbital Ordering in  $MnV_2O_4$  From First-principles Calculations*  
**Phys. Rev. Lett.** **102**, 216405 (2009)\*
2. **Soumyajit Sarkar**, Molly De Raychaudhury and T. Saha-Dasgupta  
*Density-functional Study of Electronic and Optical properties of Spinel compound  $CuIr_2S_4$*   
**Phys. Rev. B** **79**, 113104 (2009)\*
3. **Soumyajit Sarkar**, Molly De Raychaudhury, I. Dasgupta and T. Saha-Dasgupta  
*Electronic structure of  $FeCr_2S_4$ : Evidence of Coulomb enhanced spin-orbit splitting*  
**Phys. Rev. B** **80**, 201101(R) (2009)\*
4. R.T. Clay, H. Li, **S. Sarkar**, S. Mazumdar and T. Saha-Dasgupta  
*Cooperative orbital ordering and Peierls instability in the checkerboard lattice with doubly degenerate orbitals*  
**Phys. Rev. B** **82**, 035108 (2010)
5. **S. Sarkar**, Roser Valentí, T. Maitra and T. Saha-Dasgupta  
*Comparative study of  $FeCr_2S_4$  and  $FeSc_2S_4$ : Spinels with orbitally active A site*  
**Phys. Rev. B** **82**, 041105(R) (2010)\*
6. **Soumyajit Sarkar**, Sudipta Kanungo and T. Saha-Dasgupta  
*Ab initio study of low-dimensional quantum spin systems  $Sr_3NiPtO_6$ ,  $Sr_3CuPtO_6$ , and  $Sr_3NiIrO_6$*   
**Phys. Rev. B** **82**, 235122 (2010)
7. E. Jacobi, S. Kanungo, **S. Sarkar**, S. Schmitt and T. Saha-Dasgupta  
*LDA+DMFT study of Ru-based perovskite  $SrRuO_3$  and  $CaRuO_3$*   
**Phys. Rev. B** **83**, 041103(R) (2011)
8. **Soumyajit Sarkar**, Kartick Tarafder, Peter M. Oppeneer and T. Saha-Dasgupta  
*Spin-Crossover in Cyanide-Based Bimetallic Coordination Polymers – Insight from First-Principles Calculations*  
**Journal of Materials Chemistry**, 2011, **21** (36), 13832-13840
9. **Soumyajit Sarkar**, Indra Dasgupta, Martha Greenblatt and T. Saha-Dasgupta  
*Electronic and Magnetic Structure of Bi-layer,  $La_3Ni_2O_6$ , and tri-layer,  $La_4Ni_3O_8$  Nickelates from First Principles*  
**Phys. Rev. B** **84**, 180411(R) (2011)
10. **Soumyajit Sarkar** and T. Saha-Dasgupta  
*Orbital ordering in  $FeV_2O_4$ : Spinel with two orbitally active site*  
**Phys. Rev. B** **84**, 235112 (2011)\*

11. Santu Baidya, **Soumyajit Sarkar**, T. Saha-Dasgupta and D. D. Sarma  
*Localized versus Itinerant Character of Pyrochlore Ruthenates:  $Tl_2Ru_2O_7$  versus  $Hg_2Ru_2O_7$*   
**Submitted to PRB (Rapid Communication)**
12. Swarnakamal Mukherjee, **Soumyajit Sarkar** and T. Saha-Dasgupta  
*First-principles study of  $CaCu_3B_4O_{12}$ , ( $B=Co, Rh, Ir$ )*  
**Accepted to Journal of Materials Science**

# Contents

<b>Table of Contents</b>	<b>vii</b>
<b>List of Figures</b>	<b>x</b>
<b>List of Tables</b>	<b>xii</b>
<b>1 Introduction</b>	<b>1</b>
1.1 Crystal Structure of Spinel Compounds . . . . .	2
1.2 Few Important Spinel Compounds . . . . .	7
1.3 First-Principles Studies on Spinel Compound . . . . .	9
1.4 Motivation and Overview of Present Thesis . . . . .	11
<b>2 Theoretical background of electronic structure calculations</b>	<b>19</b>
2.1 Density Functional Theory (DFT) way of solving quantum many body problem . . . . .	19
2.1.1 The many-electron Hamiltonian . . . . .	19
2.1.2 Wave function based approach . . . . .	20
2.1.3 Density functional theory . . . . .	21
2.1.3.1 Basic theorems of DFT and Kohn-Sham equation . . . . .	22
2.1.3.2 Exchange-correlation functional . . . . .	25
2.1.3.3 Basis sets . . . . .	27
2.2 Overview of band-structure methods . . . . .	27
2.2.1 The Linear Muffin-tin Orbital Method . . . . .	28
2.2.2 $N^{th}$ Order Muffin Tin Orbital (NMTO) - improved LMTO method . . . . .	30
2.2.3 The Pseudopotential Method . . . . .	32
2.2.4 The Linearized Augmented Plane Wave + local orbital method . . . . .	33
2.2.5 The Projector-Augmented-Wave Formalism . . . . .	36
<b>3 Proposed Orbital Ordering in <math>MnV_2O_4</math></b>	<b>41</b>
3.1 Background . . . . .	41
3.2 Motivation the present work . . . . .	42
3.3 Results and Discussions . . . . .	43
3.3.1 Structural Optimization . . . . .	43
3.3.2 Density of states and band structure . . . . .	45
3.3.3 NMTO-downfolding calculation . . . . .	46
3.3.4 Charge-density calculation . . . . .	48

---

3.3.5	Effect of spin-orbit interaction . . . . .	49
3.3.6	Magnetic exchange interaction and non-collinear spin arrangement . . . . .	49
3.4	Conclusion . . . . .	51
<b>4</b>	<b>Coulomb enhanced spin-orbit coupling driven insulating phase in <math>\text{FeCr}_2\text{S}_4</math></b>	<b>54</b>
4.1	Introduction . . . . .	54
4.2	Motivation of the present work . . . . .	55
4.3	Results and Discussions . . . . .	56
4.3.1	Crystal structure . . . . .	56
4.3.2	Density of states and energy level splitting within GGA . . . . .	56
4.3.3	Band structure beyond GGA . . . . .	58
4.3.4	Possible structural distortion at low temperature . . . . .	65
4.3.5	Computed optical conductivity and reflectivity . . . . .	67
4.4	Conclusion . . . . .	70
<b>5</b>	<b>Comparative study of two similar spinels : <math>\text{FeCr}_2\text{S}_4</math> and <math>\text{FeSc}_2\text{S}_4</math></b>	<b>73</b>
5.1	Introduction . . . . .	73
5.2	Motivation of the present work . . . . .	73
5.3	Results and Discussions . . . . .	75
5.3.1	Density of States . . . . .	75
5.3.2	Band structure . . . . .	77
5.3.3	Effective Fe-Fe interaction . . . . .	78
5.3.4	Effect of spin-orbit coupling . . . . .	82
5.4	Conclusion . . . . .	83
<b>6</b>	<b>Electronic and optical properties of spinel <math>\text{CuIr}_2\text{S}_4</math></b>	<b>86</b>
6.1	Introduction . . . . .	86
6.2	Motivation of the present work . . . . .	87
6.3	Results and Discussions . . . . .	89
6.3.1	Crystal structure . . . . .	89
6.3.2	Density of states . . . . .	89
6.3.3	Estimation of band gap and effect of Coulomb correlation . . . . .	91
6.3.4	Calculation of optical properties . . . . .	92
6.4	Conclusion . . . . .	95
<b>7</b>	<b>Orbital ordering in spinel compound with two orbitally active sites</b>	<b>98</b>
7.1	Introduction . . . . .	98
7.2	Motivation of the present work . . . . .	99
7.3	Crystal structure . . . . .	100
7.4	Results and Discussions . . . . .	101
7.4.1	Crystal field splitting . . . . .	102
7.4.2	Density of states within GGA . . . . .	103
7.4.3	Calculation within GGA+ $U$ . . . . .	104
7.4.4	Spin-Orbit interaction . . . . .	106
7.5	Conclusion . . . . .	109

---

<b>8</b>	<b>Conclusion and scope for future study</b>	<b>112</b>
8.1	Conclusion . . . . .	112
8.2	Scope for future work . . . . .	114

# List of Figures

1.1	Conventional unit cell of cubic spinel compound . . . . .	4
1.2	Projection of B-site sub-lattice of spinel compound on different planes . . . . .	6
1.3	A-site only sub-lattice of a spinel compound . . . . .	7
2.1	Approximated crystal potential within LMTO method . . . . .	28
2.2	Construction of Kink partial wave (KPW), $\phi$ , $\phi_0$ and $\varphi$ . . . . .	31
2.3	$N^{th}$ order approximation to the energy dependence of a partial wave for a discrete (La-grange) mesh. . . . .	31
3.1	VO <sub>6</sub> octahedral unit of optimized MnV <sub>2</sub> O <sub>4</sub> structure . . . . .	45
3.2	Partial DOS of V- $d$ states in MnV <sub>2</sub> O <sub>4</sub> . . . . .	46
3.3	Shape of five $d$ orbitals . . . . .	47
3.4	LSDA + $U$ band structure of MnV <sub>2</sub> O <sub>4</sub> . . . . .	47
3.5	Three-dimensional electron density plot of MnV <sub>2</sub> O <sub>4</sub> . . . . .	48
3.6	Schematic diagram of projection of V tetrahedron on xy plane with $xz$ and $yz$ orbitals occupying alternate V site. . . . .	50
3.7	Noncollinear spin arrangement of V spins in MnV <sub>2</sub> O <sub>4</sub> . . . . .	50
4.1	Schematic diagram showing expected half-metallic ground state of FeCr <sub>2</sub> S <sub>4</sub> . . . . .	55
4.2	Spin-polarized partial DOS of FeCr <sub>2</sub> S <sub>4</sub> calculated within GGA . . . . .	57

4.3	The energy levels of Fe and Cr $d$ levels in eV unit, calculated using NMTO downfolding technique. . . . .	58
4.4	Band structure of $\text{FeCr}_2\text{S}_4$ in the up-spin channel . . . . .	59
4.5	Splitting between Fe $z^2 - x^2$ and $3y^2 - r^2$ levels in eV plotted as function of $\phi$ . . . . .	64
4.6	Variation of Fe orbital moment and band gap as a function $U$ applied at Fe site . . . . .	65
4.7	A series of minimum-energy curves plotted against the variation of Cr position, for various choices of S movements . . . . .	67
4.8	Comparison of calculated reflectivity spectrum and experimentally measured spectrum . . . . .	69
5.1	Inverse susceptibility $1/\chi(T)$ of $\text{FeSc}_2\text{S}_4$ and $\text{FeCr}_2\text{S}_4$ . . . . .	74
5.2	Non spin-polarized total DOS calculated within GGA for $\text{FeSc}_2\text{S}_4$ and $\text{FeCr}_2\text{S}_4$ . . . . .	76
5.3	Spin-polarized band structure for $\text{FeCr}_2\text{S}_4$ and $\text{FeSc}_2\text{S}_4$ calculated within GGA . . . . .	77
5.4	Wannier function plot of Fe $d_{xy}$ orbital for $\text{FeCr}_2\text{S}_4$ and $\text{FeSc}_2\text{S}_4$ . . . . .	79
5.5	The NN and 2NN interaction path between Fe atoms . . . . .	79
5.6	A-site sub-lattice of spinel structure (diamond lattice) consisting of two interpenetrating face-centered cubic lattices . . . . .	80
6.1	A view of the 3D configuration of the Ir ions, emphasizing the orientation of the hexagonal rings perpendicular to the (111) cubic direction in $\text{CuIr}_2\text{S}_4$ . . . . .	87
6.2	The total and orbital projected DOS of $\text{CuIr}_2\text{S}_4$ for both the high temperature and low temperature phases . . . . .	90
6.3	The various allowed optical transitions for photonic energy in the high-temperature and low-temperature phases of $\text{CuIr}_2\text{S}_4$ . . . . .	92
6.4	Comparison of calculated reflectivity spectrum with experimental data . . . . .	93
6.5	Absorptive part of the calculated diagonal optical conductivity of $\text{CuIr}_2\text{S}_4$ at high-temperature and low-temperature phases, respectively . . . . .	94
7.1	Orbital degeneracy of octahedrally and tetrahedrally split $\text{Fe}^{2+}$ and $\text{V}^{3+}$ $d$ levels respectively in spinel compound . . . . .	99

---

7.2	The crystal structure of high-temperature and low-temperature tetragonal phase of $\text{FeV}_2\text{O}_4$	100
7.3	The crystal field splittings of Fe- $d$ and V- $d$ states of $\text{FeV}_2\text{O}_4$	102
7.4	GGA DOS projected onto Fe- $d$ (minority spin channel only) and V- $d$ states (majority spin channel only) for HT-T and LT-T	103
7.5	GGA + $U$ DOS projected onto Fe- $d$ and V- $d$ states for HT-T and LT-T	105
7.6	The plot of charge density calculated within GGA + $U$ , demonstrating the orbital ordering at the Fe site in $\text{FeV}_2\text{O}_4$	106
7.7	The plot of charge density calculated within GGA + $U$ , demonstrating the orbital ordering at the V site in $\text{FeV}_2\text{O}_4$	106
7.8	The difference of GGA + $U$ + SO energies of $\text{FeV}_2\text{O}_4$ , with spin quantization axis pointed along in plane and out of plane directions, plotted for various $c/a$ ratios.	108

# List of Tables

1.1	Examples of few spinel compounds along with their commonly known name and characteristics. . . . .	3
1.2	Wyckoff notation of A, B and X site ions positions for different possible choice of origin for ideal cubic unit cell of spinel . . . . .	4
1.3	The atomic positions of $AB_2X_4$ in $Fd\bar{3}m$ symmetry . . . . .	5
3.1	Energy-minimized structural parameters of $MnV_2O_4$ . . . . .	44
4.1	Magnetic moments of Fe and Cr ions in $\mu_B$ . . . . .	64
4.2	Position of ions of $FeCr_2S_4$ in $F\bar{4}3m$ space group . . . . .	66
5.1	Hopping matrix elements of $FeSc_2S_4$ and $FeCr_2S_4$ and their difference in meV unit . . .	81
5.2	Magnetic moments of Fe and Cr/Sc ions in $\mu_B$ and anisotropy energy in meV/Fe. . . .	82

# Chapter 1

## Introduction

Materials are key to new technologies. Technologies are limited by materials, so for new technologies to develop it is essential to modify known materials in order to improve their properties and to discover, or even design, new materials with specific properties. Compounds like oxides, iodides, sulphides etc which show phenomena like colossal magneto resistance (CMR), high  $T_c$  super-conductivity, multi-ferroicity etc, are under investigation as they promise to be candidates for technological advancement. The knowledge of material characteristics allows the designer not only to make the best material selection for the application in a given device, but also to overcome its limits and constraints in a design. Therefore it is necessary to have microscopic understanding of these materials, to provide insights to the underlying complicated physical and chemical processes.

The chemistry controls the physical properties (*e.g.* electrical, magnetic, and optical properties) of materials. At the root of all these properties are the electrons. Study of electronic structure of such novel materials therefore form an active area of modern condensed matter research. However, such materials are usually complex in structure and in behaviour, containing several atoms in the unit cell involving several different degrees of freedom. As a result, modelling of such complex materials plays an ever increasing role in study of physical properties of those compounds. In this thesis, we have investigated and understood the complex behaviour of some of these compounds in terms suitable modelling, start-

ing from first-principles electronic structure calculations, in general.

We have considered a particular class of materials, called *spinel* compounds and have studied its exciting and intriguing physical properties. The spinel compounds have general formula  $AB_2X_4$ , where A and B can be transition metal elements and X represents mainly oxygen or sulphur. Transition-metal spinels have been, for many years, the subject of intense experimental and theoretical study [1, 2]. Spinel is an ancient name that originally referred to red gemstones, which is magnesium aluminium oxide,  $MgAl_2O_4$ . The name spinel is derived from the Latin word *spina* meaning "little thorn". In ancient Greece, Magnetite ( $Fe_3O_4$ ), the naturally occurring magnet which is a spinel mineral was first found. Magnetite is probably the most important mineral, from a historical perspective, ever to be discovered. In ancient times it was known as *lodestone*. In 1915 Sir Bragg, characterized structure of spinel [3]. In the last century there were many spinel compounds discovered showing different interesting properties. The famous Verwey transition was found in  $Fe_3O_4$  [4].  $LiTi_2O_4$ , the first oxide superconductor discovered [5], is a member of spinel family.  $LiV_2O_4$  is another famous member of spinel family, which show heavy-fermion behaviour without having any *f*-electron states [6]. We shall discuss some of these famous spinel compounds briefly later in this chapter. Table 1.1 illustrates few examples from the vast variety of spinel compounds.

## 1.1 Crystal Structure of Spinel Compounds

Spinel compounds have general formula  $AB_2X_4$ . There are two types of metal sites in the structure, with tetrahedral and octahedral coordination, the later being double in number than the former. From structural point of view, spinel compounds can broadly be classified into two classes, normal spinel and inverse spinel. In a typical normal spinel compound, like manganese vanadate ( $MnV_2O_4$ ), the A cation (in this case  $Mn^{2+}$ ) occupies the tetrahedral site and the B cation (in this case,  $V^{3+}$ ) occupies the octahedral site. In inverse spinel (if not stated, we mean normal spinel as spinel), such as magnetite ( $Fe^{3+}Fe_2^{2.5+}O_4$ ), the tetrahedral site is occupied by B-type cations ( $Fe^{2.5+}$ ), while the octahedral site is

compound	common name and characteristic
MgAl <sub>2</sub> O <sub>4</sub>	Spinel, natural gemstones
ZnAl <sub>2</sub> O <sub>4</sub>	Gahnite, a transparent diamagnetic spinel
FeAl <sub>2</sub> O <sub>4</sub>	Hercynite, a classical paramagnet
gamma-Fe <sub>2</sub> O <sub>3</sub>	Maghemite, a natural material for magnetic recording
Fe <sub>3</sub> O <sub>4</sub>	Magnetite, naturally occurring magnet (lodestone)
Mn <sub>3</sub> O <sub>4</sub>	Hausmannite, a natural tetragonal spinel
Fe <sub>3</sub> S <sub>4</sub>	Greigite, a ferrimagnetic semimetal
NiFe <sub>2</sub> O <sub>4</sub>	Trevorite, a ferrimagnetic semiconductor
ZnFe <sub>2</sub> O <sub>4</sub>	Franklinite, the paramagnetic ferrite
Fe <sub>2</sub> TiO <sub>4</sub>	Ulvùspinel, with giant magnetostrictive properties
Mg <sub>2</sub> SiO <sub>4</sub>	The high-pressure spinel polymorph of forsterite (olivine), which forms constituent of the earth's inner mantle

**Table 1.1** Examples of few spinel compounds along with their commonly known name and characteristics. This table is taken from *J. Am. Ceram. Soc.*, **82**[12], 3277-3278 (1999). Also can be found at <http://www.ruby-sapphire.com/spinel.htm>

shared between A(Fe<sup>3+</sup>) and B cations. In the present thesis all the five spinel compounds studied are of normal type.

The space group of ideal cubic spinel structure is  $Fd\bar{3}m$ , with A and B-site ions occupying high-symmetry position and X-site ion position is a free parameter ( $u, u, u$ ). Thus, for the cubic spinel structure, there is only one free structural parameter other than the lattice constant. Variation of this parameter changes the relative sizes of the tetrahedra and octahedra without changing the crystal symmetry and also introduces distortion within individual octahedron and tetrahedron. In  $Fd\bar{3}m$  space group, description of ion position is dependent on the choice of setting for the origin. The possible choices for the unit-cell origin are either of two different equivalent points with point symmetries  $\bar{4}3m$

For a detail description of spinel structure one may refer to *J. Am. Ceram. Soc.*, **82**[12], 3279-3292 (1999)

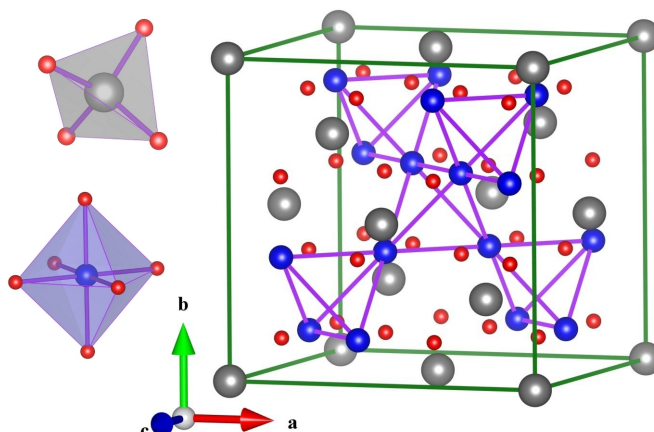


**Figure 1.1** Right hand panel shows crystal structure of spinel compound. A and B sites are represented by grey and blue balls, while the small red balls indicate position of X anion. The B cations form the pyrochlore sub-lattice, shown by violate bonds. In the right hand panel, tetrahedral and octahedral units are shown separately.

and  $\bar{3}m$ . Moreover, the origin can be assigned to either a vacant site or an occupied lattice site. Table 1.2 lists the wyckoff notation of A, B and X site ions positions for different possible choice of origin.

	Origin at $\bar{4}3m$		Origin at $\bar{3}m$	
	Origin at A site	Origin at tetrahedral vacancy	Origin at B site	Origin at octahedral vacancy
A-site cation	$8a$	$8b$	$8b$	$8a$
B-site cation	$16d$	$16c$	$16c$	$16d$
X-site anion	$32e$	$32e$	$32e$	$32e$

**Table 1.2** Wyckoff notation of A, B and X site ions positions for different possible choice of origin for ideal cubic unit cell of spinel

In Fig. 1.1 we show crystal structure of a typical spinel compound. Primitive unit cell of spinel structure in this space group consists of two formula units ( $z = 2$ ). There are two, four and eight equivalent positions of A, B and X site ions respectively. Table 1.3 lists those positions, considering origin at a lattice site occupied by A site ion with  $\bar{4}3m$  point symmetry. The spinel structure can

Site	Multiplicity	Wyckoff letter	Site Symmetry	Coordinates
A	8	<i>a</i>	$\bar{4}3m$	(0, 0, 0) (3/4, 1/4, 3/4)
B	16	<i>d</i>	$\bar{3}m$	(5/8, 5/8, 5/8) (3/8, 7/8, 1/8) (7/8, 1/8, 3/8) (1/8, 3/8, 7/8)
X	32	<i>e</i>	$3m$	(u, u, u) (-u, -u+1/2, u+1/2) (-u+1/2, u+1/2, -u) (u+1/2, -u, -u+1/2) (u+3/4, u+1/4, -u+3/4) (-u+1/4, -u+1/4, -u+1/4) (u+1/4, -u+3/4, u+3/4) (-u+3/4, u+3/4, u+1/4)

**Table 1.3** The atomic positions of  $AB_2X_4$  in  $Fd\bar{3}m$  symmetry, having origin at a lattice site occupied by A site ion with  $\bar{4}3m$  point symmetry

overall be described as three dimensional network of A-site-centered tetrahedra and B-site-centered octahedra. B-site only sub-lattice (shown by violet bonds in Fig. 1.1) forms the pyrochlore lattice, a three-dimensional network of corner shared tetrahedra. Through any one of the B-site ions, three different chains of tetrahedra run in three dimension. Projection of B-site only sub-lattice on to either of crystallographic planes gives rise to checker-board pattern. If this sub-lattice is projected on a plane normal to any of the three chain directions, projected lattice resembles the Kagome lattice. A-site only sub-lattice looks similar to that of diamond lattice (ZnS structure), which is a inter penetrating face center cubic (FCC) structure. Fig. 1.3 shows the A-site only sub-lattice of a spinel structure.

Within cubic phase, spinel compounds can also posses a non-centrosymmetric space group like  $F\bar{4}3m$ . A well studied such spinel compound is  $MgAl_2O_4$ , which remains in  $F\bar{4}3m$  symmetry [7, 8]. Off-center displacement of B-site ion in this space group is allowed, which is not present in usual  $Fd\bar{3}m$  space group. In this present thesis we have studied a sulphide spinel,  $FeCr_2S_4$ , whose space group is debated due to the possible displacement of Cr (B-site ion) and S ions. In chapter 4, we have discussed in detail the possible connections between the two space groups  $Fd\bar{3}m$  and  $F\bar{4}3m$ . Other than cubic, spinel can also have tetragonal and orthorhombic variant. For example  $MnV_2O_4$ ,  $ZnV_2O_4$ ,

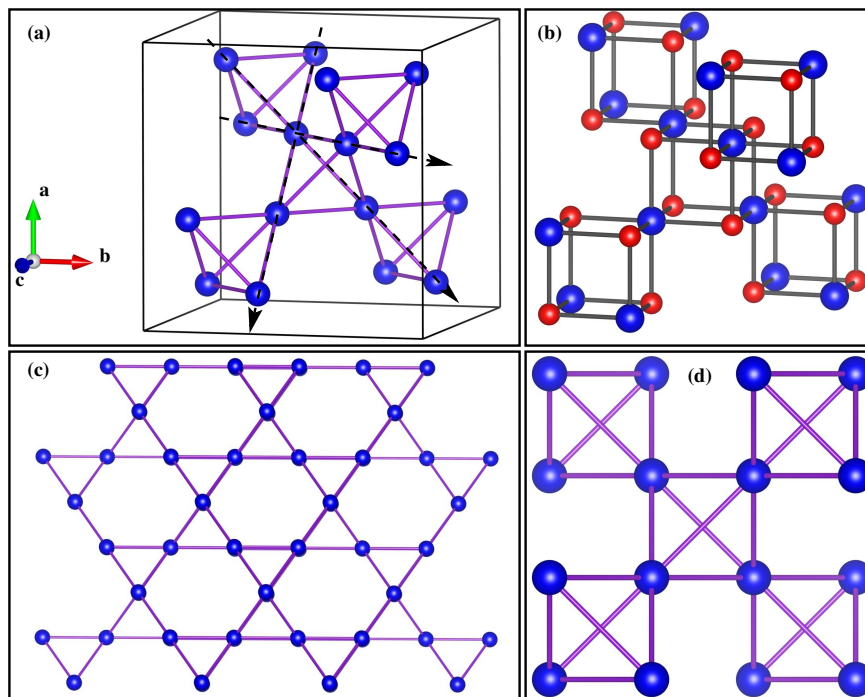


**Figure 1.2** Different projection of B-site only sub-lattice of spinel structure. a) B tetrahedra forming pyrochlore lattice. Three arrows indicates the three chain directions. b)  $B_4X_4$  building blocks inside the conventional unit cell of spinel compound. A site ions are not shown for clarity. The colour convention is same as Fig. 1.1. c) Projection of B-site sub-lattice on normal plane of any of the chain directions, forming Kagome lattice. d) Projection of B-site sub-lattice on any of the crystallographic planes, showing checker-board pattern.

$\text{CoMn}_2\text{O}_4$  exists in tetragonal structure. Many cubic spinel compounds undergo structural transitions on gradual lowering of temperature, from cubic to tetragonal to orthorhombic phase.  $\text{ZnV}_2\text{O}_4$  shows similar structural transitions [9]. In the present thesis we have studied a spinel compound  $\text{FeV}_2\text{O}_4$ , which also undergoes similar structural transition on lowering of temperature[10]. Even few spinel compounds exist in monoclinic symmetry, for example  $\text{Li}_2\text{CrCl}_4$ . The corresponding space group is  $C2/c$  [11] Also this particular compound is a chloride spinel, usually we have oxide or sulphide spinel compounds.

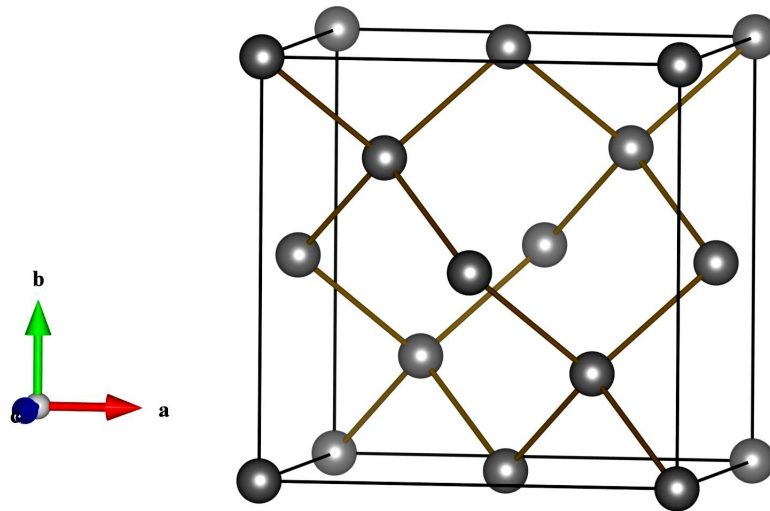


**Figure 1.3** A-site only sub-lattice of a spinel compound, showing diamond lattice. B cations and X anions are not shown inside the conventional unit cell of for better visibility.

## 1.2 Few Important Spinel Compounds

**Fe<sub>3</sub>O<sub>4</sub>** : Among the famous spinel compounds, the first candidate that comes to the list is Magnetite, Fe<sub>3</sub>O<sub>4</sub>. Starting from ancient times, it is known as naturally occurring magnet, named as lodestone. In 1915, Sir Bragg determined spinel crystal structure by doing x-ray diffraction on this particular compound, along with MgAl<sub>2</sub>O<sub>4</sub>. In 1939 the famous Verwey transition was discovered in this compound. When heated up to a temperature  $\sim 122K$ , this compound exhibits more than order of magnitude increase in conductivity, accompanied by structural transition. This threshold temperature is known as Verwey transition temperature after name of it's discoverer[4]. There has been numerous attempts in last seventy years or so, to have a definite model that can explain the behaviour of the system blow the transition temperature. Still this is a subject of active research, which is yet to be understood unambiguously. Apart from Fe<sub>3</sub>O<sub>4</sub>, in Ti<sub>4</sub>O<sub>7</sub> and Eu<sub>3</sub>Si<sub>4</sub> [12] charge order-disorder transitions of Verwey type take place.

**LiV<sub>2</sub>O<sub>4</sub>** : Heavy fermion behaviours are usually found in Ce and U based rare earth compounds that have two different types of electrons near Fermi level ( $E_F$ ), one is localized  $f$ -electrons and other one is

conduction electrons.  $\text{LiV}_2\text{O}_4$ , spinel compound shows heavy fermion behaviour which is very surprising since the system has only  $d$ -electrons near  $E_F$  [6]. In  $\text{LiV}_2\text{O}_4$ , B-site ion is  $\text{V}^{3.5+}$  which is magnetic in nature. As discussed in the previous section, they form a network of corner-sharing tetrahedra, which is a frustrating lattice for antiferromagnetic nearest neighbour interactions. The topology of the lattice prohibits antiferromagnetically aligned spins from ordering and induces macroscopic degeneracy in the ground state. Such kind of macroscopic ground state degeneracy leads to a large enhancement of spin fluctuations at low temperature and heavy-mass quasiparticles.

**$\text{LiTi}_2\text{O}_4$**  : In the field of superconductivity, spinel compounds are also known, although there are not many spinel superconductors in numbers. There are four spinel compounds which are reported as superconductors. These spinel compounds are  $\text{CuV}_2\text{S}_4$  ( $T_c = 4.45$  K) [13],  $\text{CuRh}_2\text{S}_4$  ( $T_c = 4.8$  K) [13],  $\text{CuRh}_2\text{Se}_4$  ( $T_c = 4.39$  K) [13, 14] and  $\text{LiTi}_2\text{O}_4$  ( $T_c = 11.2$  K) [15]. Superconductivity in  $\text{LiTi}_2\text{O}_4$  was first reported by Johnston *et al.* [15] in 1973, more than a decade before the discovery of high- $T_c$  cuprate superconductors [16]. The mechanisms underlying the superconductivity of  $\text{LiTi}_2\text{O}_4$  are yet not resolved properly. Experimental studies on measurement of superconducting energy gap [16] have shown that  $\text{LiTi}_2\text{O}_4$  is a weak coupling,  $d$ -band superconductor. Although there are experimental studies like, specific heat value measurements [17, 18], EXAFS Ti K-edge measurements [19], NMR experiments [20] which suggested that  $\text{LiTi}_2\text{O}_4$  is a correlated  $d$ -electron metal. Muon spin relaxation experiments [21] reported that the superconducting condensation mechanism in this system differs from usual mechanism in simple metal BCS superconductors. In literature  $\text{LiTi}_2\text{O}_4$  has been included to the family of so-called “exotic” superconductors [22, 23, 24].

**$\text{LiMn}_2\text{O}_4$**  : Now a days in consumer electronics Lithium-ion batteries are used a lot as rechargeable batteries. Popularity of these type of batteries has increased because of their non-toxicity, slow loss of charge, and no memory effects.  $\text{LiMn}_2\text{O}_4$ , a spinel compound is commonly used as the cathode for Li-ion batteries. This spinel compound exhibits a high capacitance which means it has the ability to store charge [25]. At the same time, possibility of  $\text{Li}^{1+}$  to be reinserted into its parent structure by a reverse electrochemical potential gives rise to the rechargeable capability of the battery [26].

**CoFe<sub>2</sub>O<sub>4</sub>** : CoFe<sub>2</sub>O<sub>4</sub> is another member of inverse spinel family, which has recently been studied as a component for ferrofluids. Ferrofluids are colloidal suspensions of ferromagnetic nano-particles. Depending on their size, these nano-particles exhibit different magnetic properties, such as superparamagnetism. On application of an alternating magnetic field to the superparamagnetic particles, they undergo thermal fluctuations as the spins overcome their blocking energy barrier and flip with the alternating magnetic field [27]. The ability to produce heat from the thermal fluctuations makes colloidal suspensions of this particular spinel compound a good candidate for hyperthermia based cancer treatments. CoFe<sub>2</sub>O<sub>4</sub> nano-particles are directed towards the cancerous area and temperature of the particles are raised by applying magnetic field. This in turn cooks the cancerous tissue enough to lower its resistance to chemotherapy [28].

This section lists a few of the very known and well studied spinel compounds from the vast list of compounds. Many of them are yet not well understood, and makes them a topic of active research till now. Some of them have been implemented in smart devices which are very essential in our daily also. This unarguably defines the wide range of importance of spinel compound in modern days research activity.

### **1.3 First-Principles Studies on Spinel Compound**

As discussed in the previous section, the spinel family contains many known compounds, and they show a wide spectrum of interesting properties, which makes this class of compound a familiar topic of active research for the last few decades. In this section we shall briefly discuss the works done using first-principles method on spinel compounds. As mentioned already which forms also the method for study in the present thesis. For a cubic spinel, which is the most usual form spinel compounds, there are only two free parameters in terms of its structural aspect, lattice parameter and position of X anion ( $u$  parameter). Many first-principles calculations have been done on spinel compounds to determine theoretically these two parameters. In such studies the agreement between theoretically optimized value and the experimental values is good. In general, although sometimes calculations done within local-density approximation (LDA) show tendency of underestimating the lattice parameter and

calculations done within generalized gradient approximation (GGA) show tendency of overestimating the same. A detail information of such type of calculations on cubic spinels like  $\text{ZnGa}_2\text{O}_4$ ,  $\text{ZnAl}_2\text{O}_4$ ,  $\text{ZnFe}_2\text{O}_4$ ,  $\text{MnFe}_2\text{O}_4$  and  $\text{LiMn}_2\text{O}_4$  can be found in Table 1 of Ref. [2]. At the beginning of this chapter we have discussed that spinel compounds can be classified into two major classes from structural point of view, normal spinel and inverse one. Stability between the normal and inverse phase of a spinel compound has also been studied by carrying out total-energy calculations [29]. Theoretically predicted results agree well with the experimentally reported ones.

The microscopic origin of metallic or insulating ground state of spinel compounds, especially for transition-metal spinels have been studied extensively. In addition to this magnetic interactions and ordering have also been investigated by first-principle calculations. For example,  $\text{ZnFe}_2\text{O}_4$  has been found to be an insulator from the calculation done within GGA and with antiferromagnetic (AFM) spin ordering at B site ion[30]. Small-gap insulating solution has been found for a very similar spinel compound  $\text{MnFe}_2\text{O}_4$ [31]. Band gap value of 0.98 eV has been computed for  $\text{NiFe}_2\text{O}_4$ , and half-metallic solution has been found for another ferrites spinel  $\text{CoFe}_2\text{O}_4$ [29].

Magnetic exchange interactions in spinel compounds have been studied extensively using first-principles calculations. Usually the B site ion in  $\text{AB}_2\text{X}_4$  is of magnetic in nature, although there are many spinel compounds with magnetic ions at only A site or at both A and B site. If there were only magnetic ions on B sites with only nearest-neighbour AFM coupling, then the magnetic ordering would be dominated by frustration. This is simply because the B-only sub-lattice of spinel structure forms pyrochlore lattice. In real materials, the further-neighbour interactions can be however quite dominant in determining the magnetic ordering. Table 2 of Ref.[2] lists theoretically computed magnetic exchange interactions  $J$  in many spinel compounds with magnetic ions at B site only. There are examples of spinel compounds with magnetic ions both at A and B sites, for such spinel compounds the magnetic ordering pattern becomes more complicated. For example, such a spinel compound is  $\text{MnFe}_2\text{O}_4$ , where  $\text{Mn}^{2+}$  and  $\text{Fe}^{3+}$  both have  $d^5$  configuration. Magnetic exchange interactions of this spinel has been computed via first-principles calculations[32] and that matches well with experimental

results. Substitution of a magnetic cation into a nonmagnetic spinel compound has been suggested as one of the routes to obtain novel magnetic semiconductors[33]. Cation ordering as well as magnetic interactions of  $\text{ZnFe}_2\text{O}_4$  and  $\text{CdFe}_2\text{O}_4$  were investigated from first principles calculations[34] by computing total energies of those systems.

It has been seen that spin-lattice coupling can play an important role in magnetic spinel systems. Magnetocrystalline anisotropy energy was computed for compounds like  $\text{Fe}_3\text{O}_4$ [35],  $\text{NiFe}_2\text{O}_4$ [36] and  $\text{CoFe}_2\text{O}_4$ [37]. The dependence of the anisotropy on epitaxial strain is also computed from first principles for these above mentioned compounds.

Due to the structural complexities of the spinel structure, the first principles study of phonon frequencies, structural instabilities and structural phase transitions as a function of temperature and pressure forms a active field of research. Phonon calculations have been done on  $\text{ZnAl}_2\text{O}_4$  and  $\text{ZnGa}_2\text{O}_4$  systems, and a fair agreement with experimental Raman and infrared determinations has been found[38].  $\text{LiMn}_2\text{O}_4$  is a very known spinel compound, commonly used as the cathode for Li-ion batteries. Raman and infrared-active phonon frequencies of this compound were computed from first principles[39] and found to be in good agreement with experiment.

Pressure dependence of structural parameters and prediction of structural transitions with pressure has been addressed quite a few times in literature for spinel compounds. The pressure dependence of lattice parameter and positional parameter  $u$  for spinel compounds  $\text{ZnAl}_2\text{O}_4$  and  $\text{ZnGa}_2\text{O}_4$  are studied via first principles calculations[38].

These examples establish the validity of first-principles approaches in studying spinel compounds which are complex in their geometrical constructions as well as in behaviour.

## 1.4 Motivation and Overview of Present Thesis

It is very much evident from several examples presented in the previous section that first principles calculations on spinel compounds has been greatly advanced, in terms of making accurate predictions. Needless to say that the impressive improvements in computational techniques and computer resources

helped to reach at this point. First principle calculations helped to understand the structure and many intriguing properties of these compounds, which at a glance seems to be very complex with many degrees of freedom, but still there are many more open questions and issues to be understood. The understanding at the microscopic level opens avenues for the design of new materials. A better understanding of the interplay between the different ordering like magnetic, charge and orbital degrees of freedom will lead to the identification of materials with desirable functional properties . Parallel to this, first principles calculations can make more precise connection between the real system and the simplified model to understand the underlying physics[41] leading to conceptual advances and a stronger interaction between theory and experiment.

In this present thesis we have studied five different spinel compounds namely,  $\text{MnV}_2\text{O}_4$ ,  $\text{FeCr}_2\text{S}_4$ ,  $\text{FeSc}_2\text{S}_4$ ,  $\text{CuIr}_2\text{S}_4$  and  $\text{FeV}_2\text{O}_4$ . First principles calculations have been done on these compounds to understand from microscopic point of view the exciting properties exhibited by them. The contents of the various chapters discussed in the present thesis are as follows :

**Chapter 2** : The First principles calculations carried out, are based on Density Functional Theory (DFT). In this chapter, we have discussed the theoretical background of the DFT and applying the same, how in practice one can solve a many electron Hamiltonian is discussed in nut-shell. We have discussed the different basis sets which we have considered during the course of calculation, depending upon the properties we have studied. We have also discussed the construction of low energy model Hamiltonian of such complex materials starting from a first-principles calculations.

**Chapter 3** : We have proposed a possible orbital ordering in spinel compound  $\text{MnV}_2\text{O}_4$  which consists of orbital chains running along crystallographic  $a$  and  $b$  directions with orbitals rotated alternatively by about  $45^\circ$  within each chain, in this chapter. For a correct description of the space group symmetry from theoretical calculation, consideration of correlation effects sometime becomes crucial. This has been discussed in detail in context of determination of low temperature crystal structure symmetry of  $\text{MnV}_2\text{O}_4$ . This implies that the correlation-driven orbital ordering has a strong influence on the structural transitions in this system. Our proposed orbital ordering

favours a noncollinear magnetic spin arrangement of V ions, which is found to be in agreement with the experimental results. In addition to this V-V exchange interactions have been studied theoretically.

**Chapter 4 :** Experimentally it has been found that low temperature of phase of  $\text{FeCr}_2\text{S}_4$  spinel is an insulator, although simple electron count in this compound predicts it to be a half-metal. Our calculations provide a microscopic understanding of the origin of the insulating behaviour of this compound. The insulating state is found to be driven by Coulomb enhanced spin-orbit coupling operative within the Fe- $d$  manifold. There is a controversy regarding the structural distortion at low temperature structure of  $\text{FeCr}_2\text{S}_4$ . We have investigated from theoretical point of view, the possibility of the structural distortions. We have further compared the calculated optical property data with that of the experimental one.

**Chapter 5 :** In this chapter we presented a comparative study of two very similar Fe-based spinel compounds,  $\text{FeCr}_2\text{S}_4$  and  $\text{FeSc}_2\text{S}_4$ . Though both systems contain an orbitally active A site with an  $\text{Fe}^{2+}$  ion, their properties are rather dissimilar. We have carried out first principles calculations to find out the microscopic origin of their distinct behaviour. Our calculations reveals that root cause behind this dissimilar behaviour of two spinel compounds is the differences in hybridization of Fe  $d$  states with Cr/Sc  $d$  states and S  $p$  states in the two cases. This leads to the differences in the nature of the magnetic exchanges of these two spinel compounds. The nearest neighbour versus next-nearest neighbour exchange parameter ratios in those two compounds as well as the magnitude and signs of magnetic interactions are found to be very different in the two compounds. This results into significant frustration effects in  $\text{FeSc}_2\text{S}_4$  which are absent in  $\text{FeCr}_2\text{S}_4$ .

**Chapter 6 :** This chapter describes the theoretically computed electronic and optical properties of spinel compound  $\text{CuIr}_2\text{S}_4$ . This compound undergoes a structural phase transition, accompanied by a metal-insulator transition (MIT) at a temperature of about 230 K. The nature of this MIT has been discussed in the literature in terms of both the correlated singlet formation picture as well as

the orbitally driven Peierls transition picture [42]. Our first principles study finds that correlation has little effect on this compound. Theoretically computed reflectivity and conductivity data for both the high-temperature and low-temperature phases are found to be in good agreement with the experimental results reported.

**Chapter 7 :** In this chapter we have discussed about  $\text{FeV}_2\text{O}_4$ , a spinel with orbital degrees of freedom both at Fe and V sites that exhibits two tetragonal phases, one compressed at high temperature and another elongated at low temperature. Our first principles calculations reveal that orbital ordering at Fe sites at the high and low temperature phases there are ferro-orbital ordering of  $x^2 - y^2$  and  $3z^2 - 1$  types, respectively. The orbital ordering at V sites is found to consist of orbital chains running along different directions with orbitals rotated alternatively within each chain. This is very similar to the case of  $\text{MnV}_2\text{O}_4$ , which is discussed in chapter 3. We have also found that the single-ion anisotropy effect with hard and easy  $c$  axis favors the compressed and elongated tetrahedral shapes driving the two different orbital ordering patterns at Fe site at high and low temperatures. This gives rise to magnetocrystalline anisotropy-dependent shapes.

**Chapter 8 :** This chapter deals with summery of the results of study on five different spinel compounds at one place. Also we have discussed the possibilities of future work.

---

Crystal structures shown in this chapter and in all the subsequent chapters are produced using either of two software packages, VESTA [43] or XCrystDEN [44].

# Bibliography

- [1] P. G. Radaelli, *New Journal of Physics* **7**, 53 (2005).
- [2] K. M. Rabe, *Annual Review of Condensed Matter Physics* **1**, 211–235 (2010).
- [3] W. H. Bragg, *Nature* **95**, 561–561 (1915).
- [4] E. J. W. Verwey, *Nature* **144**, 327–328 (1939).
- [5] D. C. Johnston, *Journal of Low Temperature Physics* **25**, 145–175 (1976), 10.1007/BF00654827.
- [6] C. Urano, M. Nohara, S. Kondo, F. Sakai, H. Takagi, T. Shiraki, and T. Okubo, *Phys. Rev. Lett.* **85**, 1052–1055 (2000).
- [7] P. R. Staszak, J. E. Poetzinger, and G. P. Wirtz, *Journal of Physics C: Solid State Physics* **17**, 4751 (1984).
- [8] K. D. Rouse, M. W. Thomas, and B. T. M. Willis, *Journal of Physics C: Solid State Physics* **9**, L231 (1976).
- [9] H. Ishibashi and T. Yasumi, *Journal of Magnetism and Magnetic Materials* **310**, e610 – e612 (2007), proceedings of the 17th International Conference on Magnetism.
- [10] M. Tanaka, T. Tokoro, and Y. Aiyama, *Journal of the Physical Society of Japan* **21**, 262–267 (1966).
- [11] R. Kanno, Y. Takeda, A. Matsumoto, O. Yamamoto, R. Suyama, and S. Kume, *Journal of Solid State Chemistry* **75**, 41 – 51 (1988).

- [12] D. Ihle and B. Lorenz, *physica status solidi (b)* **116**, 539–546 (1983).
- [13] N. V. Maaren, G. Schaeffer, and F. Lotgering, *Physics Letters A* **25**, 238 – 239 (1967).
- [14] M. Robbins, R. Willens, and R. Miller, *Solid State Communications* **5**, 933 – 934 (1967).
- [15] D. Johnston, H. Prakash, W. Zachariasen, and R. Viswanathan, *Materials Research Bulletin* **8**, 777 – 784 (1973).
- [16] J. G. Bednorz and K. A. Müller, *Zeitschrift für Physik B Condensed Matter* **64**, 189–193 (1986), 10.1007/BF01303701.
- [17] Heintz, J. M., Drillon, M., Kuentzler, R., Dossmann, Y., Kappler, J. P., and Gautier, F., *J. Phys. Colloques* **49**, C8–2191–C8–2192 (1988).
- [18] J. M. Heintz, M. Drillon, R. Kuentzler, Y. Dossmann, J. P. Kappler, O. Durmeyer, and F. Gautier, *Zeitschrift für Physik B Condensed Matter* **76**, 303–309 (1989), 10.1007/BF01321907.
- [19] O. Durmeyer, J. P. Kappler, E. Beaurepaire, J. M. Heintz, and M. Drillon, *Journal of Physics: Condensed Matter* **2**, 6127 (1990).
- [20] D. P. Tunstall, J. R. M. Todd, S. Arumugam, G. Dai, M. Dalton, and P. P. Edwards, *Phys. Rev. B* **50**, 16541–16549 (1994).
- [21] W. D. Wu, A. Keren, L. P. Le, G. M. Luke, B. J. Sternlieb, Y. J. Uemura, D. C. Johnston, B. K. Cho, and P. Gehring, *Hyperfine Interactions* **86**, 615–621 (1994), 10.1007/BF02068956.
- [22] Y. J. Uemura *et al.*, *Phys. Rev. Lett.* **66**, 2665–2668 (1991).
- [23] Y. J. Uemura *et al.*, *Nature* **352**, 605–607 (1991).
- [24] B. Brandow, *Physics Reports* **296**, 1 – 63 (1998).
- [25] L. C. Ferracin, F. A. Amaral, and N. Bocchi, *Solid State Ionics* **130**, 215 – 220 (2000).

- [26] J. M. Tarascon, E. Wang, F. K. Shokoohi, W. R. McKinnon, and S. Colson, *Journal of The Electrochemical Society* **138**, 2859–2864 (1991).
- [27] C. Liu, B. Zou, A. J. Rondinone, and Z. J. Zhang, *Journal of the American Chemical Society* **122**, 6263–6267 (2000).
- [28] J.-P. Fortin, C. Wilhelm, J. Servais, C. MÃnager, J.-C. Bacri, and F. Gazeau, *Journal of the American Chemical Society* **129**, 2628–2635 (2007).
- [29] Z. Szotek, W. M. Temmerman, D. Ködderitzsch, A. Svane, L. Petit, and H. Winter, *Phys. Rev. B* **74**, 174431 (2006).
- [30] D. J. Singh, M. Gupta, and R. Gupta, *Phys. Rev. B* **63**, 205102 (2001).
- [31] D. J. Singh, M. Gupta, and R. Gupta, *Journal of Applied Physics* **91**, 7370–7372 (2002).
- [32] X. Zuo and C. Vittoria, *Phys. Rev. B* **66**, 184420 (2002).
- [33] L. Pisani, T. Maitra, and R. Valentí, *Phys. Rev. B* **73**, 205204 (2006).
- [34] C. Cheng, *Phys. Rev. B* **78**, 132403 (2008).
- [35] H.-T. Jeng and G. Y. Guo, *Phys. Rev. B* **65**, 094429 (2002).
- [36] H.-T. Jeng and G. Guo, *Journal of Magnetism and Magnetic Materials* **240**, 436 – 438 (2002), 4th International Symposium on Metallic Multilayers.
- [37] H.-T. Jeng and G. Guo, *Journal of Magnetism and Magnetic Materials* **239**, 88 – 90 (2002), international Symposium on Physics of Magnetic Materials/International Symposium on Advanced Magnetic Technologies.
- [38] S. López, A. H. Romero, P. Rodríguez-Hernández, and A. Muñoz, *Phys. Rev. B* **79**, 214103 (2009).
- [39] C. M. Fang, G. A. de Wijs, C.-K. Loong, and G. de With, *J. Mater. Chem.* **17**, 4908–4913 (2007).

- 
- [40] G. Giovannetti *et al.*, Phys. Rev. B **83**, 060402 (2011).
- [41] R. T. Clay, H. Li, S. Sarkar, S. Mazumdar, and T. Saha-Dasgupta, Phys. Rev. B **82**, 035108 (2010).
- [42] D. I. Khomskii and T. Mizokawa, Phys. Rev. Lett. **94**, 156402 (2005).
- [43] K. Momma and F. Izumi, Journal of Applied Crystallography **44**, 1272–1276 (2011).
- [44] A. Kokalj, Computational Materials Science **28**, 155 – 168 (2003), proceedings of the Symposium on Software Development for Process and Materials Design.

## Chapter 2

# Theoretical background of electronic structure calculations

### 2.1 Density Functional Theory (DFT) way of solving quantum many body problem

#### 2.1.1 The many-electron Hamiltonian

Any material can be thought of as a collection of positively charged particles (nuclei) and negatively charged particles (electrons). If we have  $N_n$  nuclei surrounded by  $N_e$  electrons, then essentially we are dealing with a many-body problem. The full many-particle Hamiltonian for such system can be written as

$$H = -\frac{\hbar^2}{2m_e} \sum_{i=1}^{N_e} \nabla_{\mathbf{r}_i}^2 - \frac{\hbar^2}{2M_I} \sum_{I=1}^{N_n} \nabla_{\mathbf{R}_I}^2 - \frac{1}{4\pi\epsilon_0} \sum_{i,I} \frac{Z_I e^2}{|\mathbf{R}_I - \mathbf{r}_i|} + \frac{1}{4\pi\epsilon_0} \sum_{i>j} \frac{e^2}{|\mathbf{r}_i - \mathbf{r}_j|} + \frac{1}{4\pi\epsilon_0} \sum_{I>J} \frac{Z_I Z_J e^2}{|\mathbf{R}_I - \mathbf{R}_J|} \quad (2.1)$$

where, in the above equation, the mass of the nucleus at  $\mathbf{R}_I$  is  $M_I$ . The electron has mass  $m_e$  and the corresponding position is denoted by  $\mathbf{r}_i$ . The first term of Eq.(2.1) is the kinetic energy operator for the electrons while the second one is for the nuclei. The last three terms describe the Coulomb interaction between electrons and nuclei, between electrons and other electrons, and between nuclei and

other nuclei respectively. Exact diagonalization of this kind of Hamiltonian is a very difficult because of large degrees of freedom that are involved. In order to find acceptable solutions, one needs to make approximations at different levels.

The first step towards the simplification of the above equation is the *Born-Oppenheimer (B-O) approximation*(1927)[1]. The nuclei are much heavier and therefore much slower than the electrons. We can hence consider nuclei to be “static” at “fixed” positions and assume the electrons to be in instantaneous equilibrium with them. Following this approximation, the kinetic energy of ions can be neglected and the ion-ion interaction (last term in Eq.(2.1)) is assumed to be constant. The constant term, called Madelung energy, is calculated classically. So under B-O approximation, the many-body Hamiltonian for a system of N (since from now we shall deal with only electrons so  $N_e$  is changed to N) interacting electrons moving in the field of fixed ion cores, takes the form

$$H = - \sum_{i=1}^N \frac{\hbar^2}{2m_e} \nabla_{\mathbf{r}_i}^2 - \frac{1}{4\pi\epsilon_0} \sum_{i,I} \frac{Z_I e^2}{|\mathbf{R}_I - \mathbf{r}_i|} + \frac{1}{2} \frac{1}{4\pi\epsilon_0} \sum_{i,j} \frac{e^2}{|\mathbf{r}_i - \mathbf{r}_j|} \quad (2.2)$$

Even after this simplification, it represents a very complicated many-electron eigen value problem and further approximation is needed to solve it. Efforts have been put, therefore, to develop an effective single-particle picture, in which the system of interacting electrons can be mapped onto a system of non-interacting quantum mechanical particles that approximates the behaviour of original system. Two distinct approaches have been put forward in this direction: *wave function based approach* and *density functional theory based approaches*.

### 2.1.2 Wave function based approach

Hartree in 1928 first expressed the many-body wave function as a product of single-electron functions  $\{\phi_i(\mathbf{r}_i)\}$  as  $\psi^H(\mathbf{r}_1, \mathbf{r}_2, \dots, \mathbf{r}_N) = \phi_1(\mathbf{r}_1)\phi_2(\mathbf{r}_2) \dots \phi_N(\mathbf{r}_N)$  and solved, numerically, the equation for each electron moving in a central potential due to other electrons and the nucleus [2]. This simplest approximation can only take into account the electron-electron Coulomb repulsion in a mean-field way, neglecting the exchange and correlation properties completely. The next level of sophistication was then introduced by Fock in 1930 [3], incorporating the anti-symmetric character of electronic wave

function in terms of Slater determinant

$$\psi^{HF} = \frac{1}{\sqrt{N!}} \begin{vmatrix} \phi_1(\mathbf{r}_1) & \phi_1(\mathbf{r}_2) & \cdots & \phi_1(\mathbf{r}_N) \\ \phi_2(\mathbf{r}_1) & \phi_2(\mathbf{r}_2) & \cdots & \phi_2(\mathbf{r}_N) \\ \vdots & \vdots & \ddots & \vdots \\ \phi_N(\mathbf{r}_1) & \phi_N(\mathbf{r}_2) & \cdots & \phi_N(\mathbf{r}_N) \end{vmatrix}. \quad (2.3)$$

Application of the variational principle shows that such one-electron wave functions satisfy the Hartree-Fock (H-F) equations like

$$\left[ -\frac{\hbar^2}{2m_e} \nabla_{\mathbf{r}_i}^2 + V_{ion}(\mathbf{r}_i) + V^H(\mathbf{r}_i) + V^X \right] \phi_i(\mathbf{r}_i) = \varepsilon_i \phi_i(\mathbf{r}_i) \quad (2.4)$$

with

$$V^H(\mathbf{r}_i) = e^2 \sum_j^{occ} \int \frac{|\phi_j(\mathbf{r}_j)|^2}{|\mathbf{r}_i - \mathbf{r}_j|} d\mathbf{r}_j \quad (2.5)$$

as the Hartree potential and the exchange potential is given by

$$V_i^X \phi_i(\mathbf{r}_i) = - \sum_j^{occ} \phi_j(\mathbf{r}_i) \int \phi_j^*(\mathbf{r}_j) \frac{e^2}{|\mathbf{r}_i - \mathbf{r}_j|} \phi_i(\mathbf{r}_j) d\mathbf{r}_j \quad (2.6)$$

The exchange term  $V^X$  is difficult to derive in practice because it is non-local and related to the interaction between all electrons in the system. Consequently, the Hartree-Fock approach has a highly computational cost and is therefore restricted to small systems. In spite of the importance and achievements of the Hartree-Fock approximation, corrections beyond it are often considered due to the fact that a single determinantal state, even with the best possible orbitals, remains in general a rather poor representation of the complicated ground state wave function of a many-body system. Therefore, methods like configuration interaction (CI) approach have been developed by quantum chemists [4], which consider a linear combination of different determinantal states to improve the situation. However, such approach becomes quickly computationally prohibitive as the system size grows.

### 2.1.3 Density functional theory

In 1964, Hohenberg and Kohn proposed the Density Functional Theory (DFT) [5] to deal with many-electron problems more efficiently. In DFT one ignores the precise details of the many-electron wave

function  $\psi(\mathbf{r}_1, \mathbf{r}_2, \dots, \mathbf{r}_N)$  and considers the density of electrons in the system

$$\rho(\mathbf{r}) = N \int \psi^*(\mathbf{r}, \mathbf{r}_2, \dots, \mathbf{r}_N) \psi(\mathbf{r}, \mathbf{r}_2, \dots, \mathbf{r}_N) d\mathbf{r}_2 d\mathbf{r}_3 \dots d\mathbf{r}_N$$

as the basic variable. The main result of DFT is that the ground state properties of a many electron system are uniquely determined by its electron density distribution. In other words, all ground state properties of the many electron system are functional of its ground state electron density distribution. When the ground state electron density distribution of the many electron system is determined, its external potential is also uniquely determined.

### 2.1.3.1 Basic theorems of DFT and Kohn-Sham equation

Density functional theorem can be expressed in terms of two basic theorems:

Theorem I : There is a one-to-one correspondence between the ground-state density  $\rho(\mathbf{r})$  of a many-electron system and the external potential  $V_{ext}$ . An immediate consequence is that the ground-state expectation value of any observable  $\hat{O}$  is a unique functional of the exact ground-state electron density:

$$\langle \Psi | \hat{O} | \Psi \rangle = O[\rho]$$

Few steps of calculation can prove the above statement. Let us consider two N-electron systems, characterised by two different external potentials (differing by more than an additive constant),  $V_1(r)$  and  $V_2(r)$ . Let us consider that corresponding two wavefunctions  $\psi_1$  and  $\psi_2$ , yield the same electron density  $\rho(\mathbf{r})$ . One can use the variational principle and write for the energy the results:

$$\begin{aligned} E_1 &= \langle \psi_1 | H_1 | \psi_1 \rangle \\ &< \langle \psi_2 | H_1 | \psi_2 \rangle = \langle \psi_2 | H_2 | \psi_2 \rangle + \langle \psi_1 | [H_1 - H_2] | \psi_1 \rangle \\ &< E_2 + \int dr \rho(r) [V_1(r) - V_2(r)] \end{aligned}$$

On interchange of the suffixes, one also has the result

$$E_2 < E_1 + \int dr \rho(r) [V_2(r) - V_1(r)]$$

Summation of the two inequalities leads to the contradiction

$$E_1 + E_2 < E_2 + E_1$$

Hence the assumption of identical density arising from two different external potentials is wrong. This automatically follow the following:

A given  $\rho(\mathbf{r})$  can correspond to only one  $v(\mathbf{r})$

↓

Since  $V(\mathbf{r})$  is fixed, the Hamiltonian and hence the wave-function are also fixed by the density.

↓

Since the wave-function is a functional of density, the energy functional  $E_V[\rho]$  for a given external potential  $V(\mathbf{r})$  is a unique functional of density.

Theorem II : For  $\hat{O}$  being the Hamiltonian  $\hat{H}$ , the ground-state total energy functional  $H[\rho] \equiv E_{V_{ext}}[\rho]$  is of the form

$$E_{V_{ext}}[\rho] = \underbrace{\langle \Psi | \hat{T} + \hat{V} | \Psi \rangle}_{F_{HK}} + \langle \Psi | \hat{V}_{ext} | \Psi \rangle \quad (2.7)$$

$$= F_{HK}[\rho] + \int \rho(\mathbf{r}) V_{ext}(\mathbf{r}) d\mathbf{r} \quad (2.8)$$

where the Hohenberg-Kohn density functional  $F_{HK}[\rho]$  is universal for any many-electron system.  $E_{V_{ext}}[\rho]$  reaches its minimal value (equal to the ground-state total energy) for the ground state density corresponding to  $V_{ext}$ .

The Hohenberg-Kohn variational theorem states that if the functional  $E_{V_{ext}}[\rho]$  is varied with respect to  $\rho(\mathbf{r})$ , then  $E_{V_{ext}}[\rho_0]$  takes the lowest value, corresponding to the ground state, with the correct ground state density  $\rho_0(\mathbf{r})$ , i.e.  $E_{V_{ext}}[\rho_0] \leq E_{V_{ext}}[\rho]$ . The equations of Kohn and Sham, published in 1965, turn

DFT into a practical tool [6]. We can rewrite the Hohenberg-Kohn functional in the following way :

$$\begin{aligned}
 F_{HK} &= T + V + T_0 - T_0 \\
 &= T_0 + V + \underbrace{T - T_0}_{V_C} \\
 &= T_0 + V_H + V_C + \underbrace{V - V_H}_{V_X} \\
 &= T_0 + V_H + \underbrace{V_C + V_X}_{E_{XC}}
 \end{aligned}$$

Here  $T$  and  $V$  are the exact kinetic and electron-electron potential energy functionals,  $T_0$  is the functional for the kinetic energy of a non-interacting electron gas,  $V_H$  stands for the Hartree contribution and  $V_X$  for the exchange contribution. Here  $E_{XC}$  is the exchange-correlation energy functional. We can write explicitly the energy functional as following

$$E_{V_{ext}}[\rho] = T_0[\rho] + V_H[\rho] + E_{XC}[\rho] + V_{ext}[\rho] \quad (2.9)$$

The above expression can also be viewed from a different perspective as the energy functional of a non-interacting classical electron gas, subject to two external potentials. One due to the nuclei, and other due to exchange and correlation effects. The corresponding Hamiltonian - called the Kohn-Sham Hamiltonian is

$$\begin{aligned}
 \hat{H}_{KS} &= \hat{T}_0 + \hat{V}_H + \hat{V}_{XC} + \hat{V}_{ext} \\
 &= -\frac{\hbar^2}{2m_e} \nabla_i^2 + \frac{e^2}{4\pi\epsilon_0} \int \frac{\rho(\hat{\mathbf{r}})}{|\mathbf{r} - \hat{\mathbf{r}}|} d\hat{\mathbf{r}} + \hat{V}_{XC} + \hat{V}_{ext}
 \end{aligned} \quad (2.10)$$

where the exchange-correlation potential is given by the functional derivative

$$\hat{V}_{XC} = \frac{\delta E_{XC}[\rho]}{\delta \rho} \quad (2.11)$$

The minimization of  $E_{KS}$  ( $E_{V_{ext}}$  in Eq.(2.9)) is carried out subject to the constraint of normalized density  $\int \rho(\mathbf{r}) d\mathbf{r} = N$ . Application of the variational principle of the Kohn-Sham theory requires that for the ground state

$$\frac{\delta}{\delta \rho} \{E_{KS}[\rho] - \lambda N\} = 0 \quad (2.12)$$

$\lambda$  is the Lagrange multiplier. Using Eq.(2.9), one gets,

$$\frac{\delta T_0[\rho]}{\delta \rho(\mathbf{r})} + V_{KS}(\mathbf{r}) = \lambda \quad (2.13)$$

where

$$V_{KS}(\mathbf{r}) = v(\mathbf{r}) + V_H(\mathbf{r}) + V_{XC}(\mathbf{r}) = v(\mathbf{r}) + \frac{e^2}{4\pi\epsilon_0} \int \frac{\rho(\mathbf{r}')}{|\mathbf{r} - \mathbf{r}'|} d\mathbf{r}' + \frac{\delta E_{XC}}{\delta \rho(\mathbf{r})}$$

Kohn and Sham showed that solving Eq.(2.13) is equivalent to solving the following set of single-particle Schrödinger-like equations for the variational wave-functions of fictitious non-interacting electrons

$$\left[ -\frac{\hbar^2}{2m_e} \nabla^2 + V_{KS}(\mathbf{r}) \right] \phi_i = \epsilon_i \phi_i \quad (2.14)$$

where  $\phi_i$  and  $\epsilon_i$  are the single-particle wave-functions and eigenvalues, respectively, such that  $\rho(\mathbf{r}) = \sum_i^N \phi(\mathbf{r})^* \phi(\mathbf{r})$ . The Eq.(2.14), therefore, represents the set of Kohn-Sham self-consistent equations. Since  $V_H(\mathbf{r})$  and  $V_{XC}(\mathbf{r})$  depend on  $\rho$ , which depend on  $\phi_i$ , which in turn depend on  $V_{KS}(\mathbf{r})$ , the problem of solving the Kohn-Sham equations is not a straight-forward one. The usual way of solving such problems is the iterative procedure, *i.e.* to start with an initial guess for  $\rho(\mathbf{r})$ , calculate the corresponding  $V_{KS}(\mathbf{r})$ , and then solve the differential equation (Eq.(2.14)) for the  $\phi_i$ . From these one calculates a new density, and starts again. The process is repeated until it converges. Thus the procedure is called self-consistent cycle.

### 2.1.3.2 Exchange-correlation functional

The method proposed by Kohn-Sham, described above is exact, apart from the preceding Born-Oppenheimer approximation, and the fact that exact form of exchange-correlation functional is assumed to be known. In practice, the utility of the theory rests on the approximation used for  $E_{XC}[\rho]$ . A widely used approximation called the Local Density Approximation (LDA) is to postulate that the exchange-correlation functional has the following form:

$$E_{XC}^{LDA} = \int \rho(\mathbf{r}) \epsilon_{xc}(\rho(\mathbf{r})) d\mathbf{r} \quad (2.15)$$

Under the local density approximation,  $\epsilon_{xc}(\rho)$  assumed to be the exchange and correlation energy density of the homogeneous electron gas of density  $\rho$ . Within the LDA  $\epsilon_{xc}(\rho)$  is a function of only the local value of the density. It can be separated into exchange and correlation contributions;

$$\epsilon_{xc}(\rho) = \epsilon_x(\rho) + \epsilon_c(\rho)$$

Since the exchange energy of the homogeneous electron gas is known exactly [7, 8],  $\epsilon_x(\rho)$  takes the following form,

$$\epsilon_x(\rho) = -\frac{3e^2}{4} \left(\frac{3}{\pi}\right)^{1/3} \rho(\mathbf{r})^{1/3}$$

The functional form for the correlation energy density,  $\epsilon_c(\rho)$ , is unknown and has been simulated for the homogeneous electron gas in numerical quantum Monte Carlo calculations which yield essentially exact results[9]. The resultant exchange correlation energy has been fitted by a number of analytic forms [10, 11, 12] all of which yield similar results in practice and are collectively referred to as LDA functionals.

The next step towards the improvement of LDA is to include the information on how the density  $\rho(\mathbf{r})$  varies spatially in the functional. The exchange correlation functional which incorporate this improvement is known as Generalized Gradient Approximations (GGA)[13]. The general form of exchange correlation functional considered in such case is

$$E_{XC}^{GGA}[\rho] = \int f(\rho(\mathbf{r}), \nabla\rho(\mathbf{r})) d\mathbf{r}$$

Different GGAs differ in the choice of the function  $f(\rho, \nabla\rho)$ . The calculations presented in this thesis are mostly done using the functional proposed by Perdew, Burke and Ernzerhof in 1996, famously known as PBE[14]. There are many other forms of GGAs available, which are being used over the decades and new ones continue to appear[15, 16, 17, 18, 19].

In spite of quite accurate performance of LDA and different GGAs, the quest for more accurate functionals goes ever on and various beyond-GGA functionals have appeared. Like hybrid functionals which incorporate a portion of exact exchange from Hartree-Fock theory with exchange and correlation from other sources (such as LDA)[20]. Few of the most popular form of hybrid functionals are B3LYP (Becke, three-parameter, Lee-Yang-Parr) and HSE (Heyd-Scuseria-Ernzerhof)[21] etc.

### 2.1.3.3 Basis sets

To solve the single-particle Kohn-Sham Eq.(2.14) and to obtain the eigenvalues and eigenfunctions, a number of methods have been introduced. Regardless of different approaches, one has to choose an appropriate basis set to expand the single-particle wave-functions and depending on the choice of basis functions, different schemes, therefore, can be broadly grouped into two categories: (i) methods using energy independent basis sets or fixed basis sets, like tight binding method using linear combination of atomic orbitals (LCAO) type basis [22], pseudopotential method using plane wave basis [23], and (ii) methods using energy dependent basis set, like cellular method[24], augmented plane wave (APW) method[25] etc.

## 2.2 Overview of band-structure methods

In this thesis, general band-structure calculations reported are carried out using following methods in which different basis sets are incorporated.

- We have used plane wave based basis set as implemented in Vienna ab initio simulation package (VASP)[26, 27, 28]. The interaction between ions and electrons is described using ultra-soft pseudopotentials (US-PP)[29, 30] or the projector augmented wave method (PAW)[31, 32].
- Full-potential linearized augmented plane-wave (LAPW)[33] + local orbitals (lo)[34] method has also been used as when required as implemented in Wien2K[35] code.
- We have also used extensively tight binding linear muffin tin orbital (TB-LMTO)[36] method for first principle studies.
- We have also used Nth order muffin tin orbital (NMTO) downfolding technique[37] as implemented in the Stuttgart code, which goes beyond the scope of the standard TB-LMTO technique and succeeds in extracting the relevant information needed for the modeling of a complex crystalline solid from a full LDA calculation.

### 2.2.1 The Linear Muffin-tin Orbital Method

In order to evaluate the correct eigen states of the many electron Hamiltonian subject to real crystal potential, in a computationally more “efficient” and at the same time less “heavy” method, the Linear Muffin-tin Orbital (LMTO) method is a good choice. In this method muffin-tin approximation is used, in which the actual crystal potential is approximated in the following way (see the Fig. 2.1)

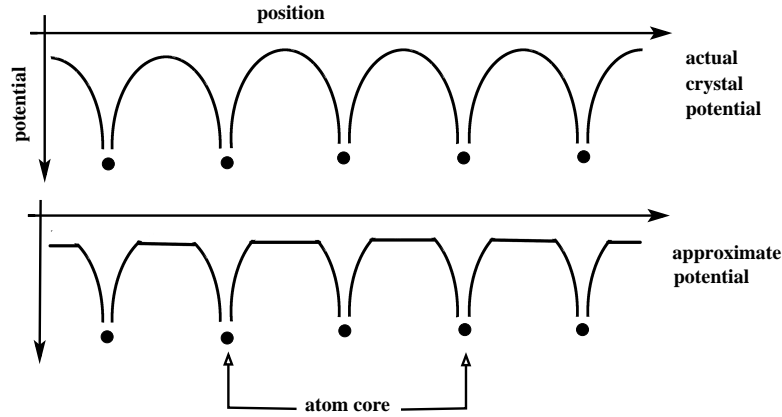


**Figure 2.1** Schematic diagram of potential inside real crystal and approximated potential considered in LMTO method. Potential is rapidly varying in the vicinity of core atomic region. In the interstitial region *ie.* away from atom core region, the actual potential is approximated as a constant potential.

The space inside the crystal is considered to be divided into two parts, atom-centered muffin tin spheres and the rest region as interstitial. The potential around each atom is treated as spherically symmetric within a radius  $S_R$  and in the interstitial region the potential is considered to be constant. Hence the potential is of the following form,

$$v(\vec{r}_R) = \begin{cases} v(r_R) & r_R \leq S_R, \vec{r}_R = |\vec{r} - \vec{R}| \\ -v_0 & r_R > S_R \end{cases}$$

Inside the spherically symmetric muffin tin sphere the rapidly varying part of wavefunction is represented by the radial solution of Schrödinger equation times spherical harmonics, known as partial

waves, which is given as

$$\phi(\vec{r}_R) = \varphi(r_R, \varepsilon) Y_L(\hat{r}_R)$$

Here  $L$  denotes the angular momentum labels  $(l, m)$ ,  $Y_L(\hat{r}_R)$  are the spherical harmonics functions and  $\hat{r}_R$  are the angular variables associated with the vector  $\vec{r}_R$ . This solution is regular at  $\vec{r} = \vec{R}$  and behaves like  $r_R^l$  as  $r_R \rightarrow 0$ . Outside the muffin-tin region the potential is assumed to be constant, and therefore the radial equation with a constant  $v_{r_R} = -v_0$  takes the following form,

$$\left[ \frac{d^2}{dr_R^2} + \frac{l(l+1)}{r_R^2} - \kappa^2 \right] r_R \varphi_{RL}(r_R, \varepsilon) = 0$$

where  $\kappa^2 = \varepsilon - v_0$ . Hence in the interstitial region the solution is plane waves, which can be expanded in terms of spherical Neumann and Bessel functions. It is needless to say that, the solutions must be continuous and smooth at the sphere boundary in order to have a “well-behaved” wavefunction. This particular method relies on atomic sphere approximation (ASA) which replaces the muffin tin spheres by space-filling atomic spheres, called Wigner-Seitz (WS) spheres. Incorporating this approximation, the information needed to set up the Hamiltonian can be divided into two independent parts. The first part contains the structure matrix which depends only on the structure and the positions of the atoms and not on the type of atoms occupying the sites. The solution of the Schrödinger equation inside each inequivalent WS sphere with appropriate boundary conditions forms the other part of the information.

Finally following Andersen’s approach of linearization [38], the LMTO basis functions within ASA can be expressed as:

$$\chi_{RL}^\alpha = \phi_{RL}(r_R) + \sum_{R'L'} \phi_{R'L'}^\alpha(r_{R'}) h_{R'L',RL}^\alpha \quad (2.16)$$

where  $L$  denotes collective angular momentum index (lm). The  $r_R$  is defined as  $\vec{r}_R = \vec{r} - \vec{R}$ , where atomic sites are given by the position vectors  $\vec{R}$ .  $\phi$  is the partial waves inside the WS sphere centered at  $\vec{R}$  for a energy of linearization  $\varepsilon_{v_{RL}}$ . The functions  $\dot{\phi}^\alpha$  are the linear combinations of the  $\phi$ ’s and their energy derivatives  $\dot{\phi}$ . The matrix  $h^\alpha$  is given by

$$h^\alpha = C^\alpha - \varepsilon_v + (\Delta^\alpha)^{1/2} S^\alpha (\Delta^\alpha)^{1/2} \quad (2.17)$$

where  $C$  and  $\Delta$  are the diagonal potential matrices. They depend on the potential inside the sphere,  $\alpha$  and on sphere radii.  $C$  and  $\Delta$  are commonly known as *band center* parameter and *band width*.  $S$  is the structure matrix depending on the representation and the geometrical arrangement of the atomic sites.

### 2.2.2 $N^{\text{th}}$ Order Muffin Tin Orbital (NMTO) - improved LMTO method

In order to calculate the single electron part - the orbitals, hopping integrals or on-site terms, from a correlated Hamiltonian, one needs to extract low energy, few band Hamiltonian out of the full Hamiltonian. Downfolding technique is the way to achieve this. In this technique, the space of a basis set is considered to be subdivided into two subsets, lower  $|l\rangle$  and  $|h\rangle$ . The reduction of the full Hamiltonian  $H$  into the lower subset Hamiltonian  $\tilde{H}_{ll}$  is carried out in such a manner that lower  $l$  eigenvalues of  $H$  and eigenvalues of  $\tilde{H}_{ll}$  are same. The formation of  $\tilde{H}_{ll}$  introduces additional energy dependence through the expression

$$\tilde{H}_{ll} = H_{ll} - H_{lh} (H_{hh} - \varepsilon)^{-1} H_{hl} \quad (2.18)$$

In LMTO method this scheme is implemented in the KKR equation, via the transformation of the structure matrix  $S^{\mathbf{k}}$  into  $\beta$  representation. The additional energy dependence is taken care of by the linearization procedure in construction of LMTO. Though the implementation of LMTO helps to resolve the problem of ghost bands, but it does not provide an accurate way to do a massive downfolding, where the downfolded bands span in a very narrow energy window. The disadvantages of LMTO methods are like,

- The basis is complete to  $(\varepsilon - \varepsilon_v)$  (*i.e.* 1<sup>st</sup> order) inside the sphere while it is only complete to  $(\varepsilon - \varepsilon_v)^0 = 1$  (0<sup>th</sup> order) in the interstitial, which is inconsistent. This inconsistency can be corrected by removing the interstitial region through introduction of ASA.
- For open-systems non-ASA corrections (combined correction) is also included in the Hamiltonian and in the overlap matrices, but,
  - This makes the formalism computationally heavy.
  - Basis must often be increased by multi-panel calculations.

- The expansion of the Hamiltonian  $H$  in the orthogonal representation as a power series in the two centred tight-binding Hamiltonian  $h$  :

$$\langle \chi | (H - \varepsilon_V) | \chi \rangle = h - hoh + \dots \quad (2.19)$$

is obtained only within ASA and excluding downfolding.

All these shortcomings have been taken care in  $N^{th}$  Order Muffin Tin Orbital (NMTO) method. This is a more consistent formalism, which overcomes the above-said shortcomings and provides a way to describe the downfolded band structure with better accuracy within a chosen energy range. This method treats the interstitial region accurately and goes beyond the linear approximation. It also uses the partial waves,  $\phi_{RL}\varepsilon, r_R$  within the atomic spheres. Instead of Neumann function, in this method screened spherical waves (SSWs) are considered in the interstitial region. The adoption of screening technique is discussed briefly.

It introduces a hard sphere of radius  $a$  and a phase shifted partial wave solution  $\phi_{RL}^{\alpha 0}(\varepsilon, r_R)$  (green line in Fig. ), which matches the value and slope of  $\phi$  at  $S_R$ , but their curvature differ. At the hard sphere,  $\phi_{RL}^{\alpha 0}(\varepsilon, r_R)$  is joined continuously but with a kink to the SSW,  $\phi_{RL}^{\alpha}(\varepsilon, r)$ , shown by blue line in Fig. . The combined form of these contributions is known as Kink Partial Waves (KPWs), which is given as

$$\psi_{RL}^{\alpha}(\varepsilon, r_R) = [\phi_{RL}^{\alpha}(\varepsilon, r_R) - \phi_{RL}^{\alpha 0}(\varepsilon, r_R)] Y_L(\hat{r}_R) + \phi_{RL}^{\alpha}(\varepsilon, r)$$

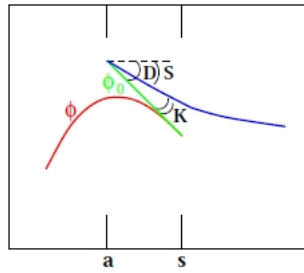


**Figure 2.2** Construction of Kink partial wave (KPW),  $\phi$ ,  $\phi_0$  and  $\phi_K$ .

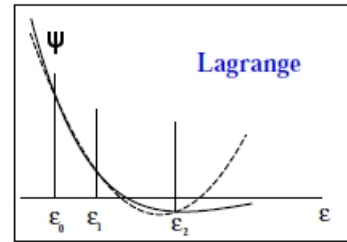


**Figure 2.3**  $N^{th}$  order approximation to the energy dependence of a partial wave for a discrete (Lagrange) mesh.

The members of NMTO basis set  $\chi_{R'L'}^N$  is constructed by Lagrange interpolation of  $\psi_{RL}^\alpha(\epsilon, r_R)$  evaluated at the energy points  $\epsilon_0, \dots, \epsilon_N$  (see Fig. ),

$$\chi_{R'L'}^N = \sum_{n=0}^N \sum_{RL \in A} \psi_{RL}^\alpha(\epsilon_n, r_R) L_{n,RL,R'L'}^{(N)}$$

Thus the construction of basis set is energy selective, as well as localized in nature. The energy selective nature of the basis set provides the way to select a narrow energy window from full LDA band structure accurately. This procedure naturally takes into account the re-normalization effect due to the integrated-out orbitals by defining energy-selected, effective orbitals which serve as Wannier-like orbitals for the few-orbital Hamiltonian in the downfolded representation. The real-space representation of the downfolded Hamiltonian in the basis of downfolded NMTOs provide information on effective hopping, which we have used extensively in our first-principle study.

### 2.2.3 The Pseudopotential Method

Electrons at the outermost shell of an atom usually take part in the chemical bonding, and there by control chemical and physical properties of the system, while those forming the inner shells do not participate actively. This leads to the idea behind the pseudopotential theory. Let us denote core and valance state of single-particle Kohn-Sham equation (Eq.(2.14))  $\psi^c$  and  $\psi^v$  respectively. A new set of single-particle valance states  $\tilde{\phi}^v$  can be defined as

$$\psi^v(\vec{r}) = \tilde{\phi}^v + \sum_c \alpha_c \psi^c(\vec{r}) \quad (2.20)$$

The coeff.  $\alpha_c$ s are determined using the condition that  $\psi^c$  and  $\psi^v$  are orthogonal to each other. Using Eq.(2.20), one can write the Eq.(2.14) in a different form:

$$\left[ -\frac{\hbar^2}{2m_e} \nabla^2 + V_{KS} + \sum_c (\epsilon^v - \epsilon^c) |\psi^c\rangle \langle \psi^c| \right] \tilde{\phi}^v = \epsilon^v \tilde{\phi}^v \quad (2.21)$$

The operator  $V_{PS} \equiv V_{KS} + \sum_c (\epsilon^v - \epsilon^c) |\psi^c\rangle \langle \psi^c|$ , represents a weak attractive potential and is called a pseudopotential. The new states  $\tilde{\phi}^v$  obey a single-particle equation with a modified potential, but have the same eigenvalues  $\epsilon^v$  as the original valance state  $\psi^v$ . This new set of valance state experience a

weaker potential near the atomic nucleus, but the proper ionic potential away from the core region. Since it is this region in which the valence electrons interact to form bonds that hold the solid together, the pseudo-wavefunctions preserve all the important physics relevant to the behaviour of the solid.

Since last few decades several successful attempts have been made to generate more accurate as well as more efficient pseudo-potentials, keeping the basic principles same. In norm-conserving pseudopotential [39] scheme, inside some core radius, the all electron (AE) wave function is replaced by a soft nodeless pseudo (PS) wave function, subject to the condition that within the chosen core radius the norm of the PS wave function has to be the same with the AE wave function and outside the core radius both the wave functions are identical. However, the charge distribution and moments of AE wave function are well reproduced by the PS wave function only when the core radius is taken around the outer most maximum of AE wave function. This in practice makes the situation for strongly localized orbitals like  $3d$  and rare-earth elements, complicated as the resulting pseudopotentials require a large plane-wave basis set. This situation was remarkably improved by Vanderbilt [29] by introduction of ultra-soft pseudopotential. According to the scheme proposed by him the norm conservation constraint was relaxed and a localized atom centered augmentation charges were introduced to make up the charge deficit. These augmentation charges are defined as the charge density difference between the AE and the PS wavefunction. Only for the augmentation charges, a small cutoff radius must be used to restore the moments and the charge distribution of the AE wavefunction accurately. But the success of this particular approach is partly hampered by rather difficult construction of the pseudopotential.

#### **2.2.4 The Linearized Augmented Plane Wave + local orbital method**

In spite of the fact that pseudopotential methods are extremely useful, if one is interested in information that is inherently contained in the region near the nucleus (for example hyperfine splitting or core level excitation), pseudopotential methods may not be the primary choice. In such cases Augmented Plane Wave (APW) basis set can be more useful. In the region far away from the nuclei, the electrons are relatively delocalized and thus can be described by plane waves. On the other hand, close to the nuclei, the electrons behave in a localized manner confined in an isolated atom. In such case atomic like

functions can describe the behaviour of the electrons more efficiently. Therefore the space can be treated as divided into two regions, like we discussed for LMTO method in Subsection 2.2.1. Around each atom a sphere of radius  $R_\alpha$  is considered and such spheres are usually referred as *muffin tin spheres* ( $S_\alpha$ ). The remaining space is called as *interstitial region* ( $I$ ). One augmented plane wave (APW) used in the expansion of  $\phi_{\vec{k}}$  is defined as

$$\phi_{\vec{k}}^{\vec{G}}(\vec{r}, E) = \begin{cases} \frac{1}{\sqrt{\Omega}} e^{i(\vec{k}+\vec{G})\cdot\vec{r}} & \vec{r} \in I \\ \sum_{l,m} A_{lm}^{\alpha,\vec{k}+\vec{G}} u_l^\alpha(r', E) Y_m^l(\theta', \phi') & \vec{r} \in S_\alpha \end{cases} \quad (2.22)$$

The symbols  $\vec{k}$ ,  $\vec{G}$  and  $\vec{r}$  have their usual meaning and  $\Omega$  represents the volume of the unit cell. Each atom inside the unit cell is labelled by  $\alpha$ , hence this label is different for all atoms in the unit cell, not just for all inequivalent atoms. The position inside the spheres is given with respect to the center of each sphere by  $\vec{r}' = \vec{r} - \vec{r}_\alpha$ .  $\theta'$  and  $\phi'$  are the spherical polar angles indicating the direction of  $\vec{r}'$ . The  $Y_m^l$  are the spherical harmonics. The  $A_{lm}^{\alpha,\vec{k}+\vec{G}}$  are parameters to be determined. The  $u_l^\alpha$  are solutions to the radial part of the Schrödinger equation for an isolated atom  $\alpha$  at the energy  $E$ . The well-known condition for “well-behaved” wave function is that the solution must be continuous at the boundary. This is not a obvious thing, as because a plane wave is oscillating in nature and has a unique direction built in. Therefore to match it with another function based on spherical harmonics over the entire surface of a sphere, is not straightforward. Let us expand the plane wave in spherical harmonics about the origin of the sphere of atom  $\alpha$  in the following way.

$$\frac{1}{\sqrt{\Omega}} e^{i(\vec{k}+\vec{G})\cdot\vec{r}} = \frac{4\pi}{\sqrt{\Omega}} e^{i(\vec{k}+\vec{G})\cdot\vec{r}_\alpha} \sum_{l,m} i^l j_l(|\vec{k}+\vec{G}||\vec{r}'|) Y_m^l(\vec{k}+\vec{G}) Y_m^l(\theta', \phi') \quad (2.23)$$

where  $j_l$  is the Bessel function of order  $l$ . The boundary condition *ie.* two functions of Eq.(2.22) to be continuous at the sphere surface helps to uniquely determine  $A_{lm}^{\alpha,\vec{k}+\vec{G}}$ . In principle there are an infinite number of terms in Eq.(2.23). Therefore one can use infinite number of  $A_{lm}^{\alpha,\vec{k}+\vec{G}}$  to create a good matching between the two functions. In practice one have to truncate at some value  $l_{max}$ . A practically used condition is that  $R_\alpha G_{max} = l_{max}$ , where  $G_{max}$  is the cut-off for plane waves. This allows to determine a good  $l_{max}$  for a given  $G_{max}$ .

Till now the basis set functions are dependent on energy  $E$ . Linearization of APW method *ie.* *Linearized Augmented Plane Wave* (LAPW) helps to get rid of this problem. If one can determine  $u_l^\alpha$  at some energy  $E_0$ , then one could make a Taylor expansion to find it at energies not far away from it:

$$u_l^\alpha(r', E) = u_l^\alpha(r', E_0) + (E_0 - E) \underbrace{\frac{\partial u_l^\alpha(r', E)}{\partial E}}_{\dot{u}_l^\alpha(r', E_0)} \Big|_{E=E_0} + O(E_0 - E)^2 \quad (2.24)$$

Substituting the first two terms of the expansion in the APW for a fixed  $E_0$  gives the definition of an LAPW. Since  $(E_0 - E)$  in the second term is unknown, hence another coeff.  $B_{lm}^{\alpha, \vec{k}+\vec{G}}$  has to be introduced.

$$\phi_{\vec{G}}^{\vec{k}}(\vec{r}, E) = \begin{cases} \frac{1}{\sqrt{\Omega}} e^{i(\vec{k}+\vec{G})\cdot\vec{r}} & \vec{r} \in I \\ \sum_{l,m} \left( A_{lm}^{\alpha, \vec{k}+\vec{G}} u_l^\alpha(r', E) + B_{lm}^{\alpha, \vec{k}+\vec{G}} \dot{u}_l^\alpha(r', E) \right) Y_m^l(\theta', \phi') & \vec{r} \in S_\alpha \end{cases} \quad (2.25)$$

In order to determine both the coefficients, one need to match both the value and the slope of the functions at the boundary. It is worth to mention that one should not choose an universal  $E_0$ . Rather for every physically important  $l$  (s,p,d and f states, *i.e.* up to  $l = 3$ ) and for every atom one should choose  $E_l^\alpha$ . Electronic states that are extremely well bound to the nucleus (for example,  $1s$  state of Cu) behave almost exactly as if it were in a free atom. This means such a state does not participate directly in chemical bonding with other atoms. Such states are called as *core states* and must be contained entirely in the muffin tin sphere. States that leak out of the muffin tin sphere, are called *valence states*. Since only valance states take part in chemical bonding, so to make the numerical method computationally less heavy it is preferable to treat only valance states. Core states are treated as in free atoms, but subject to the potential due to the valance states.

While applying this in practice, it frequently happens that states with the same  $l$  but a different principal quantum number  $n$  are both valance states. Now in such cases it is not very clear how to choose  $E_l^\alpha$ . This dilemma is solved by adding another type of basis function to the LAPW basis set, called a *local orbital* (LO). A local orbital is defined as:

$$\phi_{lm,LO}^{\alpha}(\vec{r}) = \begin{cases} 0 & \vec{r} \notin S_{\alpha} \\ \left( A_{lm}^{\alpha,LO} u_l^{\alpha}(r', E_{1,l}^{\alpha}) + B_{lm}^{\alpha,LO} \dot{u}_l^{\alpha}(r', E_{1,l}^{\alpha}) + C_{lm}^{\alpha,LO} u_l^{\alpha}(r', E_{2,l}^{\alpha}) \right) Y_m^l(\theta', \phi') & \vec{r} \in S_{\alpha} \end{cases} \quad (2.26)$$

A local orbital is defined for a particular  $l$  and  $m$ , and for a particular atom  $\alpha$ . It is zero in the interstitial region and in the muffin tin spheres of other atoms, hence its name *local orbital*. In the above expression  $E_{1,l}^{\alpha}$  is the linearization energy value suitable for the state with higher  $l$  value among the two valence states. The lower valence state which is much more free-atom-like, is sharply peaked at an energy  $E_{2,l}^{\alpha}$ . Therefore a single radial function  $u_l^{\alpha}(r', E_{2,l}^{\alpha})$  at that same energy is sufficient to describe it. These three coefficients  $A_{lm}^{\alpha,LO}$ ,  $B_{lm}^{\alpha,LO}$  and  $C_{lm}^{\alpha,LO}$  in Eq.(2.26), are determined by the condition that the LO is normalized, and has zero value and zero slope at the muffin tin boundary. Adding local orbitals increases the LAPW basis set size, which in turn increases the computational time. But this small price is paid for the much better accuracy that local orbitals offer, and therefore they are always used.

### 2.2.5 The Projector-Augmented-Wave Formalism

P. E. Blöchl in 1994, developed the projector-augmented- wave (PAW) method, which combines the linear augmented plane wave method with the plane wave pseudopotential approach. This method turned out to be computationally elegant, transferable and accurate method for electronic structure calculation. Later Kresse and Joubert [31] modified this PAW method and implemented within the plane wave code of VASP.

In this formalism, the AE wavefunction  $\Psi_n$  is derived from the PS wavefunction  $\tilde{\Psi}_n$  by means of a linear transformation:

$$|\Psi_n\rangle = |\tilde{\Psi}_n\rangle + \sum_i (|\phi_i\rangle - |\tilde{\phi}_i\rangle) \langle \tilde{p}_i | \tilde{\Psi}_n \rangle \quad (2.27)$$

The index  $i$  is a shorthand for the atomic site at  $\vec{R}_i$ . The all electron partial waves  $\phi_i$  are the solutions of the radial Schrödinger equation for the isolated atom. The PS partial waves  $\tilde{\phi}_i$  are equivalent to the AE partial waves outside a core radius  $r_c^l$ . Of course these two wavefunctions match both in value and

slope at the boundary  $r_c^l$ . The projector function  $\tilde{p}_i$  for each PS partial wave localized within the core radius, obeys the relation  $\langle \tilde{p}_i | \tilde{\phi}_j \rangle = \delta_{ij}$ . From Eq.(2.27), the AE charge density in PAW method can be written as,

$$\rho(\vec{r}) = \tilde{\rho}(\vec{r}) + \rho^1(\vec{r}) - \tilde{\rho}^1(\vec{r}) \quad (2.28)$$

where  $\tilde{\rho}$  is the soft pseudo-charge density calculated directly from the pseudo wavefunctions on a plane wave grid. The on-site charge densities  $\rho^1$  and  $\tilde{\rho}^1$  are treated on radial support grids localized around each atom. It should be mentioned that the charge density  $\tilde{\rho}^1$  is exactly the same as  $\rho^1$  within the augmentation spheres around each atom. In PAW approach, an additional density, called compensation charge density is added to both auxiliary densities  $\rho^1$  and  $\tilde{\rho}^1$  so that the multi-pole moments of the terms  $\rho^1 - \tilde{\rho}^1$  in Eq.(2.28) vanish. Thus the electrostatic potential due to these terms vanishes outside the augmentation spheres around each atom, just as is accomplished in LAPW method. Like density, the energy can also be written as a sum of three terms and by functional derivatives of the total energy, one can derive the expressions of Kohn-Sham equations.

# Bibliography

- [1] M. Born and J. R. Oppenheimer, *Ann. Physik* **84**, 457 (1927).
- [2] D. R. Hartree, *Mathematical Proceedings of the Cambridge Philosophical Society* **24**, 426–437 (1928).
- [3] V. Fock, *Z. Phys.* 61 (1930).
- [4] C. D. Sherrill and H. F. S. III, “The Configuration Interaction Method: Advances in Highly Correlated Approaches,” in *The Configuration Interaction Method: Advances in Highly Correlated Approaches*, Vol. 34 of *Advances in Quantum Chemistry*, M. C. Z. Per-Olov Lowdin, John R. Sabin and E. Brandas, eds., (Academic Press, 1999), pp. 143 – 269.
- [5] P. Hohenberg and W. Kohn, *Phys. Rev.* **136**, B864–B871 (1964).
- [6] W. Kohn and L. J. Sham, *Phys. Rev.* **140**, A1133–A1138 (1965).
- [7] R. M. Dreizler and E. K. U. Gross, *Density Functional Theory* (Springer, Berlin, 1990).
- [8] R. G. Parr and W. Yang, *Density-Functional Theory of Atoms and Molecules* (Oxford University Press, Oxford, 1989).
- [9] D. M. Ceperley and B. J. Alder, *Phys. Rev. Lett.* **45**, 566–569 (1980).
- [10] J. P. Perdew and A. Zunger, *Phys. Rev. B* **23**, 5048–5079 (1981).
- [11] U. v. Barth and L. Hedin, *J. Phys. C: Solid State Phys.* **5**, 1629–1642 (1972).

- 
- [12] S. H. Vosko, L. Wilk, and M. Nusair, *Canadian Journal of Physics* **58**, 1200–1211 (1980).
- [13] J. P. Perdew and W. Yue, *Phys. Rev. B* **33**, 8800–8802 (1986).
- [14] J. P. Perdew, K. Burke, and M. Ernzerhof, *Phys. Rev. Lett.* **77**, 3865–3868 (1996).
- [15] A. D. Becke, *Phys. Rev. A* **38**, 3098–3100 (1988).
- [16] C. Lee, W. Yang, and R. G. Parr, *Phys. Rev. B* **37**, 785–789 (1988).
- [17] J. P. Perdew, J. A. Chevary, S. H. Vosko, K. A. Jackson, M. R. Pederson, D. J. Singh, and C. Fiolhais, *Phys. Rev. B* **46**, 6671–6687 (1992).
- [18] B. Hammer, L. B. Hansen, and J. K. Nørskov, *Phys. Rev. B* **59**, 7413–7421 (1999).
- [19] Z. Wu and R. E. Cohen, *Phys. Rev. B* **73**, 235116 (2006).
- [20] A. D. Becke, *The Journal of Chemical Physics* **98**, 1372–1377 (1993).
- [21] J. Heyd, G. E. Scuseria, and M. Ernzerhof, *The Journal of Chemical Physics* **118**, 8207–8215 (2003).
- [22] J. C. Slater and G. F. Koster, *Phys. Rev.* **94**, 1498–1524 (1954).
- [23] J. C. Phillips and L. Kleinman, *Phys. Rev.* **116**, 287–294 (1959).
- [24] E. Wigner and F. Seitz, *Phys. Rev.* **46**, 509–524 (1934).
- [25] T. L. Loucks, *Augmented plane wave method* (W.A. Benjamin, New York, 1967).
- [26] G. Kresse and J. Hafner, *Phys. Rev. B* **47**, 558 (1993).
- [27] G. Kresse and J. Hafner, *Phys. Rev. B* **49**, 14251 (1994).
- [28] G. Kresse and J. Furthmüller, *Phys. Rev. B* **54**, 11169 (1996).
- [29] D. Vanderbilt, *Phys. Rev. B* **41**, 7892 (1990).

- 
- [30] G. Kresse and J. Hafner, *J. Phys.: Condens. Matter* **6**, 8245 (1994).
- [31] G. Kresse and D. Joubert, *Phys. Rev. B* **59**, 1758 (1999).
- [32] P. E. Blöchl, *Phys. Rev. B* **50**, 17953 (1994).
- [33] O. Jepsen, J. Madsen, and O. K. Andersen, *Phys. Rev. B* **18**, 605–615 (1978).
- [34] D. Singh, *Phys. Rev. B* **43**, 6388–6392 (1991).
- [35] P. Blaha, K. Schwarz, G. Madsen, D. Kvasnicka, and J. Luitz, in *WIEN2k, An Augmented Plane Wave + Local Orbitals Program for Calculating Crystal Properties*,
- [36] O. K. Andersen and O. Jepsen, *Phys. Rev. Lett.* **53**, 2571–2574 (1984).
- [37] O. K. Andersen and T. Saha-Dasgupta, *Phys. Rev. B* **62**, R16219–R16222 (2000).
- [38] O. K. Andersen, *Phys. Rev. B* **12**, 3060–3083 (1975).
- [39] D. R. Hamann, M. Schlüter, and C. Chiang, *Phys. Rev. Lett.* **43**, 1494–1497 (1979).

## Chapter 3

# Proposed Orbital Ordering in $\text{MnV}_2\text{O}_4$ <sup>†</sup>

### 3.1 Background

Inherent geometric frustration present in spinel systems have made this class of compounds to be a potential candidate for study of magnetic, orbital and charge ordering in recent years [1].  $\text{MnV}_2\text{O}_4$  shows a complex behaviour including structural transitions from cubic to tetragonal symmetries which are often accompanied by an orbital order-disorder transition as well as complicated magnetic orderings at low temperatures. New experimental observations in single crystals [2] of  $\text{MnV}_2\text{O}_4$  has revealed a lower symmetry structure than previously suggested [3]. This has important implications for the related orbital order at low temperatures which is still under study. In  $\text{MnV}_2\text{O}_4$  both the A (Mn) and B (V) site ions are magnetic with  $S=5/2$  and 1 respectively. The presence of two magnetic ions in this system makes the magnetic phase transition more complicated than in other vanadium spinel oxides such as  $\text{ZnV}_2\text{O}_4$ ,  $\text{MgV}_2\text{O}_4$ , or  $\text{CdV}_2\text{O}_4$  with nonmagnetic A-site ions [3, 2, 4].  $\text{MnV}_2\text{O}_4$  undergoes a phase transition from paramagnetic to a collinear ferrimagnetic phase at 56 K where the Mn and V spin moments point in opposite directions. At  $T = 53$  K a second magnetic phase transition to noncollinear ferrimagnetism follows, accompanied by a structural transition from cubic to tetragonal phase.

---

<sup>†</sup>This chapter is based on *Phys. Rev. Lett.* 102, 216405 (2009)

## 3.2 Motivation the present work

The cubic to tetragonal structural transition in  $\text{MnV}_2\text{O}_4$  is associated with a compression of the  $\text{VO}_6$  octahedron ( $c_T/a_T=0.98$ ) which is similar to the vanadium spinel compound  $\text{ZnV}_2\text{O}_4$ . Although it should be mentioned that there are examples of spinel compounds where this tetragonal phase is elongated, like  $\text{CoMn}_2\text{O}_4$ [5],  $\text{Mn}_3\text{O}_4$ [6]. The octahedral environment of V ( $\text{VO}_6$ ) splits the  $d$  states into low lying  $t_{2g}$  and high lying  $e_g$ .  $\text{V}^{3+}$  in this compound is in a  $3d^2$  configuration. Hence the V- $t_{2g}$  orbitals are partially filled giving rise to the possibility of orbital ordering. Earlier experimental observations [3] indicated the low temperature structure belongs to tetragonal space group  $I4_{1/amd}$ . Although recent precise experiments on single crystal [2, 4] reports that this tetragonal space group to be  $I4_{1/a}$ . The orbital order and, accordingly, the magnetic order are closely related to the underlying space group symmetry. Therefore it is very important to establish the space group symmetry unambiguously. The  $I4_{1/a}$  space group breaks the mirror and glide symmetries present in the  $I4_{1/amd}$  space group. This implies that two of the four V-O bonds in the  $ab$  plane are shorter whereas in  $I4_{1/amd}$  symmetry all four V-O bond lengths are the same.

Garlea *et al.* [2] proposed a staggered A-type orbital ordering for this system based on their observations of the structural and magnetic phases at low temperature. Suzuki *et al.* [4] also proposed a similar ordering as mentioned previously. The magnetic structure at low temperatures has been unambiguously established by the above-mentioned experiments. In spite of that, it is worth to note that there has not yet been any experiment such as x-ray resonant spectroscopy to directly probe the orbital order. Determination of exchange couplings using neutron scattering techniques by Chung *et al.* [7] is in apparent contradiction with the proposed staggered A-type orbital ordering. As pointed out by these authors, the above mentioned proposed orbital order lacks the consideration of trigonal distortion, which is found to be strongest in  $\text{MnV}_2\text{O}_4$  among all the vanadium spinels. The trigonal distortion has been often shown to have significant effects on the orbital order [8, 9]. Therefore the underlying orbital

---

$c_T$  and  $a_T$  are the lattice parameters in tetragonal phase.

The angle between apical O, V and any one of the four O ions in  $ab$  plane should have been  $90^\circ$  in ideal  $\text{VO}_6$ , but in practice this angle deviates from the ideal value. This kind of distortion is commonly known as trigonal distortion.

ordering in  $\text{MnV}_2\text{O}_4$  can be much more complicated than what is reported in literature. Determination of correct crystal symmetry is very crucial in order to find out the underlying orbital ordering. We have discussed earlier, that first principles calculations can be carried out in order to theoretically optimizing crystal structure efficiently. Therefore first principles calculations can be employed to get a clear picture regarding the low temperature crystal structure symmetry of  $\text{MnV}_2\text{O}_4$ . Also the magnetic exchange interactions ( $J_s$ ) can be determined successfully, at least the relative magnitude of  $J_s$ , from first principle calculations. Hence the orbital ordering and corresponding magnetic exchange interactions can be studied from first principles point of view.

### 3.3 Results and Discussions

#### 3.3.1 Structural Optimization

In order to study the orbital ordering at low temperature, one needs to settle down the issue of space group of low temperature structure. In order to investigate the relative stability between  $I4_{1/amd}$  and  $I4_{1/a}$  symmetries in  $\text{MnV}_2\text{O}_4$ , we performed a structural optimization using the plane wave method as implemented in the Vienna ab-initio simulation package (VASP). In our calculations we have considered different exchange-correlation functional like local spin density approximation (LSDA), generalized gradient approximation (GGA), and LSDA +  $U$ . Following are the few details of parameters used in our optimization calculation. We used projector augmented wave (PAW) potentials, and the wave functions were expanded in the plane wave basis with a kinetic energy cutoff of 450 eV. Reciprocal space integration was carried out with a k mesh of  $6 \times 6 \times 6$ .

Mn and V in this compound occupy the high symmetry  $4a$  and  $8d$  positions. Therefore the calculation essentially involves optimization of the internal degrees of freedom associated with O. Spin arrangement considered is of ferrimagnetic type with Mn and V spins pointing opposite to each other. Calculations done within LSDA as well as GGA gave us a ground state structure of  $I4_{1/amd}$  symmetry. In literature it has already been reported that electron-electron correlation influences the structural optimization in a quite significant way[10, 11]. We have further optimized the atomic positions within the

	LDA	GGA	LSDA+U
Mn	0.0 0.25 0.125	0.0 0.25 0.125	0.0 0.25 0.125
V	0.0 0.0 0.5	0.0 0.0 0.5	0.0 0.0 0.5
O	0.0 0.0243 0.7392	0.0 0.0236 0.7394	0.0059 0.0244 0.7383

**Table 3.1** Energy-minimized structural parameters of  $\text{MnV}_2\text{O}_4$ . Lattice constants have been kept constant at the experimental value [3]. Numbers quoted under LSDA+U are obtained using  $U=4.5$  eV.

LSDA +  $U$  approach with different choices of  $U$  values ( $U = 0.5, 1, 2, 3, 4.5,$  and  $6$  eV) for both Mn and V.  $J$  was chosen to be 1 eV for all calculations. Mn and V are neighbors in the periodic table and it is not to be expected that their  $U$  values will be very different. This is the reason why we considered same  $U$  value for both Mn and V in our calculation. Remarkably, it has been seen that with the consideration of  $U$  beyond 2 eV, the  $I4_{1/a}$  symmetry becomes the ground state structure. Table 3.1 shows the ion positions of ground state structures.

The LSDA +  $U$  optimized structural parameters show the O  $x$  coordinate to be nonzero, signaling the change of space group symmetry to  $I4_{1/a}$ . The O in  $I4_{1/a}$  are in  $16f$  positions with nonzero  $x$  coordinate, and this breaks the mirror and glide symmetry compared to the alternative proposed candidate  $I4_{1/amd}$ . Not only that this non-zero  $x$  coordinate of O makes the V-O bond lengths even in the  $ab$  plane to be unequal (see Fig. 3.1). This lowering of symmetry necessarily breaks the degeneracy of the  $t_{2g}$  states completely and also introduces mixing between different  $t_{2g}$  states, which will be discussed later in detail. It should be mentioned that the optimized structure under LSDA +  $U$  shows a tetragonal distortion close to the experimentally reported one [3]. Undoubtedly these results indicate the importance of correlation effects for the description of the correct orbital ordering and the low temperature structure. As mentioned above, we have used different  $U$  values for structural optimization and for each of ground state structures we have determined the orbital and spin moment of individual ions. Among all the theoretically optimized structures,  $U= 4.5$  eV gives the closest comparison to the experimental result. All further calculations are done considering this particular structure corresponding to  $U=4.5$

eV.

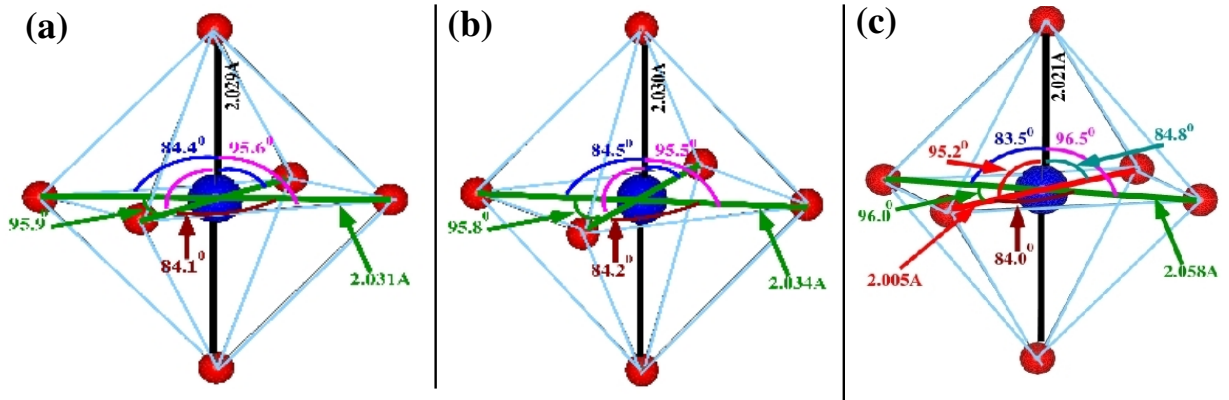


**Figure 3.1**  $\text{VO}_6$  octahedral unit of optimized structure, calculated within LDA, GGA and LSDA+ $U$  (from left to right) respectively. Different color of V-O bond indicates different bond length. Note that for only LSDA+ $U$  optimized  $\text{VO}_6$  unit V-O bond lengths on  $ab$  plane are also different.

### 3.3.2 Density of states and band structure

$\text{Mn}^{2+}$  ( $d^5$ ) ion in  $\text{MnV}_2\text{O}_4$  remains in high-spin (HS) configuration, with completely filled  $d$  states in one spin channel and completely empty in other spin channel. On the other hand  $\text{V}^{3+}$  ( $d^2$ ) has two electrons in its majority spin channel. Therefore only the majority spin channel is important as because in minority spin channel either V- $d$  states are completely empty or Mn- $d$  states are completely occupied.

From the Fig. 3.2 one can see that V- $d$  states have split into two main groups,  $t_{2g}$  (consisting of  $x^2 - y^2$ ,  $xz$  and  $yz$ ) and  $e_g$  (consisting of  $3z^2 - 1$  and  $xy$ ). Although the usual convention is that  $t_{2g}$  states are consist of  $xy$ ,  $yz$  and  $xz$  orbitals, and the  $x^2 - y^2$  and  $3z^2 - 1$  orbitals form  $e_g$  sub-group. This apparently different convention because of the fact that there is  $45^\circ$  rotation in  $ab$  plane between local and global coordinate systems. Fig. 3.3 shows the five  $d$  orbitals, if there is a  $45^\circ$  rotation in  $xy$  plane of co-ordinate system,  $x^2 - y^2$  and  $xy$  orbital will interchange their shape. Inclusion of correlation effects in the V  $d$  orbitals through the LSDA +  $U$  approach splits the  $t_{2g}$  states further and opens a gap of 1.1

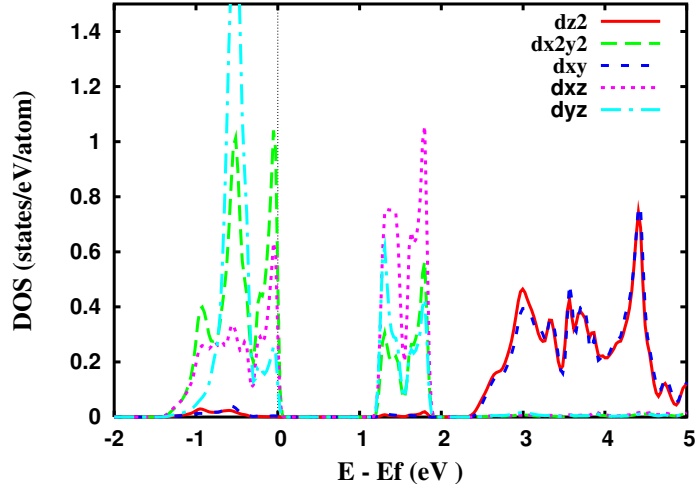


**Figure 3.2** V- $d$  partial DOS calculated within LSDA+ $U$ , for  $U=4.5$  eV. Only the DOS for the majority spin channel is shown (the minority spin channel is unoccupied). Energy plotted along x-axis is with respect to Fermi energy ( $E_f$ ).

eV. The degeneracy between all the three  $t_{2g}$  orbitals is lifted in the low symmetry  $I4_{1/a}$  group. All the three  $t_{2g}$  states are partially filled with more occupancy in  $x^2 - y^2$  and  $yz$  orbitals compared to that of  $xz$  orbital.

This becomes more evident from  $t_{2g}$  band structure in majority spin channel, shown in Fig. 3.4. The  $t_{2g}$  bands are well separated from occupied O- $p$  dominated bands by a gap of 1.5 eV and from unoccupied  $e_g$ -like bands by a gap of 0.2 eV. The fatness of the bands in Fig. 3.4 represents the projected band characters of  $x^2 - y^2$ ,  $xz$  and  $yz$  orbitals. It is evident from the band structure that significant mixing between the  $t_{2g}$  orbitals happens due to the lower symmetry in  $I4_{1/a}$ .

### 3.3.3 NMTO-downfolding calculation

We have performed NMTO-downfolding [12] calculations to construct a V- $d$  only low energy Hamiltonian by integrating out other degrees of freedom, starting with a full LSDA+ $U$  Hamiltonian. Diagonalization of on-site block of the Hamiltonian can provide information regarding the precise V orbital composition. Following are the eigen-states of  $5 \times 5$  on-site block of Hamiltonian, corresponding to

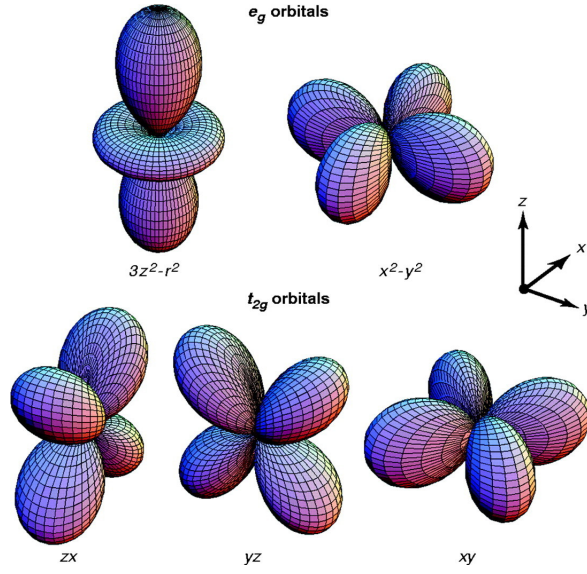


**Figure 3.3** Sub-grouping of five  $d$  orbitals under octahedral crystal field splitting. If  $xy$  plane is rotated by  $45^\circ$  then  $x^2 - y^2$  and  $xy$  orbital should interchange their position in the above diagram. Figure is taken from Tokura *et al.* Science **288**, 462 (2000).

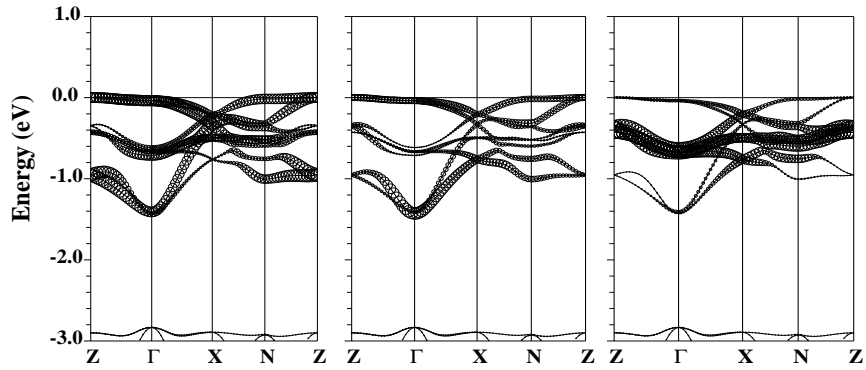


**Figure 3.4** LSDA +  $U$  band structure of  $\text{MnV}_2\text{O}_4$  projected onto  $V$ - $x^2 - y^2$ ,  $xz$ , and  $yz$  character (from left to right)

the eigen-values arranged in ascending order.

$$\begin{aligned}
 |1\rangle &= 0.78|x^2 - y^2\rangle - 0.59|xz\rangle - 0.21|yz\rangle + 0.07|xy\rangle + 0.02|3z^2 - 1\rangle \\
 |2\rangle &= -0.35|x^2 - y^2\rangle - 0.15|xz\rangle - 0.92|yz\rangle - 0.09|xy\rangle - 0.07|3z^2 - 1\rangle \\
 |3\rangle &= 0.52|x^2 - y^2\rangle - 0.79|xz\rangle - 0.31|yz\rangle - 0.13|xy\rangle + 0.02|3z^2 - 1\rangle \\
 |4\rangle &= 0.05|x^2 - y^2\rangle - 0.08|xz\rangle - 0.11|yz\rangle + 0.66|xy\rangle + 0.74|3z^2 - 1\rangle \\
 |5\rangle &= -0.02|x^2 - y^2\rangle - 0.11|xz\rangle + 0.04|yz\rangle - 0.73|xy\rangle + 0.67|3z^2 - 1\rangle
 \end{aligned}$$

The lowest energy state has predominant  $x^2 - y^2$  character along with a significant mixing of  $xz$  character. This is expected due to the trigonal distortion with the compression of  $\text{VO}_6$  octahedron along the  $c$  direction. The next higher energy state is dominated by  $yz$  character. Therefore, the second electron of  $\text{V}^{3+}$  always occupies the orbital with predominant  $yz$  character in all V sites. From our calculation it is evident that an alternating occupation of  $xz$  and  $yz$  orbitals at the V sites is not a correct picture in this scenario.

### 3.3.4 Charge-density calculation

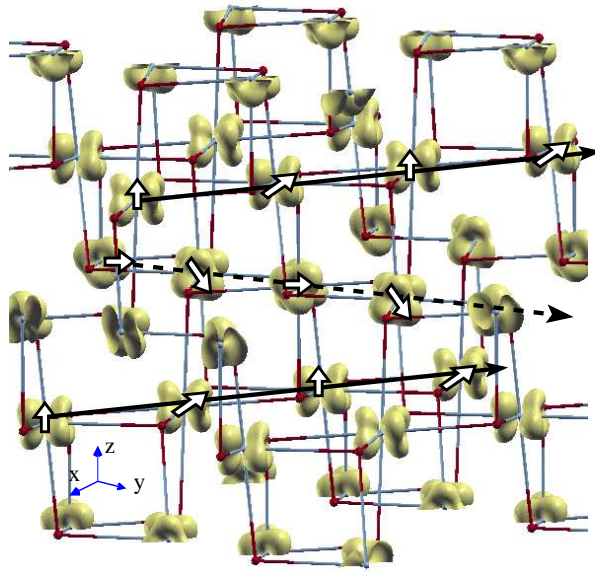


**Figure 3.5** Three-dimensional electron density plot showing the orbital ordering. The black solid and dashed lines designate the orbital chains. The arrows superimposed on the electron density at each V site mark the rotation sense of the orbitals as one moves to neighboring V sites within a given chain. The atoms at the alternate corners of the distorted cubes are occupied by V and O, respectively.

Fig. 3.5 shows the three-dimensional electron density of occupied V  $t_{2g}$  orbitals on a real space grid, in which a long range order pattern for the orbital distribution can be found. One can observe orbital chains along  $a$  and  $b$  directions (indicated by solid lines and dashed lines). It should be noted that the orbitals within each chain rotated alternatively by about  $45^\circ$ , which is shown by the arrow

marks. This is in contrary to the proposed staggered A-type ordering of orbitals. [2, 4] The staggered trigonal distortion that is present both within the  $ab$  plane and along the  $c$  direction is the root cause behind the rotation of orbitals with respect to each other within the chain and between the chains. We call the ordering *ferro-orbital* since it is in all sites the same orbital that is occupied by the second electron, and not an alternating occupation of  $xz$  and  $yz$ .

### 3.3.5 Effect of spin-orbit interaction

The spin-orbit coupling has been observed to play a significant role in dictating the nature of orbital order [8, 13] in similar type of vanadate spinel  $\text{ZnV}_2\text{O}_4$ . It has also been proposed to be important for the magnetic and orbital physics of  $\text{MnV}_2\text{O}_4$ [14]. We performed LSDA +  $U$  + SO calculations with the same  $U$  values as mentioned previously. The spin-orbit effects have been incorporated in our calculation as a second variation using the scalar relativistic approximation. Contrary to the case of  $\text{ZnV}_2\text{O}_4$  [8], we do not observe any significant difference in charge density from that of LSDA +  $U$ . It is well-known that the value of the orbital moment depends sensitively on the choice of  $U$ . It has already been mentioned in subsection 3.3.1, that the experimental V moment is best described for  $U = 4.5$  eV. At this  $U$  value we obtain an orbital moment of about  $0.34\mu_B$  at V site which is antiparallel to the spin moment ( $-1.65\mu_B$ ). This is in accordance with the Hunds rule, since V- $d$  orbitals are less than half filled. Theoretically calculated total magnetic moment and spin moment at Mn site are  $1.3\mu_B$  and  $4.24\mu_B$  respectively. These are in good agreement with the experimental estimate.[2] It should be noted that the perfect antiferro-orbital ordering as proposed earlier in literature would imply a quenching of orbital moment. The presence of a finite orbital moment can therefore be associated with the breakdown of perfect antiferro-orbital ordering.

### 3.3.6 Magnetic exchange interaction and non-collinear spin arrangement

The magnetic exchange couplings have been computed from first principles by considering LSDA +  $U$  total energy calculations. For this purpose we have considered different spin orientations of V ions within the V-only tetrahedra. The corresponding total energies have been mapped to a Heisenberg-like

model to estimate the magnetic exchange along the orbital chains ( $J$ ) and between the chains ( $J'$ ). The values obtained from our calculation are 11 meV and 2 meV respectively. This implies  $\alpha \approx J/J' = 0.2$  compared to 0.3 found by Chung *et al.* [7]. Perfect antiferro-orbital ordering with  $xz$  and  $yz$  alternately occupied along the orbital chain would, however, yield much smaller ratios of  $J/J'$ . This is because the overlap between orthogonal  $yz$  and  $xz$  orbitals at neighboring sites would have been nearly zero. Fig. 3.6 shows a schematic diagram of this situation. The moderately strong value of  $J'$ , as obtained in our calculation, originates from large mixing of different  $t_{2g}$  orbitals influencing the overlap of the re-normalized orbitals at neighboring sites.

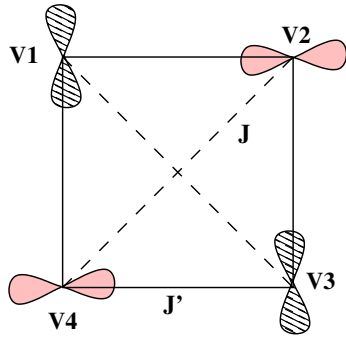


**Figure 3.6** Schematic diagram of projection of V tetrahedron on  $xy$  plane with  $xz$  and  $yz$  orbitals occupying alternate V site. The dashed lines represent V-V interaction along the chains ( $J$ ), whereas the solid lines represent the same between the chains ( $J'$ ). The solid filled and dash-line filled orbitals represent  $xz$  and  $yz$  orbitals respectively.

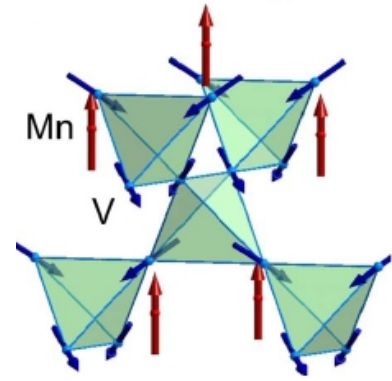


**Figure 3.7** Noncollinear spin arrangement of V spins on pyrochlore network of V only sub-lattice. The Blue color arrows indicate V spin which are rotated in about the  $c$ -axis direction. Mn spins (Brown arrows) remain collinear *ie.* along the  $c$ -axis direction. Figure is taken from Ref.[2].

All the calculations reported so far have been computed assuming collinear spin arrangement of V ions. Although experiment reports a transition from collinear to noncollinear spin arrangement coincident with the structural phase transition. Fig. 3.7 shows the noncollinear spin arrangement of V spins. We have carried out calculations to confirm whether our proposed orbital order sustains a noncollinear arrangement of V spins. We relaxed the V spin orientation keeping the Mn spins aligned

parallel to the  $c$  axis. The relaxed spin structure shows the V spins to be canted with respect to the  $c$  axis by about  $63^\circ$ , which is in very good agreement with the experimentally estimated canting of  $65^\circ$  reported by Garlea *et. al.*[2].

### 3.4 Conclusion

To investigate the nature of the orbital ordering in  $\text{MnV}_2\text{O}_4$ , DFT-based first principles calculations have been carried out. This orbital ordering is closely associated with the transition from a high temperature cubic structure to a low temperature tetragonal structure. Crystal structure optimization shows a strong influence of correlation effects in the choice of the correct low temperature structure. The ground state structure at low temperature is  $I4_1/a$ , which loses the mirror and glide symmetry compared to the alternative proposed candidate  $I4_1/amd$ . This lowering of symmetry necessarily breaks the degeneracy of the  $V-t_{2g}$  states completely and also introduces mixing between different  $t_{2g}$  states. The resulting eigen states therefore turn out to be of mixed character and non-degenerate, which get filled up by two V electrons. The corresponding orbital ordering at the V site represents a ferro-orbital ordering with formation of orbital chains in which the orbital rotates from one site to another both between and within the chain due to the presence of a co-operative type of local trigonal distortion at the V site. V-V magnetic exchange has been computed which are in good agreement with experimental results. Our computed results provide an explanation of the controversy between antiferro-orbital ordering versus the strong exchange between the orbital chains ( $J'$ ). Our proposed orbital ordering is capable of predicting correctly the noncollinear spin structure as observed experimentally [2]. There is a recent NMR study on single crystal of  $\text{MnV}_2\text{O}_4$  [15], which reports the orbital ordering at V sites to be consistent with the orbital ordering model proposed by us.

# Bibliography

- [1] P. G. Radaelli, *New Journal of Physics* **7**, 53 (2005).
- [2] V. O. Garlea, R. Jin, D. Mandrus, B. Roessli, Q. Huang, M. Miller, A. J. Schultz, and S. E. Nagler, *Phys. Rev. Lett.* **100**, 066404 (2008).
- [3] K. Adachi, T. Suzuki, K. Kato, K. Osaka, M. Takata, and T. Katsufuji, *Phys. Rev. Lett.* **95**, 197202 (2005).
- [4] T. Suzuki, M. Katsumura, K. Taniguchi, T. Arima, and T. Katsufuji, *Phys. Rev. Lett.* **98**, 127203 (2007).
- [5] P. J. Wojtowicz, *Phys. Rev.* **116**, 32–45 (1959).
- [6] R. Tackett, G. Lawes, B. C. Melot, M. Grossman, E. S. Toberer, and R. Seshadri, *Phys. Rev. B* **76**, 024409 (2007).
- [7] J.-H. Chung, J.-H. Kim, S.-H. Lee, T. J. Sato, T. Suzuki, M. Katsumura, and T. Katsufuji, *Phys. Rev. B* **77**, 054412 (2008).
- [8] T. Maitra and R. Valentí, *Phys. Rev. Lett.* **99**, 126401 (2007).
- [9] V. I. Anisimov, M. A. Korotin, M. Zöfl, T. Pruschke, K. Le Hur, and T. M. Rice, *Phys. Rev. Lett.* **83**, 364–367 (1999).
- [10] L. Pisani and R. Valentí, *Phys. Rev. B* **71**, 180409 (2005).

- 
- [11] C. J. Fennie and K. M. Rabe, *Phys. Rev. B* **72**, 214123 (2005).
- [12] O. K. Andersen and T. Saha-Dasgupta, *Phys. Rev. B* **62**, R16219–R16222 (2000).
- [13] O. Tchernyshyov, *Phys. Rev. Lett.* **93**, 157206 (2004).
- [14] R. Plumier and M. Sougi, *Physica B: Condensed Matter* **155**, 315 – 319 (1989).
- [15] S.-H. Baek, N. J. Curro, K.-Y. Choi, A. P. Reyes, P. L. Kuhns, H. D. Zhou, and C. R. Wiebe, *Phys. Rev. B* **80**, 140406 (2009).

## Chapter 4

# Coulomb enhanced spin-orbit coupling driven insulating phase in $\text{FeCr}_2\text{S}_4$ <sup>†</sup>

### 4.1 Introduction

$\text{FeCr}_2\text{S}_4$  is a known member of spinel family. Since '70s, it has regained interest due to the recent discovery of large negative magnetoresistance (MR)[1]. The MR effect has been discussed in the context of non-double exchange like model because of the absence of mixed valency and lack of any strong evidence of formation of Jahn-Teller (JT) polarons. The system is insulating above 180K and below 150K. At 180K temperature, there is magnetic transition in this compound with  $\text{Fe}^{2+}$  and  $\text{V}^{3+}$  ions coupled ferrimagnetically. This magnetic ordering persists even up to 50mK. Between the temperature range 180 K-150 K, metallic behaviour is shown by the compound [1, 2]. There have several experimental studies on this particular compound, but theoretical work reported is almost none except initial calculations [3] done by Park *et al.* We have carried out a detailed density functional theory study of the electronic structure of this material to understand the low temperature insulating phase.

---

<sup>†</sup>This chapter is based on *Phys. Rev. B 80, 201101(R) (2009)*

## 4.2 Motivation of the present work

A type and B type atom in this spinel compound,  $\text{FeCr}_2\text{S}_4$ , are Fe and V respectively. Therefore  $\text{Fe}^{2+}(d^6)$  and  $\text{V}^{3+}(d^3)$  ions are in tetrahedral and octahedral environment respectively. Since  $\text{Fe}^{2+}$  ion is in high spin state, in majority spin channel Fe- $d$  states are completely filled with one electron left in minority spin channel at degenerate Fe  $e$  levels. On the other hand,  $\text{V}^{3+}$  with three electrons completely occupies the  $t_{2g}$  states in majority spin channel with  $e_g$  states completely empty. Hence one should expect half-metallic solution for the ground state of  $\text{FeCr}_2\text{S}_4$ . This is in contradiction with the experimental report of insulating ground state of  $\text{FeCr}_2\text{S}_4$ .

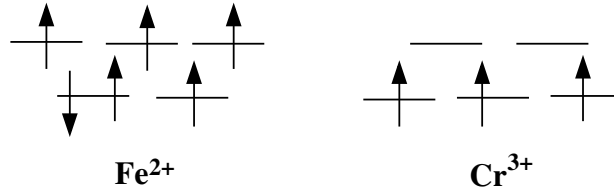


**Figure 4.1** Schematic diagram showing expected half-metallic ground state of  $\text{FeCr}_2\text{S}_4$ .  $\text{Cr}^{3+}$  with  $d^3$  configuration have  $t_{2g}$  states completely occupied and  $e_g$  states completely empty. On the contrary,  $\text{Fe}^{2+}$  with  $d^6$  configuration, have full-filled  $d$  levels in up-spin channel and a single electron in doubly degenerate  $e$  states in down spin channel, giving rise to a half-metallic ground state.

We have carried out first principles calculations to understand the counter intuitive low temperature ground state of  $\text{FeCr}_2\text{S}_4$ . In addition to this, there has been controversy regarding the low temperature structure of this compound. There are indications of some structural distortions at low temperature ( $\leq 60\text{K}$ )[4, 5]. Although the nature and existence of this distortion are debated. Reports from x-ray and neutron-diffraction studies [6] says that the sample remains in  $Fd\bar{3}m$  symmetry down to a temperature of 4.2 K. However, a recent transmission electron microscopic studies,[7] assigned a noncentrosymmetric  $F4\bar{3}m$  space group to the low-temperature structure. This structural aspect needs to be made clear for a better understanding of low temperature structure of  $\text{FeCr}_2\text{S}_4$ . There have been several experimental studies on this compound, including optical properties also. There have been reports of optical reflectivity and conductivity [8, 9, 10] measurements on this compound. We have computed

optical properties like reflectivity, from first principles calculations and compared with experimental data.

## 4.3 Results and Discussions

### 4.3.1 Crystal structure

Experimentally measured crystal structure of  $\text{FeCr}_2\text{S}_4$  shows cubic space group of symmetry  $Fd\bar{3}m$  with lattice parameter  $a = 9.99 \text{ \AA}$  and  $u_s = 0.384$ , [3, 6] where  $u_s$  is the internal parameter of S position in  $Fd\bar{3}m$  space group. The deviation of S position from the ideal value of 0.375 introduces trigonal distortion at  $\text{CrS}_6$  octahedra in terms of two distinct S-S bond lengths of 3.28 and 3.54  $\text{\AA}$ . The tetrahedral unit  $\text{FeS}_4$  in this space group however, remains ideal. The octahedral environment splits Cr- $d$  levels into usual low-lying  $t_{2g}$  and high lying  $e_g$  blocks, and there is some mixing between the two due to nonzero trigonal distortion present in  $\text{CrS}_6$  octahedra. In the next section we shall discuss this in detail in context of DOS calculation.

The calculations have been carried out within the frame work of LAPW basis set as implemented in WIEN2K code. The number of plane waves is restricted using the criteria muffin-tin radius multiplied by  $k_{max}$  yielding a value of 7. The total Brillouin zone (BZ) was sampled with 256 k points for self consistent calculations. The NMTO-downfolding calculation was used to determine the crystal field splitting at Fe and Cr sites. For this purpose, NMTO-downfolding calculations were carried out keeping only the Fe- $d$  and Cr- $d$  states active and downfolding all the other states, including S- $p$  states. The on-site block of the real-space Hamiltonian in the Fe- $d$  and Cr- $d$  basis gives the crystal field splitting.

### 4.3.2 Density of states and energy level splitting within GGA

$\text{Cr}^{3+}(d^3)$  has completely filled  $t_{2g}$  states in up spin channel and all the  $d$  states empty in down spin channel, which can be seen in Fig. (4.2). The Fe  $d$  levels are completely occupied in down spin channel with partially filled  $e$  block in up-spin channel. This confirms the nominal 3+ and 2+ valency of Cr and Fe, respectively. Calculation within GGA results in a half-metallic ground state, which is in contra-

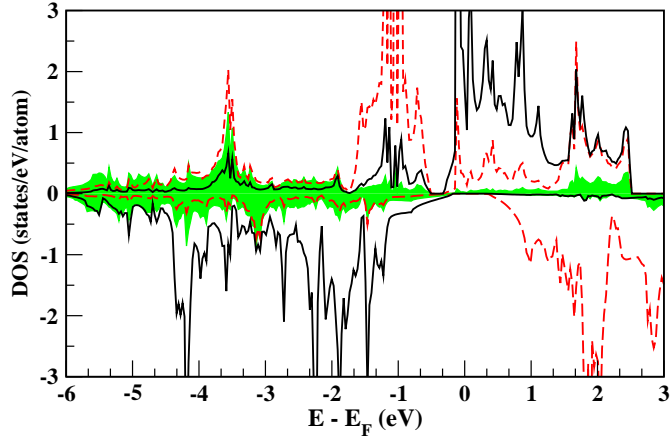


**Figure 4.2** spin-polarized partial density of states calculated within GGA. Fe- $d$  states, Cr- $d$  states, and S- $p$  states are presented by solid black lines, broken gray lines and filled light gray areas, respectively. Energy is plotted with respect to Fermi energy ( $E_f$ ).

diction with the experimental reports, as discussed at the beginning of this chapter. The superexchange interaction between half-filled Cr  $t_{2g}$  states and half-filled Fe  $d$  states gives rise to antiferromagnetic coupling between Cr and Fe. On the other hand, ferromagnetic coupling between Cr and Fe can result due to the superexchange interaction between empty Cr  $e_g$  states and partially filled Fe levels. The former becomes dominant which results into net antiferromagnetic coupling between Cr and Fe with magnetic moments at Cr and Fe sites  $2.75$  and  $-3.14 \mu_B$ , respectively, with a total magnetic moment of  $2 \mu_B/f.u.$

In order to evaluate the crystal field splitting at Fe and Cr site, we have carried out NMTO down-folding calculations. In this calculation we have downfolded all the states except Fe- $d$  and Cr- $d$ . The crystal-field splitting at the Fe site is found to be smaller than the spin splitting, while at the Cr site they are found to be comparable. Energetically Cr  $e_g$  up-spin states are close to Fe  $d$  states in the up-spin channel. This causes significant hybridization between empty Cr  $e_g$  and Fe  $d$  states in the up-spin channel.

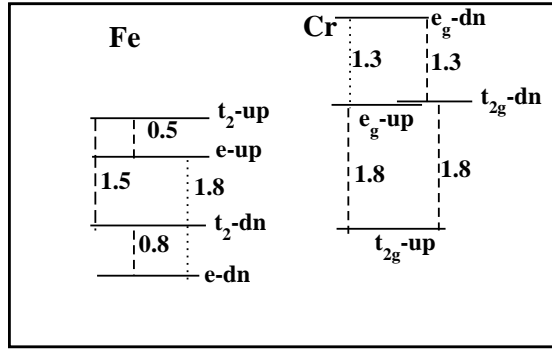


**Figure 4.3** The energy levels of Fe and Cr  $d$  levels in eV unit, calculated using NMTO downfolding technique.

### 4.3.3 Band structure beyond GGA

In order to have the desired insulating ground state, both, missing correlation effect [3] as well as the Jahn-Teller (JT) effect,[4] have been discussed in literature to account for this discrepancy. Regarding the JT effect, it should be noted that the relevant JT ion  $\text{Fe}^{2+}$  is in tetrahedral environment with Fe  $e$  states being the relevant degree of freedom. The JT distortion within the  $e$  manifold which point in between the S ions is expected to be weak. There are indications of some structural distortions of  $\text{FeCr}_2\text{S}_4$  at temperature below 60 K [4, 5], although the nature and existence of this distortion are debated. The x-ray and neutron-diffraction experiments [6] reports that the sample remains in  $Fd\bar{3}m$  symmetry, down to a temperature 4.2 K. A recent transmission electron microscopic studies,[7] reports that the low temperature structure to be in  $F\bar{4}3m$  symmetry. Lowering symmetry from  $Fd\bar{3}m$  to  $F\bar{4}3m$  would give rise to two inequivalent Fe ions in the unit cell, it can not to lift the degeneracy within the  $e$  block avoiding the JT distortion. We shall discuss this point in detail later.

Leaving aside the possible influence of structural distortion, band dispersion of  $\text{FeCr}_2\text{S}_4$  in  $Fd\bar{3}m$  symmetry along the high-symmetry points of the BZ of the cubic-face centered (FCC) lattice in the up-spin channel is studied (see Fig. 4.4). We considered only the up spin channel because in down spin either all states are completely filled or completely empty. From left to right, the various panels show the results obtained on the basis of GGA, GGA+ $U$ , GGA+SO, and GGA+ $U$ +SO calculations. The band

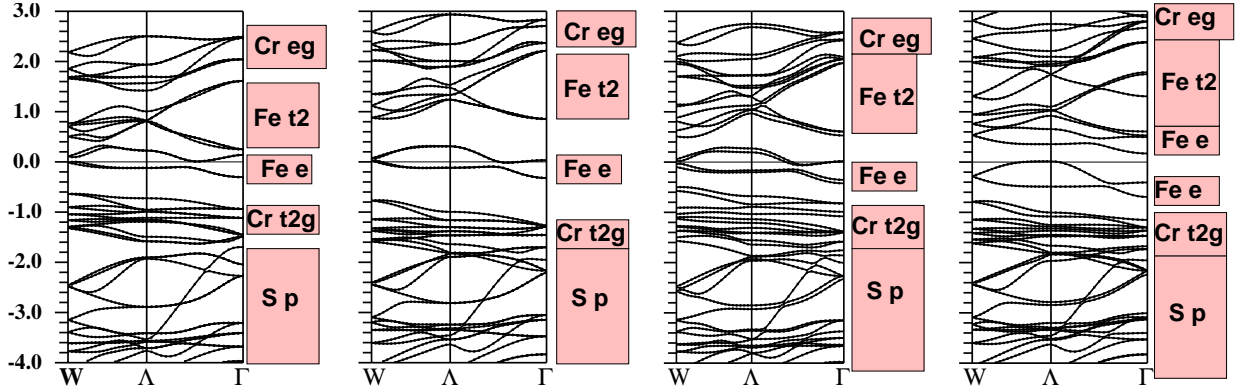


**Figure 4.4** Band structure of  $\text{FeCr}_2\text{S}_4$  in the up-spin channel. Energies are plotted with respect to  $E_F$  in eV unit. From left to right: band structures calculated with GGA, GGA+ $U$ , GGA+SO, and GGA+ $U$ +SO, respectively. In the GGA+ $U$ , and GGA+ $U$ +SO calculations, the  $U$  values were chosen as  $U_{Fe}=2.50$  eV,  $U_{Cr}=1.50$  eV, and  $J_{Fe}=0.9$  eV,  $J_{Cr}=0.8$  eV.

dispersion calculated within GGA, corresponds to the DOS shown in Fig. 4.2. It shows that degenerate  $Fe\ e$  bands of  $3y^2 - r^2$  and  $z^2 - x^2$  cross  $E_f$  making the system half-metallic.

The band structure taking into account the missing correlation in GGA calculation, incorporated within GGA+ $U$  formalism is shown in next panel of Fig. 4.4. The GGA+ $U$  method is designed to make the configurations with larger magnetization more favorable. Here in a manifold of degenerate bands involving only one spin channel, the method is therefore not effective, although the double counting scheme still remains operative. Our study reveals that the application of onsite  $U$  increases the gap between  $e$  and  $t_2$  blocks of  $Fe\ d$  states compared to that obtained from GGA calculations. We have also found that with increasing value of  $U$  this gap also increases, keeping the structure of degenerate  $e$  bands crossing the Fermi level intact. Therefore it can be concluded that the inclusion of on-site Hubbard  $U$  is not capable of driving the insulating solution, unless the symmetry is broken by some means.

The third panel of Fig. 4.4 shows the result of inclusion of spin-orbit coupling (SOC). Our calculation shows that spin and orbital moments have the same sign for  $Fe$ , but opposite sign for  $Cr$ . This is in

accordance of Hund's rule, since the  $d$  states of  $\text{Fe}^{2+}$  are more than half filled, but those of  $\text{Cr}^{3+}$  are less than half filled (see Table 4.1). The orbital moment at the Cr site is found to be small due to the  $d^3$  configuration of Cr. On the other hand, the orbital moment at Fe site is found to be large which is bit surprising. The two degenerate  $e$  states of Fe comprising of states which differ by  $\Delta l_z = 0, \pm 2$ , therefore orbital moment should vanish. However this finite orbital moment at Fe site can happen through coupling with empty Fe  $t_2$  states. In order to understand the role of SOC in the Fe  $d$  manifold, let us consider the following Hamiltonian. The spin-orbit part of the Hamiltonian is given by,

$$\begin{aligned} \hat{H}_{SO} = \lambda [ & \hat{S}_z (\hat{L}_z \cos \theta + \frac{1}{2} \hat{L}_+ e^{-i\phi} \sin \theta + \frac{1}{2} \hat{L}_- e^{i\phi} \sin \theta) \\ & + \frac{1}{2} \hat{S}_+ (-\hat{L}_z \sin \theta - \hat{L}_+ e^{-i\phi} \sin^2 \frac{\theta}{2} + \hat{L}_- e^{i\phi} \cos^2 \frac{\theta}{2}) \\ & + \frac{1}{2} \hat{S}_- (-\hat{L}_z \sin \theta - \hat{L}_+ e^{-i\phi} \cos^2 \frac{\theta}{2} + \hat{L}_- e^{i\phi} \sin^2 \frac{\theta}{2}) ] \quad (4.1) \end{aligned}$$

In the Eq. (4.1)  $\theta$  and  $\phi$  are the zenith and azimuthal angles of the magnetization direction of the spin moment. Calculation within GGA shows that the up and down spin states are energetically separated by 1.5-2 eV. Therefore it is expected that these states would not couple through SOC. Hence the parts of the spin-orbit Hamiltonian with spin raising and lowering operator (last two parts of the Eq.(4.1)) have been neglected and the effective Hamiltonian studied is given as,

$$\hat{H}_{SO} = \lambda [\hat{S}_z (\hat{L}_z \cos \theta + \frac{1}{2} \hat{L}_+ e^{-i\phi} \sin \theta + \frac{1}{2} \hat{L}_- e^{i\phi} \sin \theta)] \quad (4.2)$$

The angular parts of the  $d$  orbitals have been expressed in terms of spherical harmonics. Our calculation shows that SOC introduces coupling between empty Fe  $|xz\rangle, |yz\rangle$  states and  $|z^2 - x^2\rangle, |3y^2 - r^2\rangle$  states. The coupling  $\langle yz | \hat{H}_{SO} | z^2 - x^2 \rangle$  is  $\propto \sin \theta \cos \phi$ ,  $\langle xz | \hat{H}_{SO} | z^2 - x^2 \rangle$  is  $\propto \sin \theta \sin \phi$  and similar dependencies are found for the coupling with  $|3y^2 - r^2\rangle$  state. Keeping this in view, the matrix form of Hamiltonian, given in Eq. (4.2), takes the following form.

	$ z^2 - x^2\rangle$	$ 3y^2 - r^2\rangle$	$ yz\rangle$	$ zx\rangle$	$ xy\rangle$
$\langle z^2 - x^2  $	$\epsilon_2$	0	$i \frac{1-\sqrt{3}}{2} \sin\theta \cos\phi$	$i \frac{1-\sqrt{3}}{2} \sin\theta \sin\phi$	0
$\langle 3y^2 - r^2  $	0	$\epsilon_2$	$i \frac{\sqrt{3}(1+\sqrt{3})}{2} \sin\theta \cos\phi$	$i \frac{\sqrt{3}(\sqrt{3}-1)}{2} \sin\theta \sin\phi$	0
$\langle yz  $	$i \frac{(\sqrt{3}-1)}{2} \sin\theta \cos\phi$	$-i \frac{\sqrt{3}(\sqrt{3}+1)}{2} \sin\theta \cos\phi$	$\epsilon_1$	$i \cos\theta$	$-i \sin\theta \sin\phi$
$\langle zx  $	$i \frac{(\sqrt{3}-1)}{2} \sin\theta \sin\phi$	$i \frac{\sqrt{3}(\sqrt{3}-1)}{2} \sin\theta \sin\phi$	$-i \cos\theta$	$\epsilon_1$	$i \sin\theta \cos\phi$
$\langle xy  $	0	0	$i \sin\theta \sin\phi$	$-i \sin\theta \cos\phi$	$\epsilon_1$

where,  $\varepsilon_1$  and  $\varepsilon_2$  are the energies of Fe  $t_2$  and  $e$  states respectively. Starting from  $5 \times 5$  Hamiltonian we carried out downfolding technique to get the Fe-Fe on-site Hamiltonian in  $z^2 - x^2$  and  $3y^2 - r^2$  basis set. In section 2.2.2 of chapter 2, we have mentioned about how downfolding technique works. In this technique, the space of a basis set is considered to be subdivided into two subsets, lower  $|l\rangle$  and  $|h\rangle$ . The reduction of the full Hamiltonian  $H$  into the lower subset Hamiltonian  $\tilde{H}_{ll}$  is carried out in such a manner that lower  $l$  eigenvalues of  $H$  and eigenvalues of  $\tilde{H}_{ll}$  are same. The formation of  $\tilde{H}_{ll}$  introduces additional energy dependence through the expression

$$\tilde{H}_{ll} = H_{ll} - H_{lh} \frac{1}{(H_{hh} - \varepsilon)} H_{hl} \quad (4.3)$$

In the present example let us first downfold the  $|xy\rangle$  state. Hence to be consistent with Eq. (4.3), now  $H_{hh} = \varepsilon_1$ ,  $\varepsilon$  is chosen as Fermi energy and  $H_{lh}, H_{hl}, H_{ll}$  take the following form,

$$H_{hl} = \begin{bmatrix} 0 & 0 & i \sin\theta \sin\phi & -i \sin\theta \cos\phi \end{bmatrix} \quad H_{lh} = \begin{bmatrix} 0 \\ 0 \\ -i \sin\theta \sin\phi \\ i \sin\theta \cos\phi \end{bmatrix}$$

$$H_{ll} = \begin{bmatrix} \varepsilon_2 & 0 & i \frac{1-\sqrt{3}}{2} \sin\theta \cos\phi & i \frac{1-\sqrt{3}}{2} \sin\theta \sin\phi \\ 0 & \varepsilon_2 & i \frac{\sqrt{3}(1+\sqrt{3})}{2} \sin\theta \cos\phi & i \frac{\sqrt{3}(\sqrt{3}-1)}{2} \sin\theta \sin\phi \\ i \frac{(\sqrt{3}-1)}{2} \sin\theta \cos\phi & -i \frac{\sqrt{3}(\sqrt{3}+1)}{2} \sin\theta \cos\phi & \varepsilon_1 & i \cos\theta \\ i \frac{(\sqrt{3}-1)}{2} \sin\theta \sin\phi & i \frac{\sqrt{3}(\sqrt{3}-1)}{2} \sin\theta \sin\phi & -i \cos\theta & \varepsilon_1 \end{bmatrix}$$

Now using Eq. 4.3 one can evaluate  $\tilde{H}_{ll}$ , which in this case is the downfolded form of  $5 \times 5$  Hamiltonian in  $|z^2 - x^2\rangle, |3y^2 - r^2\rangle, |yz\rangle, |zx\rangle$  basis. After downfolding the  $xy$  state, the Hamiltonian

takes the following form,

$$\tilde{H}_{II} = \begin{bmatrix} \varepsilon_2 & 0 & i\frac{(1-\sqrt{3})}{2}\sin\theta\cos\phi & i\frac{(1-\sqrt{3})}{2}\sin\theta\sin\phi \\ 0 & \varepsilon_2 & i\frac{\sqrt{3}(1+\sqrt{3})}{2}\sin\theta\cos\phi & i\frac{\sqrt{3}(\sqrt{3}-1)}{2}\sin\theta\sin\phi \\ -i\frac{(1-\sqrt{3})}{2}\sin\theta\cos\phi & -i\frac{\sqrt{3}(1+\sqrt{3})}{2}\sin\theta\cos\phi & \varepsilon_1 + \frac{\sin^2\theta\sin^2\phi}{\varepsilon_F - \varepsilon_1} & \frac{\sin^2\theta\sin^2\phi}{2(\varepsilon_F - \varepsilon_1)} + i\cos\theta \\ -i\frac{(1-\sqrt{3})}{2}\sin\theta\sin\phi & -i\frac{\sqrt{3}(\sqrt{3}-1)}{2}\sin\theta\sin\phi & \frac{\sin^2\theta\sin^2\phi}{2(\varepsilon_F - \varepsilon_1)} - i\cos\theta & \varepsilon_1 + \frac{\sin^2\theta\cos^2\phi}{\varepsilon_F - \varepsilon_1} \end{bmatrix}$$

Repeating the same procedure to downfold the  $yz$  and  $zx$  state, one can get the Fe-Fe on-site Hamiltonian in  $z^2 - x^2$  and  $3y^2 - r^2$  basis set. To simplify the expressions let us consider  $\phi = \frac{\pi}{2}$  and  $\theta$  as variable. The downfolded  $2 \times 2$  Hamiltonian takes the following form:

$$H = \begin{pmatrix} \varepsilon_2 + \tilde{\varepsilon}(\theta) & -\sqrt{3}\tilde{\varepsilon}(\theta) \\ -\sqrt{3}\tilde{\varepsilon}(\theta) & \varepsilon_2 + 3\tilde{\varepsilon}(\theta) \end{pmatrix} \quad (4.4)$$

where

$$\tilde{\varepsilon}(\theta) = \frac{\left(\frac{\sqrt{3}-1}{2}\sin\theta\right)^2}{\varepsilon_F - \varepsilon_1 - \frac{\cos^2\theta}{\varepsilon_F - \varepsilon_1 - \frac{\sin^2\theta}{\varepsilon_F - \varepsilon_1}}}$$

The difference between eigen values of the Hamiltonian gives the splitting between the two  $e$  states. For this particular example, the splitting comes out to be  $4\tilde{\varepsilon}(\theta)$ . Therefore it can be noted that the splitting between Fe  $z^2 - x^2$  and  $3y^2 - r^2$  states does depend on the Fe  $t_2$  states.

Our study reflects to the fact that the SOC-induced splitting between Fe  $z^2 - x^2$  and  $3y^2 - r^2$  are strongest for  $\theta = \frac{\pi}{2}$ . In other words, the above mentioned splitting are strongest when the spin quantization axis is in the  $xy$  plane. We considered the onsite energies of Fe  $d$  orbitals as shown in the Fig. 4.3, and considered a typical value of spin-orbit coupling parameter  $\lambda = -0.02$  eV. For a fixed value of  $\theta = \frac{\pi}{2}$ , the splitting between Fe  $3y^2 - r^2$  and  $z^2 - x^2$  states as a function of  $\phi$  has been evaluated and is shown in Fig. 4.5. From this figure it is clear that the splitting between those two Fe  $e$  states is strongest for  $\phi = 0$ .

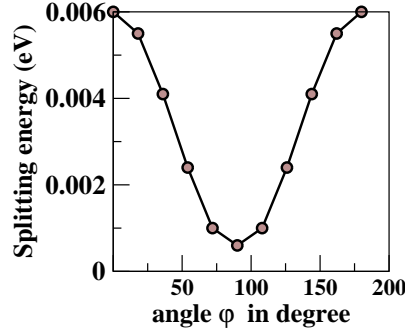


**Figure 4.5** Splitting between Fe  $z^2 - x^2$  and  $3y^2 - r^2$  levels in eV plotted as function of  $\phi$

	Fe		Cr	
	Orbital moment	Spin moment	Orbital moment	Spin moment
GGA	...	-3.135	...	2.750
GGA+U	...	-3.279	...	2.720
GGA+SO	-0.077	-3.133	-0.024	2.754
GGA+U+SO	-0.134	-3.270	-0.026	2.690

**Table 4.1** Magnetic moments of Fe and Cr ions in  $\mu_B$ .

#### Effect of SOC in presence of Coulomb $U$

The splitting introduced between Fe  $e$  states due to SOC, however is not enough to make the system insulating. The situation changes remarkably upon application of GGA+U+SO, as is shown in the right most panel of Fig. 4.4. The SOC in presence of Coulomb  $U$ , introduces enough splitting between Fe  $z^2 - x^2$  and  $3y^2 - r^2$  states so that the system becomes insulator. This kind of Coulomb enhanced spin-orbit splitting as has been already seen for  $\text{Sr}_2\text{RhO}_4$ [11] and for double perovskite  $\text{Ba}_2\text{NaOsO}_6$ [12]. Choice of  $U$  and  $J$  value for Fe and Cr ions in this particular calculation is furnished below.

$$U_{Fe}=2.50 \text{ eV}, U_{Cr}=1.50 \text{ eV}, J_{Fe}=0.9 \text{ eV}, \text{ and } J_{Cr}=0.8 \text{ eV}$$

The SOC enhanced by Coulomb correlation opens up a gap of 0.1 eV with  $z^2 - x^2$  completely occupied

and  $3y^2 - r^2$  being completely empty. With the increase of  $U$  value at Fe site, the gap value increases because of the fact that double-counting correction pushes the empty local states further apart, although the orbital moment at Fe saturated. The variation in the band gap and Fe orbital moment as a function of  $U$  is shown in Fig. 4.6.

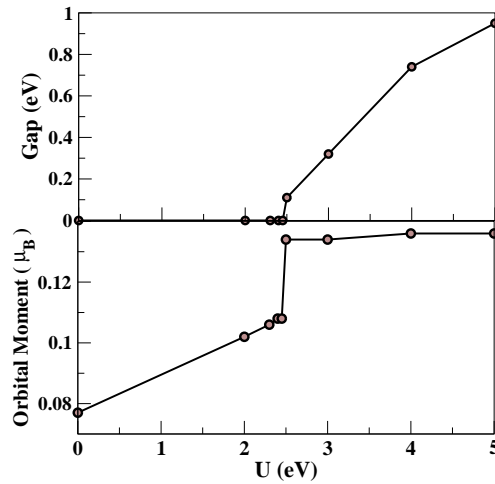


**Figure 4.6** Variation of Fe orbital moment (upper panel) and band gap (lower panel) as a function  $U$  applied at Fe site.

The magnetocrystalline anisotropy energy has also been computed for this compound, which turns out to be 10 meV/Fe. This anisotropy energy is the energy difference between calculations with the spin quantization along [001] and [110], however the system favors the spin quantization axis to be along [110]. The spin quantization is found to be further favored along [100] by 20 meV/Fe compared to [110], which is consistent with our findings from Fe  $t_2$  mediated SOC.

#### 4.3.4 Possible structural distortion at low temperature

As discussed in subsection 4.3.3, there is possibility of S and Cr movements in the low-temperature crystal structure of  $\text{FeCr}_2\text{S}_4$ [7]. As a next step of our study we have investigated the possible structural transition from  $Fd\bar{3}m$  to  $F\bar{4}3m$  by total energy calculations. There have reports of similar controversy regarding the space group of another spinel compound  $\text{MgAl}_2\text{O}_4$ . In case of  $\text{MgAl}_2\text{O}_4$  also, it is

debated which is the correct symmetry,  $Fd\bar{3}m$  or  $F\bar{4}3m$ [13, 14]. We follow the scheme adopted by Staszak *et. al.* for determination of ion positions of  $MgAl_2O_4$  in  $F\bar{4}3m$ , to carry out calculations for checking which one is the favorable symmetry of  $FeCr_2S_4$ ,  $Fd\bar{3}m$  or  $F\bar{4}3m$ . The ion positions of cubic spinel compound in  $F\bar{4}3m$  space group is given in Table 4.2.

Ion	Position
Fe	0.0, 0.0, 0.0
Fe	0.25, 0.25, 0.25
Cr	$0.625 + \delta_3, 0.625 + \delta_3, 0.625 + \delta_3$
O	$0.375 + \delta_1, 0.375 + \delta_1, 0.375 + \delta_1$
O	$0.875 - \delta_2, 0.875 - \delta_2, 0.875 - \delta_2$

**Table 4.2** Position of ions of  $FeCr_2S_4$  in  $F\bar{4}3m$  space group

From the Table 4.2 it is clear that within  $F\bar{4}3m$  space group there are two inequivalent Fe and S ions and one inequivalent Cr ion. If  $\delta_1$  and  $\delta_2$  becomes equal and  $\delta_3$  becomes zero then the ion positions of  $F\bar{4}3m$  space group actually corresponds to that of  $Fd\bar{3}m$  (see Table 4.2)[13].  $\delta_1$  and  $\delta_2$  governs the distortion related to the movement of S ions, where as  $\delta_3$  is associated with movement of Cr ions. We carried out total-energy calculations within the framework of GGA+ $U$ +SO with same choice of  $U$ ,  $J$  values as discussed earlier, assuming  $F\bar{4}3m$  symmetry. We have considered different sets of values of  $(\delta_1, \delta_2)$ , and for each set  $\delta_3$  is varied over a range of -0.002 to 0.002.

The total-energy curve as shown in Fig. 4.7 shows a tendency of small Cr movement as well as some movements of S ions in the low temperature structure of  $FeCr_2S_4$ . It is interesting to note that the small movements in S ions produce two different class of  $FeS_4$  tetrahedra of different volumes. This S movement dose not introduces any distortion in the  $FeS_4$  tetrahedra, those tetrahedra remain uniform. Therefore even in the  $FeCr_2S_4$  structure with both Cr and S ion displacement, the Fe  $t_2$  states remain degenerate. We repeated electronic structure calculations with ionic positions as given in  $F\bar{4}3m$  crystal structure. Our study reveals that S movements tend to reduce the band gap, while the Cr movement

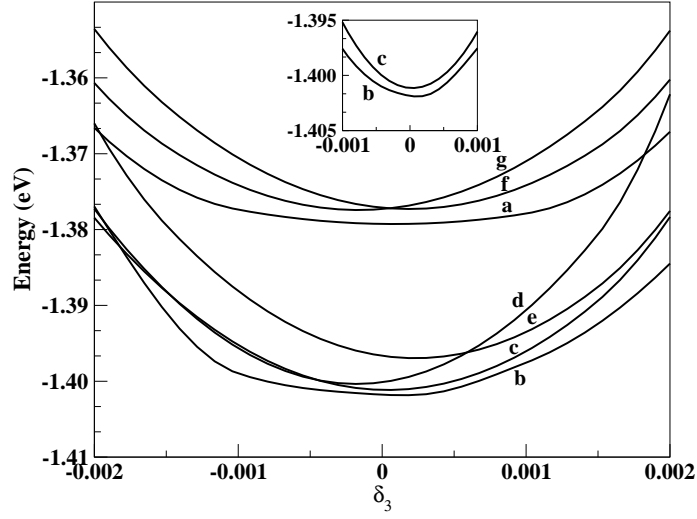


**Figure 4.7** A series of minimum-energy curves plotted against the variation of Cr position  $\delta_3$ , for various choices of S movements: (a)  $\delta_1 = \delta_2 = 0.0090$ ; (b)  $\delta_1 = 0.0095, \delta_2 = 0.0085$ ; (c)  $\delta_1 = 0.0085, \delta_2 = 0.0095$ ; (d)  $\delta_1 = 0.0085, \delta_2 = 0.0100$ ; (e)  $\delta_1 = 0.0100, \delta_2 = 0.0085$ ; (f)  $\delta_1 = 0.0090, \delta_2 = 0.0095$ ; (g)  $\delta_1 = 0.0095, \delta_2 = 0.0090$ . The inset shows the two lower most curves. For the lowest curve (b) the minimum energy position corresponds to non-zero value of  $\delta_3$ .

tends to increase it. The optimized values of S and Cr movements, given by curve “b”, gave rise to a gap of 0.2 eV.

#### 4.3.5 Computed optical conductivity and reflectivity

There have been reports of optical reflectivity and conductivity [8, 9, 10] measurements on this particular sulphide spinel. It is therefore worthwhile to compute the optical properties from first-principles calculations and compare with the experimental results. In doing so, the reflectivity spectrum was calculated using the joint density of states and the dipole matrix elements .

Joint density of states (JDOS) provides the optical conductivity in arbitrary units if one can ignore the transition rules. It is given by

$$JDOS(\omega) = \frac{4\pi^2 e^2}{\Omega m^2 \omega^2} \sum_{k m' \zeta} \delta(\epsilon_{k m'} - \epsilon_{k n} - \hbar \omega)$$

where  $e$  and  $m$  are the charge and mass of the electron,  $\Omega$  is the volume of the unit cell,  $\omega$  is the photon frequency, and  $\epsilon_{kn'}$  and  $\epsilon_{kn}$  are the eigenvalues of conduction (final) and valence (initial) bands at  $k$  point in the Brillouin zone for  $\zeta$  spin channel. Realistic comparison of theoretically calculated optical properties with experimental optical spectrum is only possible when the actual transition probabilities or the dipole matrix elements are convoluted with JDOS. Band structure calculations provide only the dispersive and the absorptive parts of the diagonal and off-diagonal conductivities, respectively, using the selection rules. The corresponding imaginary or real counterparts are obtained by using the Kramers-Kronig transformation. The expressions for the diagonal conductivity and off-diagonal conductivity are given by,

$$\sigma_{ij}(\omega) = \frac{4\pi^2 e^2}{\Omega m^2 \omega} \sum_{kn'\zeta} (\langle kn\zeta | p_i | kn'\zeta \rangle \langle kn'\zeta | p_j | kn\zeta \rangle) \times \delta(\epsilon_{kn'} - \epsilon_{kn} - \hbar\omega)$$

where  $\langle kn\zeta | p_i | kn'\zeta \rangle$  is the dipole matrix element evaluated in the basis of the Kohn-Sham orbitals. It gives the transition probability from state  $n$  to state  $n'$  at  $k^{th}$  point in BZ in the  $\zeta$  spin channel, with  $p_i$  being the momentum operator in the  $i$  direction. Dielectric function ( $\xi_{ij}$ ) is given as

$$\xi_{ij}(\omega) = \delta_{ij} + i \frac{4\pi}{\omega} \sigma_{ij}(\omega)$$

. In turn the reflectivity can be expressed as

$$R(\omega) = \left| \frac{\sqrt{\xi_{xx}(\omega)} - 1}{\sqrt{\xi_{xx}(\omega)} + 1} \right|^2$$

It should be noted that though the experimental spectra were measured at room temperature, such a comparison is found to be reasonable. None of the optical experiments reported till date show any substantial modification of the optical spectrum in the energy region explored as temperature is changed,[10] which indicates that the gross electronic structure remains unaltered by the temperature variation. The experimental spectrum shown as dotted line in Fig. 4.8 shows a peaked structure (structure I) at about 0.3 eV and a broad one (structure II) between 0.7 and 7.0 eV. In between these two structures there is a dip at about 0.5 eV. The reflectivity data calculated is calculated within GGA+ $U$ +SO, as shown in the previously mentioned figure by solid line. In general there is a good agreement between our calculated reflectivity data and experimental data. The broad shape and position of structure II,

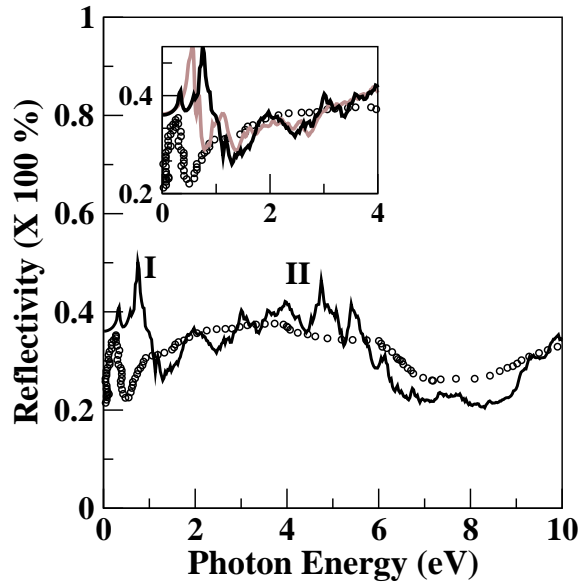


**Figure 4.8** Comparison of calculated reflectivity spectrum (solid line) and experimentally measured spectrum (dotted line). Two calculated spectra in the inset, shown as black and grey solid lines, correspond to calculations in undistorted and distorted crystal structure, respectively.

which originates from the transitions involving fully occupied Cr  $t_{2g}$  and S  $p$  states in the valence band, and the empty Fe  $d$  and Cr  $e_g$  and S  $p$  hybridized states in the majority-spin channel and the fully filled Fe  $d$  hybridized with S  $p$  states to the empty Cr  $d$  states in the minority-spin channels, agrees very well with the experimental one. On the other hand the peak at structure I is much broader in the calculation. Regarding this point an important issue to consider is the influence of the structural distortion. The inset of fig. 4.8, shows the change in the reflectivity caused by the movements of Cr and S ions (spectrum shown in solid gray line). It is found to alter structure I while keeping all the structures beyond 1.2 eV unaltered. Structure I narrows down and moves down in energy and the following dip moves down, thereby providing a better agreement in the low energy feature. The precise determination of the ionic positions therefore seems crucial.

## 4.4 Conclusion

In this chapter we have shown how first principles calculations have been employed to study the origin of insulating ground state of  $\text{FeCr}_2\text{S}_4$  in low temperature regime. Our study reveals that the insulating behaviour is driven by spin-orbit coupling within Fe  $e$  states which gets renormalized in presence of Coulomb correlation. This adds  $\text{FeCr}_2\text{S}_4$  to the list of compounds exhibiting Coulomb enhanced spin-orbit coupling. The large spin-orbit coupling found within Fe  $e$  states are quite unusual and we have found that this happens due to coupling with empty Fe  $t_2$  states. The possible role of low-temperature structural distortion of this sulphide spinel has been explored. Our total-energy calculation shows tendency of both S and Cr movements in the low temperature phase of  $\text{FeCr}_2\text{S}_4$ . Comparison of calculated reflectivity spectrum with experimentally measured data shows improved agreement in the mid infra-red regime upon inclusion of structural distortion. More experimental studies are needed for a complete understanding of the optical properties.

# Bibliography

- [1] A. P. Ramirez, R. J. Cava, and J. Krajewski, *Nature* **386**, 156–159 (1997).
- [2] Z. Chen, S. Tan, Z. Yang, and Y. Zhang, *Phys. Rev. B* **59**, 11172–11174 (1999).
- [3] M. S. Park, S. K. Kwon, S. J. Youn, and B. I. Min, *Phys. Rev. B* **59**, 10018–10024 (1999).
- [4] M. Spender and A. Morrish, *Solid State Communications* **11**, 1417 – 1421 (1972).
- [5] M. Eibschutz, S. Shtrikman, and Y. Tenenbaum, *Physics Letters A* **24**, 563 – 564 (1967).
- [6] G. Shirane, D. E. Cox, and S. J. Pickart, *Journal of Applied Physics* **35**, 954–955 (1964).
- [7] M. Mertinat, V. Tsurkan, D. Samusi, R. Tidecks, and F. Haider, *Phys. Rev. B* **71**, 100408 (2005).
- [8] T. Ogasawara, K. Ohgushi, H. Okamoto, and Y. Tokura, *Journal of the Physical Society of Japan* **75**, 083707 (2006).
- [9] K. Ohgushi, Y. Okimoto, T. Ogasawara, S. Miyasaka, and Y. Tokura, *Journal of the Physical Society of Japan* **77**, 034713 (2008).
- [10] K. Ohgushi, T. Ogasawara, Y. Okimoto, S. Miyasaka, and Y. Tokura, *Phys. Rev. B* **72**, 155114 (2005).
- [11] G.-Q. Liu, V. N. Antonov, O. Jepsen, and O. K. Andersen., *Phys. Rev. Lett.* **101**, 026408 (2008).
- [12] H. J. Xiang and M.-H. Whangbo, *Phys. Rev. B* **75**, 052407 (2007).

- [13] P. R. Staszak, J. E. Poetzinger, and G. P. Wirtz, *Journal of Physics C: Solid State Physics* **17**, 4751 (1984).
- [14] K. D. Rouse, M. W. Thomas, and B. T. M. Willis, *Journal of Physics C: Solid State Physics* **9**, L231 (1976).

## Chapter 5

# Comparative study of two similar spinels : $\text{FeCr}_2\text{S}_4$ and $\text{FeSc}_2\text{S}_4$ <sup>†</sup>

### 5.1 Introduction

In the previous chapter we have discussed about  $\text{FeCr}_2\text{S}_4$  in which the orbitally active ion is A-site ion  $\text{Fe}^{2+}$ . In the present chapter we shall consider another spinel compound in which like  $\text{FeCr}_2\text{S}_4$ , A-site ion is also  $\text{Fe}^{2+}$ . Except for the difference in B-site ion, formula of these two spinel compounds are exactly same. In  $\text{FeCr}_2\text{S}_4$  the B site ion is  $\text{Cr}^{3+}$  which is magnetic with local  $S=3/2$  moment, while in  $\text{FeSc}_2\text{S}_4$  compound the B site is occupied by  $\text{Sc}^{3+}$  which has filled shell [Ar] configuration. The A site ion,  $\text{Fe}^{2+}(d^7)$  in both the compounds, has one hole in the doubly degenerate  $e$  levels of the tetrahedrally split  $fe$   $d$  levels, giving rise to orbital degeneracy.

### 5.2 Motivation of the present work

Although the chemical formula of the two spinel compounds  $\text{FeCr}_2\text{S}_4$  and  $\text{FeSc}_2\text{S}_4$  are exactly the same except for B-site ion, these compounds behave very differently. The Cr-compound orders mag-

---

<sup>†</sup>This chapter is based on *Phys. Rev. B* 82, 041105(R) (2010)

netically in a ferrimagnetic spin arrangement between Fe and Cr moments with a transition temperature of 167 K[1] while  $\text{FeSc}_2\text{S}_4$  does not order magnetically even up to a measured temperature of 50 mK[2]. Experiments with poly-crystalline samples of  $\text{FeCr}_2\text{S}_4$  reports long-range orbital ordering while a glassy freezing phase has been observed in single crystals of the same compound. In contrast to this,  $\text{FeSc}_2\text{S}_4$  has been reported as an orbital liquid[3]. The Curie-Weiss temperature ( $\Theta_{CW}$ ), obtained by fitting the high temperature behaviour of magnetic susceptibility, for these two compounds are -200 K ( $\text{FeCr}_2\text{S}_4$ [3]) and -45 K ( $\text{FeSc}_2\text{S}_4$ [3]) (see Fig. 5.1).

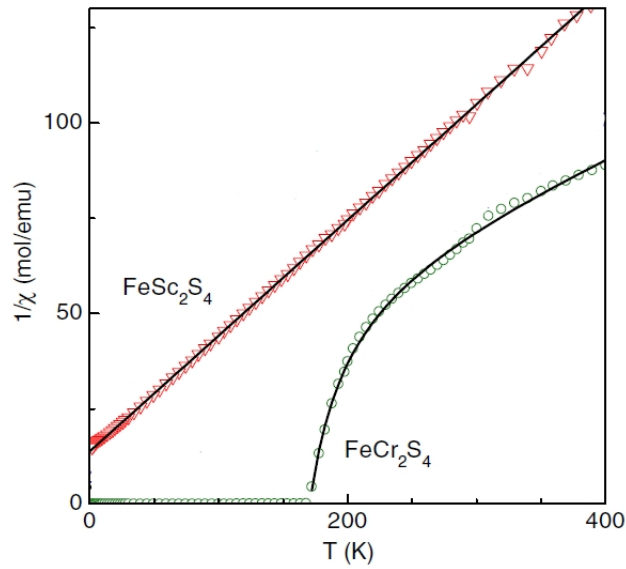


**Figure 5.1** Inverse susceptibility  $1/\chi(T)$  of  $\text{FeSc}_2\text{S}_4$  (triangles), and  $\text{FeCr}_2\text{S}_4$  (circles), respectively. The straight solid lines are linear fits with a Curie-Weiss law  $\chi = C/(T - \Theta_{CW})$ . The figure is taken from Ref. [3].

In literature the frustration parameter is defined as  $f = \frac{-\Theta_{CW}}{T_N}$  [4], where  $T_N$  is the magnetic transition temperature. For  $\text{FeCr}_2\text{S}_4$  this turns out to be 1.2, whereas for  $\text{FeSc}_2\text{S}_4$ , the value of this parameter turns out to be more than 1000. To the best of our knowledge, the microscopic understanding of this qualitatively different behavior has not been attempted till date. Experimental works[3, 2, 1] on this topic have been reported, also related theoretical work based on model Hamiltonian [5, 6, 7] has been performed. We carried out first principles calculations to study the root cause behind this dissimilar

behaviour of those two sulphide spinel from microscopic point of view.

### 5.3 Results and Discussions

For our DFT-based calculations we have considered three different basis sets, namely, the LAPW method as implemented in the WIEN2K code, the muffin-tin orbital based Nth-order MTO (NMTO) method as implemented in the Stuttgart code and the plane-wave basis as implemented in the VASP. The reliability of the calculation in the three basis sets has been cross-checked.

Both the spinel compounds crystallize in the conventional cubic  $Fd\bar{3}m$  symmetry, with lattice parameters 9.99 Å[1] and 10.50 Å[8], for  $\text{FeCr}_2\text{S}_4$  and  $\text{FeSc}_2\text{S}_4$  respectively. There is a 5% expansion in the Sc compound due to large  $\text{Sc}^{3+}$  ions (size  $\approx 0.75$  Å) compared to that of  $\text{Cr}^{3+}$  ions (size  $\approx 0.62$  Å). The other free structural parameter *i.e.* position of S ion is given by 0.259 and 0.255 for  $\text{FeCr}_2\text{S}_4$  and  $\text{FeSc}_2\text{S}_4$  respectively [9, 8]. This leads to a trigonal distortion in the  $\text{BS}_6$  octahedra in the compounds. For  $\text{FeCr}_2\text{S}_4$  the deviation of S-B-S angle from  $90^\circ$  is  $4.4^\circ$ , where as the same for  $\text{FeSc}_2\text{S}_4$  is  $2.5^\circ$ .

#### 5.3.1 Density of States

Fig. 5.2 shows the non spin-polarized DOS calculated using LAPW basis set within the generalized gradient approximation. The number of plane waves is restricted using the criteria muffin-tin radius multiplied by  $k_{max}$  yielding a value of 7. The total Brillouin zone (BZ) was sampled with 256 k points for self consistent calculations.

In order to check the influence of the crystal structure differences between Cr and Sc compounds on the electronic properties of the crystal structure, we have performed calculations to study the electronic structure of  $\text{FeSc}_2\text{S}_4$  considering crystal structure of  $\text{FeCr}_2\text{S}_4$ . The top panel of Fig. 5.2 shows the DOS of  $\text{FeSc}_2\text{S}_4$  obtained considering the actual crystal structure in comparison with the DOS obtained assuming the crystal structure of  $\text{FeCr}_2\text{S}_4$ . On the other hand, the bottom panel shows the comparison of DOS between  $\text{FeSc}_2\text{S}_4$  and  $\text{FeCr}_2\text{S}_4$  both in their actual crystal structure. Focusing on the DOS shown in the top panel of Fig. 5.2, they look similar to each other although they differ in minute details.

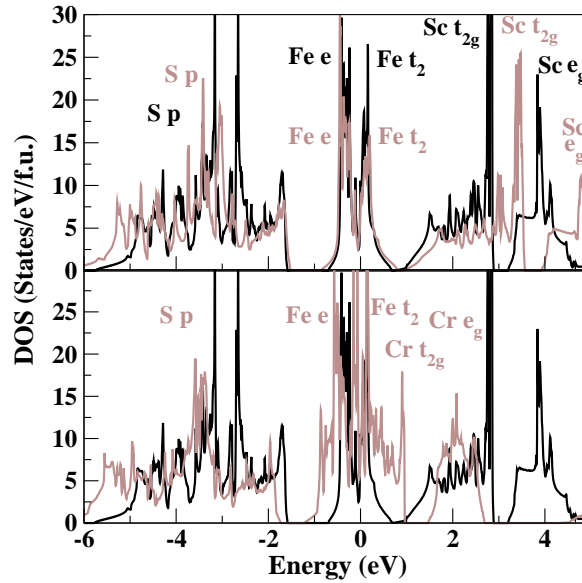


**Figure 5.2** Non spin-polarized total DOS calculated within GGA. Top panel shows DOS of  $\text{FeSc}_2\text{S}_4$  calculated in the actual crystal structure (dark solid line) and in the crystal structure of  $\text{FeCr}_2\text{S}_4$  (light solid line). Bottom panel represents comparison of DOS of  $\text{FeSc}_2\text{S}_4$  (dark solid line) and  $\text{FeCr}_2\text{S}_4$  (light solid line). Energy is plotted with respect to the Fermi energy ( $E_F$ ). The various orbital contributions are marked for each DOS plots.

For example, the Fe  $d$  dominated states at the Fermi level ( $E_F$ ) are a bit narrower in actual crystal structure of  $\text{FeSc}_2\text{S}_4$  compared to that of hypothetical lattice. Also in the positioning of the empty Sc levels spanning the energy window of about 1-5 eV differ little bit between the two DOS. On the other hand, significant differences can be spotted while comparing the DOS of two actual compounds (lower panel of Fig. 5.2). It can be clearly seen that bandwidth of the Fe  $d$  dominated states crossing  $E_F$  is substantially increased and also one can notice easily that there is a significant change in the unoccupied region of the DOS profile. This comparison makes it clear that the difference between  $\text{FeCr}_2\text{S}_4$  and  $\text{FeSc}_2\text{S}_4$  arises from the relative energy positions of Cr and Sc with respect to that of Fe. This is more evident from the spin-polarized band structure calculation which is discussed in next section.

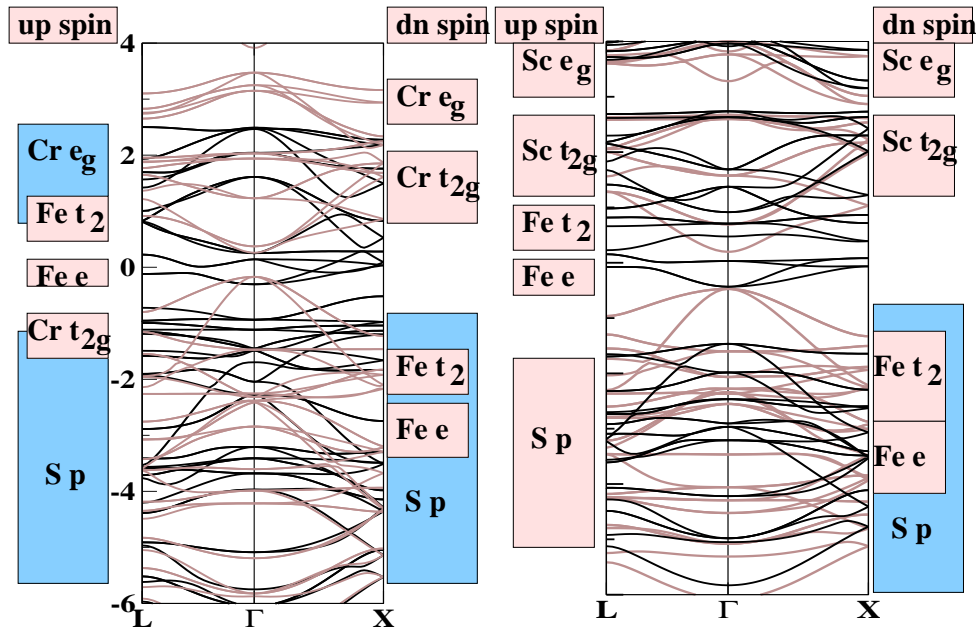


**Figure 5.3** Spin-polarized band structure calculated within GGA. Energy is plotted with respect to  $E_F$ . Left and right panel show band structure of  $\text{FeCr}_2\text{S}_4$  and  $\text{FeSc}_2\text{S}_4$  respectively. The dark lines represent the bands corresponding to up spin channel and light colored line represent the bands corresponding to down spin channel.

### 5.3.2 Band structure

Fig. 5.3 shows the comparison of spin-polarized band structures between the two spinel compounds discussed in this chapter. In spite of the fact that  $\text{FeSc}_2\text{S}_4$  does not spin order, such calculations are useful in understanding the relative positions of Fe and the cation B (Cr/Sc) energy levels taking into account the spin degrees of freedom. Fe and Cr/Sc  $d$  states are split into  $e$ ,  $t_2$  and  $t_{2g}$ ,  $e_g$  states, respectively since those ions occupy the tetrahedral and octahedral sites respectively. On top of that, these states are spin-split also. The Fe  $d$  dominated states are completely occupied in the down spin channel. Considering the up spin channel, One can notice that Fe  $e$  states are partially occupied. This is in agreement with the  $\text{Fe}^{2+}$  nominal valence in both the spinel compounds. In  $\text{FeSc}_2\text{S}_4$ , Sc  $d$  states are empty in both spin channels with little shift in the energy scale between the two spin channels. This essentially proves the non-magnetic character of  $\text{Sc}^{3+}$  in the compound. Looking at the Cr  $d$  states at

the down spin channel, one can see that the states are completely empty. On the other hand, in the other spin channel *i.e.* up spin channel,  $t_{2g}$  states are occupied and  $e_g$  states are empty with a spin splitting of about 2 eV between the two. This proves the ferrimagnetic spin arrangements between Fe and Cr in  $\text{FeCr}_2\text{S}_4$  compound. Therefore it has been clearly shown that the difference between two sulphide spinel compounds arises from the relative energy positions of Cr and Sc with respect to that of Fe. While the Sc  $d$  levels all appear above the Fe  $d$  states with little mixing between them, there exists a rather strong mixing between Fe  $d$  and Cr  $d$  states in the up spin channel. Fe-Cr mixing causes the substantial increase in the width of the Fe  $d$  dominated states crossing  $E_F$  (see Fig. 5.2).

### 5.3.3 Effective Fe-Fe interaction

We have performed NMTO downfolding calculation in order to extract the effective Fe-Fe interaction in the two spinel compounds. In our downfolding calculations, we have kept active Fe  $d$  states and have downfolded all the other states involving Cr/Sc and S. In the Fig. 5.4 we show Fe  $d_{xy}$  Wannier function for  $\text{FeCr}_2\text{S}_4$  and  $\text{FeSc}_2\text{S}_4$ . It can be clearly seen that central region of the Wannier function is shaped according to the  $d_{xy}$  symmetry, while the tails are shaped according to the integrated out orbital degrees of freedom, e.g., Cr/Sc and S orbitals. From Fig. 5.4 it can be seen that Wannier function for Cr compound is much more delocalized compared to that of Sc compound with significant weights at the Cr sites surrounding the central Fe site. In contrast, the Wannier function for  $\text{FeSc}_2\text{S}_4$  is localized with little weight on Sc sites and only some weight on the neighbouring S sites.

In the effective Wannier function basis of Fe, real-space Hamiltonian is constructed, which is tabulated in Table 5.1. In doing so we have considered up to second nearest-neighbour (2NN) interactions. If we focus on the hopping parameters listed in Table 5.1, we find that the most significant changes between the hopping parameters of  $\text{FeCr}_2\text{S}_4$  and  $\text{FeSc}_2\text{S}_4$  are within the  $t_2$  ( $d_{xy}$ ,  $d_{yz}$  and  $d_{xz}$ ) block of the Hamiltonian. We have noticed that the Fe-Fe nearest-neighbour (NN) hopping integrals are larger than the 2NN hopping terms for the Cr compound. In fact our calculation reveals that, in case of  $\text{FeCr}_2\text{S}_4$  the largest 2NN hopping is about three times smaller than the largest NN hopping term. Interestingly we have found that reverse case is true for  $\text{FeSc}_2\text{S}_4$  compound. The 2NN hoppings are larger than the

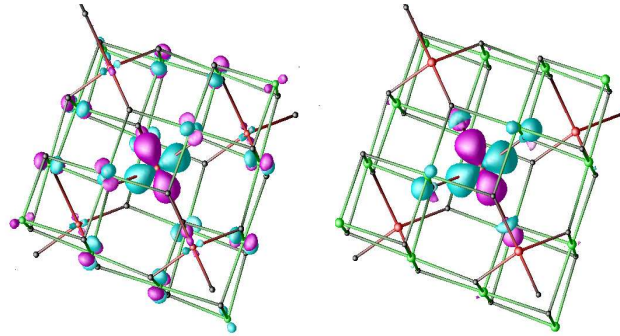


**Figure 5.4** Wannier function plot of Fe  $d_{xy}$  orbital for  $\text{FeCr}_2\text{S}_4$  (left panel) and  $\text{FeSc}_2\text{S}_4$  (right panel). Plotted are the constant value surfaces. Two opposite lobes of the wave functions are colored differently.

NN hoppings for Sc compound.

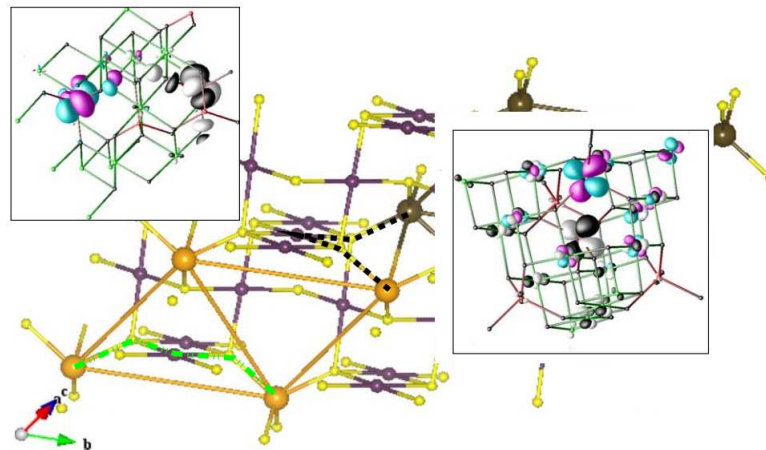


**Figure 5.5** The NN and 2NN interaction path between Fe atoms. Small dark and light balls represent B(Sc/Cr) and S atoms, respectively. Big dark and light balls represent Fe atoms belonging to two FCC sublattices constituting the diamond lattice. The dashed line in black (dark) and green (light), represent the NN and 2NN paths, respectively. The inset in the upper-left (lower right) corner shows the overlap of the Wannier functions of Fe  $d_{xy}$  placed at two Fe atoms in  $\text{FeSc}_2\text{S}_4$  ( $\text{FeCr}_2\text{S}_4$ ) separated by 2NN (NN) distance.

Two A ions in a typical spinel lattice are connected via A-X-B-X-A path, which is true for both NN and 2NN A-site ions. This interaction path is shown in Fig. 5.5. The A-site sublattice of spinel structure

forms diamond like lattice (see Fig. 5.6). Diamond lattice is actually composed of two interpenetrating face-centered cubic (FCC) lattices. NN interactions connect two A-site ions belonging to two different FCC lattice, where as 2NN interactions happen between two A-site ions belonging to same FCC lattice.

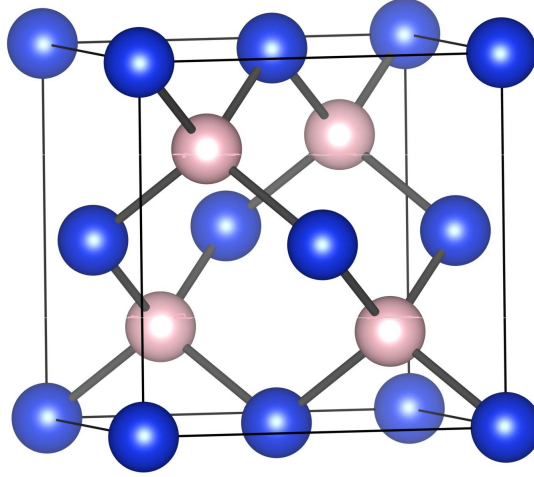


**Figure 5.6** A-site sub-lattice of spinel structure (diamond lattice) consisting of two interpenetrating FCC lattices. Dark and light coloured atoms form two FCC lattices separately.

The NN hopping path as marked in Fig. 5.5, includes Fe-B-Fe, Fe-S-Fe, and S-B-S bond angles of about  $60^\circ$ ,  $80^\circ$ , and  $90^\circ$ , respectively, while the corresponding bond angles for the 2NN hopping paths are found to be close to  $120^\circ$ ,  $130^\circ$ , and  $90^\circ$ , respectively<sup>†</sup>. Therefore it is important to note that the direct Fe-B hybridization becomes important for NN interaction. On the other hand for the 2NN interaction, the anion mediated (Fe-S-Fe) exchange becomes important. Since for  $\text{FeSc}_2\text{S}_4$  the Fe-Sc hybridization is much less, NN interaction in this compound becomes less dominant compared to 2NN interaction. The fact that the NN interaction is strong in  $\text{FeCr}_2\text{S}_4$  and the 2NN interaction is strong in  $\text{FeSc}_2\text{S}_4$  is supported by the plot of the Wannier functions for two NN Fe sites (top left panel of Fig. 5.5) and two 2NN Fe sites (bottom right panel of Fig. 5.5). One can easily find from Fig. 5.5, a clear overlap of Cr-like tails between two Wannier functions for  $\text{FeCr}_2\text{S}_4$ . On the other hand, for  $\text{FeSc}_2\text{S}_4$ , the S-like tails point to each other.

<sup>†</sup>These numbers vary slightly between  $\text{FeCr}_2\text{S}_4$  and  $\text{FeSc}_2\text{S}_4$ .

	NN	2NN		
m,m'	$[\frac{1}{4}\frac{1}{4}\frac{1}{4}]$	$[0\frac{1}{2}\frac{1}{2}]$	$[\frac{1}{2}0\frac{1}{2}]$	$[\frac{1}{2}\frac{1}{2}0]$
1,1	-3 60 <b>63</b>	43 12 <b>31</b>	43 12 <b>31</b>	-16 -13 <b>3</b>
2,2	-3 60 <b>63</b>	-16 -13 <b>3</b>	43 12 <b>31</b>	43 12 <b>31</b>
3,3	11 10 <b>1</b>	-6 -1 <b>5</b>	-6 -1 <b>5</b>	-21 2 <b>23</b>
4,4	-3 60 <b>63</b>	43 12 <b>31</b>	-16 -13 <b>3</b>	43 12 <b>31</b>
5,5	11 10 <b>1</b>	-16 1 <b>17</b>	-16 1 <b>17</b>	-1 -2 <b>1</b>
1,2	-10 -9 <b>1</b>	-22 11 <b>33</b>	46 17 <b>29</b>	22 -11 <b>33</b>
1,3	-22 -18 <b>4</b>	16 8 <b>8</b>	16 8 <b>8</b>	-11 -22 <b>11</b>
1,4	-10 -9 <b>1</b>	46 17 <b>29</b>	-22 11 <b>33</b>	22 -11 <b>33</b>
1,5	0 0 <b>0</b>	-18 3 <b>21</b>	18 -3 <b>21</b>	0 0 <b>0</b>
2,3	11 9 <b>2</b>	4 11 <b>7</b>	7 -7 <b>0</b>	-24 -1 <b>23</b>
2,4	-10 -9 <b>1</b>	22 -11 <b>33</b>	-22 11 <b>33</b>	46 17 <b>29</b>
2,5	-19 -16 <b>3</b>	-7 -19 <b>12</b>	23 5 <b>18</b>	5 8 <b>3</b>
3,4	11 9 <b>2</b>	-7 7 <b>14</b>	4 11 <b>7</b>	24 1 <b>23</b>
3,5	0 0 <b>0</b>	9 -2 <b>11</b>	-9 2 <b>11</b>	0 0 <b>0</b>
4,5	19 16 <b>3</b>	-23 -5 <b>18</b>	7 19 <b>12</b>	-5 -8 <b>3</b>

**Table 5.1** Hopping matrix elements (in meV) of  $\text{FeSc}_2\text{S}_4$  and  $\text{FeCr}_2\text{S}_4$  (first two values of each column, respectively) and the magnitude of their differences (third value of each column) for the NN  $[\frac{1}{4}\frac{1}{4}\frac{1}{4}]$  and 2NN  $[0\frac{1}{2}\frac{1}{2}]$ ,  $[\frac{1}{2}0\frac{1}{2}]$ ,  $[\frac{1}{2}\frac{1}{2}0]$ . The matrix elements are listed for distinct entries only. 1, 2, 3, 4, and 5 represent the five  $d$  orbitals,  $d_{xy}$ ,  $d_{yz}$ ,  $d_{3z^2-1}$ ,  $d_{xz}$ , and  $d_{x^2-y^2}$ , respectively.

### Fe-Fe exchange interactions

One can estimate the exchange interactions from the hopping integrals through the use of a superexchange like formula. However this kind of approach relies on the knowledge of the appropriate charge-transfer energy, which is indeed difficult to estimate because of complicated hopping paths. The alternate way to compute the effective magnetic exchange interactions, is in terms of total energy

calculations of different spin arrangements and mapping the total energies to an Ising-type model. We considered the second approach to estimate the Fe-Fe magnetic exchange interactions in the two sulphide spinel compounds. For this purpose, spin-polarized calculations were carried out in a plane wave basis as implemented in VASP and with the choice of the GGA exchange-correlation functional. Our calculations shows that for  $\text{FeSc}_2\text{S}_4$ ,  $J_1=-0.01$  meV and  $J_2=-0.37$  meV with  $J_2/J_1=37$ , where  $J_1$  and  $J_2$  are the magnetic exchange interaction between NN and 2NN Fe ions respectively. This proves that 2NN exchange interaction dominates over NN exchange interaction which has already been inferred from our estimated hopping integrals. This result is also in agreement with the findings of neutron scattering measurements [2]. On the other hand, our calculation shows that for  $\text{FeCr}_2\text{S}_4$   $J_1=6$  meV and  $J_2=2.5$  meV, both the exchange interactions being ferromagnetic in nature. For Cr compound the NN interaction dominates over the 2NN neighbour interaction. For Cr compound it turns out that  $J_2/J_1=0.4$ , which is in sharp contrast with that of Sc compound.

#### 5.3.4 Effect of spin-orbit coupling

	Fe		Cr/Sc		Anisotropy energy (meV/Fe)
	Orbital moment	spin moment	Orbital moment	spin moment	
$\text{FeSc}_2\text{S}_4$	-0.14	-3.44	0.0	0.05	6
$\text{FeCr}_2\text{S}_4$	-0.13	-3.27	-0.03	2.69	10

**Table 5.2** Magnetic moments of Fe and Cr/Sc ions in  $\mu_B$  and anisotropy energy in meV/Fe.

Due to the presence of unquenched orbital degrees of freedom on the Fe sites, the importance of the spin-orbit coupling (SOC) in these compounds has been discussed in the literature [5, 6]. Relative strength of SOC parameter  $\lambda$  is an important quantity in this context. Table 5.2 shows the magnetic moments of Fe and Cr/Sc ions, obtained from GGA+ $U$ +SO calculations carried out for both  $\text{FeCr}_2\text{S}_4$  and  $\text{FeSc}_2\text{S}_4$  structures. These calculations are done within LAPW basis sets as implemented in Wien2k

code, with following U and J value, U=2.5eV and J=1eV. From our calculations we got rather large moment of 0.13 - 0.14  $\mu_B$  at Fe site for both FeSc<sub>2</sub>S<sub>4</sub> and FeCr<sub>2</sub>S<sub>4</sub>, with the spin moment pointing along the same direction as that of orbital moment. Such values of orbital moments are surprisingly large given the fact that the orbitally active levels of Fe are *e* levels. The reason behind this has been discussed in previous chapter, as the finite coupling between Fe *e* and empty *t*<sub>2</sub> orbitals. We have also evaluated magnetocrystalline anisotropy energy, which is obtained as the total energy difference between the calculations with the spin quantization along [001] and [110]. In our calculation it has been found that the anisotropy energy is approximately two times larger for FeCr<sub>2</sub>S<sub>4</sub> compared to FeSc<sub>2</sub>S<sub>4</sub>. This strongly indicates stronger spin-orbit interaction in Cr compound compared to Sc compound. The strength of the effective spin-orbit interaction depends on the energy level separation ( $\Delta$ ) between Fe *e* and *t*<sub>2</sub>. From NMTD downfolding calculations we have estimated  $\Delta$  for both FeSc<sub>2</sub>S<sub>4</sub> and FeCr<sub>2</sub>S<sub>4</sub>, which are 0.46 eV and 0.20 eV respectively. The spin-orbit coupling parameter is given by,  $\lambda \sim \frac{6\lambda_0^2}{\Delta}$ , where  $\lambda_0$  is the atomic spin orbit coupling constant, estimated to be 0.01 eV. Next using estimated values of  $\Delta$  for both FeSc<sub>2</sub>S<sub>4</sub> and FeCr<sub>2</sub>S<sub>4</sub>, we get  $\lambda_{Sc} = 1.3$  meV and  $\lambda_{Cr} = 3$  meV. If we consider only the dominant magnetic interaction for each of the two compounds then we get  $\frac{\lambda}{J} \gg 1$  in FeCr<sub>2</sub>S<sub>4</sub> compound and  $\frac{\lambda}{J} \ll 1$  in FeSc<sub>2</sub>S<sub>4</sub>. These two situations will give rise to very different ground states, an magnetically ordered state for  $\frac{\lambda}{J} \gg 1$  and a spin orbital singlet for  $\frac{\lambda}{J} \ll 1$  [5, 6].

## 5.4 Conclusion

We have carried out DFT calculations to provide a microscopic understanding of the dissimilar behavior of two spinel compounds, FeSc<sub>2</sub>S<sub>4</sub> and FeCr<sub>2</sub>S<sub>4</sub>. Our study reveals that this difference in behaviour originates from the difference in the hybridization between Fe *d* states and B (B=Cr/Sc) *d* states and S *p* states. Our study shows that this not only affects the magnitude of magnetic exchanges but also the relative importance of different magnetic exchanges. In our calculation we got a contrasting value of J<sub>2</sub>/J<sub>1</sub> of 37 in the case of the Sc compound to a value of 0.4 in the case of the Cr compound. Not only that, the J's are antiferromagnetic for the Sc systems and ferromagnetic for the Cr system. This leads

---

to important frustration effects in the  $\text{FeSc}_2\text{S}_4$  which are absent in the  $\text{FeCr}_2\text{S}_4$ .

# Bibliography

- [1] M. S. Park, S. K. Kwon, S. J. Youn, and B. I. Min, *Phys. Rev. B* **59**, 10018–10024 (1999).
- [2] A. Krimmel, M. Mücksch, V. Tsurkan, M. M. Koza, H. Mutka, and A. Loidl, *Phys. Rev. Lett.* **94**, 237402 (2005).
- [3] N. Büttgen, J. Hemberger, V. Fritsch, A. Krimmel, M. Mücksch, H.-A. K. von Nidda, P. Lunkenheimer, R. Fichtl, V. Tsurkan, and A. Loidl, *New Journal of Physics* **6**, 191 (2004).
- [4] L. Balents, *Nature* **464**, 199 – 208 (2010).
- [5] G. Chen, A. P. Schnyder, and L. Balents, *Phys. Rev. B* **80**, 224409 (2009).
- [6] G. Chen, L. Balents, and A. P. Schnyder, *Phys. Rev. Lett.* **102**, 096406 (2009).
- [7] D. Bergman, J. Alicea, E. Gull, S. Trebst, and L. Balents, *Nat Phys* **3**, 487 – 491 (2007).
- [8] A. Krimmel, personal communication.
- [9] G. Shirane, D. E. Cox, and S. J. Pickart, *Journal of Applied Physics* **35**, 954–955 (1964).

## Chapter 6

# Electronic and optical properties of spinel

## $\text{CuIr}_2\text{S}_4$ <sup>†</sup>

### 6.1 Introduction

One of the most studied topics in condensed matter physics in last few decades is metal-insulator transition (MIT). After the discovery of high- $T_c$  cuprates[1] and manganites[2], attention of researchers has been drawn to this phenomenon due to its vast application possibilities. It is a commonly occurring phenomenon among transition-metal oxides and sulphides, although its origin seems to be varied. For example in  $\text{V}_2\text{O}_3$ , MIT occurs due to correlation induced enhancement of crystal field splitting[3]. On the other hand in case of magnetite  $\text{Fe}_3\text{O}_4$ , in literature[4] it has been discussed that the root cause behind the MIT shown by this compound is correlation assisted charge-ordering transition between  $\text{Fe}^{2+}$  and  $\text{Fe}^{3+}$ . Many of the compounds belonging to spinel class exhibit MIT. These compounds show complicated ordering at low temperature with associated MIT from a high-temperature (HT) metallic phase.  $\text{CuIr}_2\text{S}_4$  is one such spinel compound which has been reported to undergo a first-order MIT near 230 K simultaneous to structural phase transition [5].

---

<sup>†</sup>This chapter is based on *Phys. Rev. B* 79, 113104 (2009)

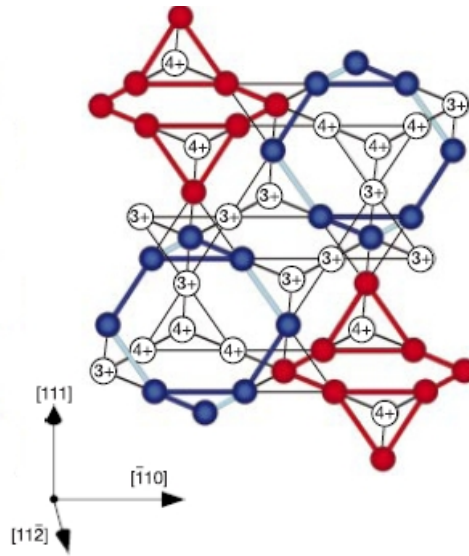


**Figure 6.1** A view of the 3D configuration of the Ir ions, emphasizing the orientation of the hexagonal rings perpendicular to the  $[111]$  cubic direction. Red and blue colour atoms represent  $\text{Ir}^{3+}$  and  $\text{Ir}^{4+}$ , respectively. The dimerized Ir-Ir bonds are indicated with light-blue cylinders. In the projection, the  $[111]$  cubic direction is tilted by approximately  $18^\circ$  out of the paper plane to create a 3D impression of the stacking and to provide a prospective view of both types of octamers. The charge-ordering pattern is also indicated. The  $\text{Ir}^{3+}$  hexagons lie essentially in the  $[111]$  planes whereas the  $\text{Ir}^{4+}$  hexagons lie in the  $(1,1,\bar{1})$  planes. Spin dimerization of the  $\text{Ir}^{4+}$  ions takes place along the two orthogonal cubic directions  $[101]$  and  $[1,0,\bar{1}]$ . This figure is taken from Ref. [7].

## 6.2 Motivation of the present work

HT phase of  $\text{CuIr}_2\text{S}_4$  has a cubic spinel structure with  $Fd\bar{3}m$  symmetry [6]. On lowering of temperature the system undergoes reduction of symmetry. The low-temperature (LT) structure was initially characterized to be tetragonal[6] (space group  $I4_1/amd$ ), although the study also reported observation of additional Bragg peaks which were not indexed. The neutron measurement by Radaelli *et. al.*[7] revealed a fascinating octamer ordering in LT  $\text{CuIr}_2\text{S}_4$  with a triclinic space group (see Fig. 6.1). The octamer ordering consists of tetramerization of Ir-Ir bonds with short, long, and intermediate bond lengths giving rise to octamer clusters, one of which exhibits alternation of Ir-Ir bond lengths.

Croft *et. al.*[8] has explained formation of such superstructures in terms of formation of corre-

lated spin singlet dimers. Similar explanation can also be found in case of  $\text{VO}_2$ [9]. NMR experiments reports[10] Cu to be in monovalent state in  $\text{CuIr}_2\text{S}_4$ . Therefore if one assumes S to be in divalent state in this compound then Ir sites are nominally in the 3.5+ state, which is a mixed valent state. At low temperature, Ir ions are therefore expected to charge disproportionate into  $\text{Ir}^{3+}$  and  $\text{Ir}^{4+}$ .  $\text{Ir}^{3+}$  consists of completely filled  $t_{2g}$  states, where as  $\text{Ir}^{4+}$  ions have two filled and one half filled  $t_{2g}$  states. Croft *et. al.* interpreted that  $\text{Ir}^{4+}$  ions with their  $S=1/2$  configuration form correlation assisted spin singlets which lead to alternation of  $\text{Ir}^{4+}-\text{Ir}^{4+}$  bond lengths, while  $\text{Ir}^{3+}-\text{Ir}^{3+}$  bond lengths remain uniform. It should be noted that while in the case of 3d transition metal based oxide systems like  $\text{VO}_2$  or  $\text{Ti}_4\text{O}_7$ , correlation assisted spin singlet formation is of much relevance, in the present case, the ion under study is Ir, which is a 5d element. Furthermore, S being in the 3p state with more extended wave functions compared to O 2p state is expected to give rise to wide bands with much weaker correlation effect. As a consequence, there exists an alternative explanation of MIT, proposed by Khomskii and Mizokawa,[11] in terms of the orbitally driven Peierls state. Ir is the B-site ion in the spinel compound  $\text{CuIr}_2\text{S}_4$ . As discussed in the crystal structure of spinel compounds section, this B-site ions form chains running in criss-cross manner through out the crystal. Significant overlap of Ir  $d$  orbitals aligned along a given chain direction and negligible in other chain directions leads to formation of essentially one-dimensional bands and with proper filling lead to a Peierls-type effect.

In the view of two different ideas, we carried out first principles calculations to study the MIT in  $\text{CuIr}_2\text{S}_4$ . Results of such a first principles calculations may provide indications about the appropriate scenario of the MIT observed in this spinel compound. There have been reports of measurement of optical spectrum on single crystals[12] conducted on both HT and LT structures. The changes observed in the optical conductivity and reflectivity spectra between the high-temperature and low-temperature data are essentially caused by the reconstruction of band structure following the structural changes from high temperature to low temperature. We have studied the influence of such changes in optical properties in terms of electronic structure calculations, using density-functional theory (DFT) calculations.

## 6.3 Results and Discussions

### 6.3.1 Crystal structure

It is already mentioned that  $\text{CuIr}_2\text{S}_4$  undergoes MIT near room temperature (230 K). For our calculation of HT cubic structure of  $\text{CuIr}_2\text{S}_4$  we considered  $Fd\bar{3}m$  symmetry with lattice parameter  $a=9.847 \text{ \AA}$  and S ion position (free parameter  $u$  of cubic spinel structure) as 0.385 [6]. For LT structure, the symmetry is triclinic ( $P\bar{1}$ )[13, 14, 15]. The LT unit cell corresponds to four times of that of HT phase and the superstructure arises due to the large displacement of the Ir sites. As discussed in previous section, at low temperature phase of  $\text{CuIr}_2\text{S}_4$ , Ir ions exist in two different classes,  $\text{Ir}^{4+}$  (dimerized Ir) and  $\text{Ir}^{3+}$  (non-dimerized Ir). There are eight independent Ir atoms in the low temperature phase. Out of them four form very short metal-metal bonds of average bond length  $3.0 \text{ \AA}$  with each other across shared octahedral faces. All the other Ir-Ir distances being between  $3.43$  and  $3.66 \text{ \AA}$  (see Fig. 6.1). The two types of Ir-dimerized ( $\text{Ir}^{4+}$ ) and non-dimerized ( $\text{Ir}^{3+}$ ) are marked in blue and red, respectively, in Fig. 6.1. Atoms of each type are arranged in octamers, groups of 8 octahedra, related in pairs by the centre of symmetry. Such a structure can be thought of as planar hexagonal rings with two additional octahedra attached at opposite sides, above and below the hexagon (bi-capped hexagonal rings). The Ir ions (with the spin values of  $1/2$ ) in the  $\text{Ir}^{4+}$  octamers exhibit drastic alternations of Ir-Ir distances ( $3.0 \text{ \AA}$  and  $3.5 \text{ \AA}$ ), which results in spin dimerization. On the other hand, the Ir-Ir distance in  $\text{Ir}^{3+}$ -octamers ( $S = 0$ ) remain uniform.

### 6.3.2 Density of states

The calculations have been carried out with no shape approximation to the potential and charge density. The basis has been chosen to be LAPW as implemented in Wien2K code. For the number of plane waves, the criterion used was muffin-tin radius multiplied by  $k_{max}$  (for the plane wave) yielding a value of 7. The number of k points used in the irreducible part of the Brillouin zone was 104 for the self-consistent calculation and 256 for the optical calculation.

Fig. 6.2 represents DOS as obtained in generalized gradient approximation (GGA) of the exchange-

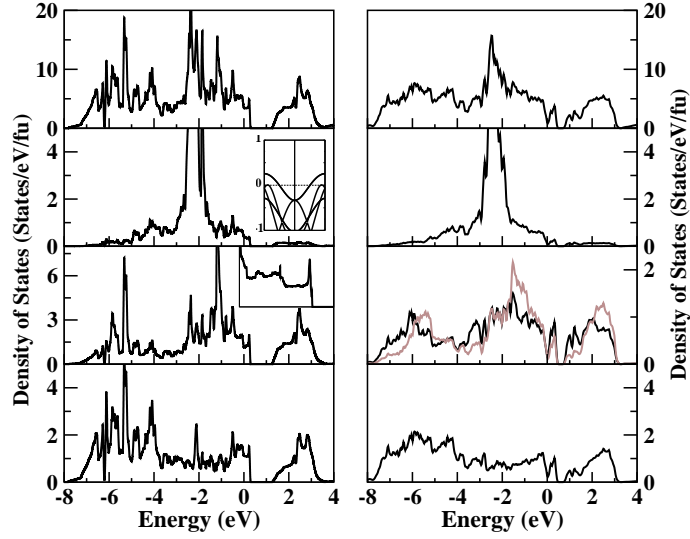


**Figure 6.2** The total and orbital projected DOS of  $\text{CuIr}_2\text{S}_4$  for the high temperature (left panels) and low temperature (right panels) phases, respectively. The panels from top to bottom represent the total DOS, DOS projected on to Cu- $d$ , Ir- $d$  and S- $p$ . The insets in the high-temperature DOS show the band structure and DOS close to  $E_F$  exhibiting predominant 1D-like features. The bands have been plotted along the high symmetry directions [011]-[000]-[110]. The black and the gray lines in panel corresponding to Ir- $d$  projected DOS for the low temperature represent the DOS corresponding the dimerized and undimerized Ir atoms, respectively.

correlation functional. Let us first discuss the DOS of high temperature structure (left panel of Fig. 6.2). One can find significant hybridization between delocalized Ir- $5d$  and S- $3p$  giving rise to wide  $d$ - $p$  hybridized bands spanning the energy range of about 12 eV, from 8 eV below the Fermi energy ( $E_F$ ) to 4 eV above the Fermi energy. The Cu- $d$  derived states localized at an energy of about 2.5 eV below  $E_F$  remain completely occupied in agreement with earlier band-structure calculation[16] and NMR studies[10]. There are distinct indication (see inset of Fig. 6.2) of formation of one dimensional like features near the  $E_F$ , in case of Ir- $d$  projected DOS. This gets merged to a broad filled manifold of Ir  $t_{2g}$  states on moving to energies further away from  $E_F$ . Formation of such 1D-like chains has also been observed in some of spinel compounds, like  $\text{ZnV}_2\text{O}_4$ [17, 18]. In our case, due to the extended character of the Ir- $5d$  orbital the direct overlap of  $t_{2g}$  orbitals which point to each other along a chain direction, gives rise to a bandwidth of about 4 eV. The crystal field splitting of Ir- $t_{2g}$  and Ir- $e_g$  states is about 1 eV.

Ir- $e_g$  states remains empty, which confirms the 3.5+ valence of Ir, with Cu in the monovalent and S in the divalent state.

Let us now study the low temperature DOS carefully. The general features of the DOS remain more or less the same between the HT and LT, significant changes happen close to  $E_F$ . The structural data at the LT phase show there are two inequivalent classes of Ir ions. One of the two Ir classes exhibits alternating Ir-Ir short and long bonds and another forms uniform Ir-Ir bond. In Fig. 6.2 we have plotted Ir- $d$  DOS for both the classes, referred as *dimerized* and *nondimerized* respectively. one can find easily the formation of occupied bonding and unoccupied antibonding-like states close to  $E_F$  for dimerized Ir's. The projected DOS on undimerized Ir's also exhibits this same feature with larger weight on bonding subbands compared to antibonding subbands. The bonding-antibonding feature, however, is more pronounced with almost equal weights between bonding and antibonding subbands in case of dimerized Ir's. This results in charge disproportionation between undimerized and dimerized Ir ions with charges  $5.5+\delta$  and  $5.5-\delta$  with  $\delta = 0.05$ . In case of a  $3d$  transition metal oxide system like  $Ti_4O_7$  this charge disproportionation is found to be nearly complete with Ti in 3+ and 4+ states. This is in contrast with the small value of charge disproportionation of Ir which is a  $5d$  element. This special feature points to a very delocalized character of Ir together with 1D-like properties. The bonding-antibonding splitting originated due to bond tetramerization in Ir chains with an alternation of  $Ir^{3.5-\delta} / Ir^{3.5-\delta} / Ir^{3.5+\delta} / Ir^{3.5+\delta} / \dots$  gives rise to an insulating solution of electronic structure with GGA as is evident from the DOS in Fig. 6.2.

### 6.3.3 Estimation of band gap and effect of Coulomb correlation

From our first principles calculations the band gap value of this system is evaluated as 0.02 eV, which is in agreement with estimates obtained from photoemission study[19]. The gap value, as obtained within GGA, is found to be highly sensitive on the structural details, which is expected since the gap originates from structural changes. In view of this, it would have been preferable to carry out structural optimization. This is, however, hindered by the large unit cell and extremely low symmetry of the low temperature structure.

In order to check the effect of correlation in this spinel compound, we have carried out a LDA+ $U$  calculation. In this calculation the spin arrangement of Ir ions considered is of antiferromagnetic (AFM) type. Such a spin arrangement is considered because of the fact that the true spin singlet state without any long range order is not possible to achieve within a LDA+ $U$  kind of approach. The AFM spin alignment therefore is the closest approximation to assume. This calculation, however, leads to a nonmagnetic solution with vanishingly small magnetic moments at both the dimerized and undimerized Ir sites. This situation is quite different from that of  $\text{Ti}_4\text{O}_7$  case [20]. There a similar kind of approach gave rise to distinctly different magnetic behaviour among  $\text{Ti}^{3+}$  and  $\text{Ti}^{4+}$  like ions. Our first principles results are in contradiction to the idea of correlation assisted localized spins at  $\text{Ir}^{4+}$  ions forming spin singlets. Hence it confirms the expectation of the correlation effect to be much weaker in the case of an Iridium-sulphide system with extended, delocalized  $5d$  and  $3p$  states, compared to  $3d$  metal-oxide systems.

#### 6.3.4 Calculation of optical properties

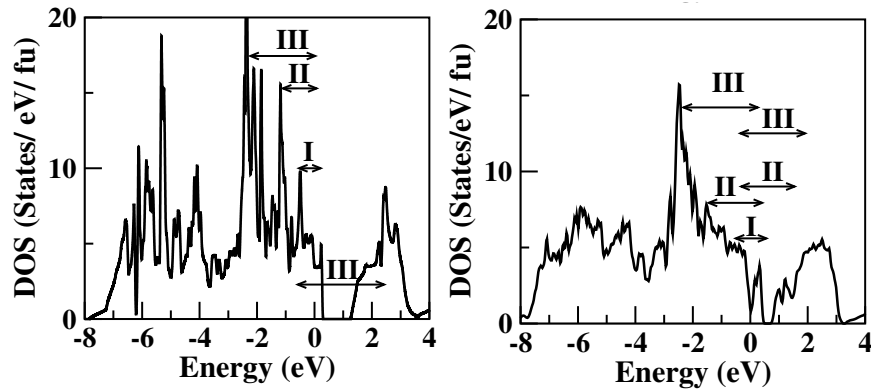


**Figure 6.3** The various allowed optical transitions for photonic energy ranging from 0 to 3 eV in the high-temperature (left panel) and low-temperature (right panel) phases.

Fig. 6.3 shows the various possible optical transitions considering the GGA electronic structure at HT and LT for photonic energy ranging from 0 to 3 eV. It is evident from the Fig. 6.3 the low energy transitions are dominated by Ir  $t_{2g}$ - $t_{2g}$  transitions, which are marked as I and II in the figure. On the

other hand, the higher energy transitions (marked as III) primarily originate from Ir  $t_{2g}$ - $e_g$  transition. In addition to this, Cu- $d$ -Ir  $t_{2g}$  transition also contributes to that peak. These transitions are allowed due to appreciable hybridization between S- $p$  and Cu- $d$  and Ir- $d$  states. In moving from HT to LT structure, marked changes happen in the details of the low energy transitions due to opening of a band gap and formation of bonding and antibonding subbands.

While discussing the optical properties of  $\text{FeCr}_2\text{S}_4$ , we have already mentioned how theoretically optical conductivity and reflectivity can be calculated. Employing the same scheme, we have also calculated the optical properties of  $\text{CuIr}_2\text{S}_4$ . Fig. 6.4 shows the computed reflectivity obtained using the

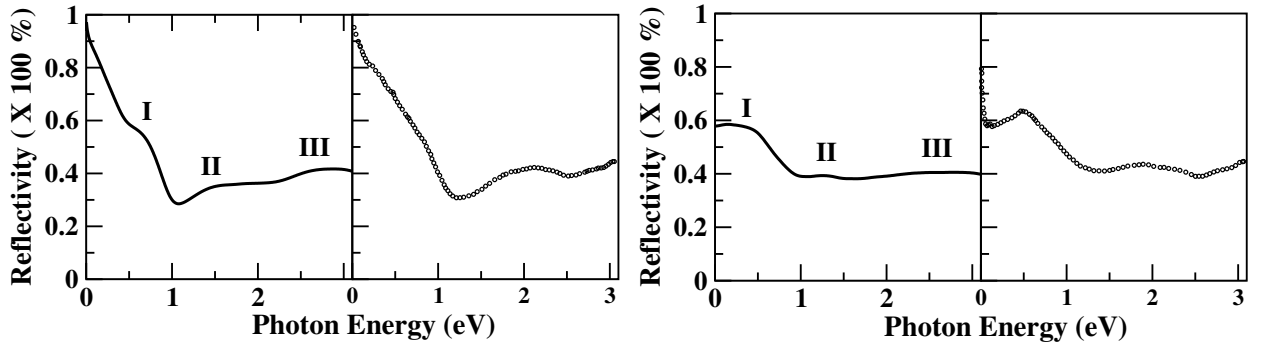


**Figure 6.4** Calculated reflectivity spectrum (solid line) in comparison with the experimental data shown in the dotted lines for the high-temperature (left panels) and low-temperature (right panels) phases. I, II, and III indicate the prominent structures corresponding to optical transitions marked in Fig. 6.3.

joint DOS and the dipole matrix elements. In case of HT phase Drude contribution is added in order to take into account the intraband transitions due to the metallic character of the electronic structure. The added Drude component suppresses a bit the low energy near  $E_F$  Ir  $t_{2g}$ - $t_{2g}$  transition marked as “I” in Fig. 6.3. Although it does not mask it completely and traces of it are still visible in the reflectivity spectra. One can also find the presence of two other peaks marked as structures “II” and “III” originating primarily from transitions relating to Ir  $t_{2g}$  states appearing far away in energy to near  $E_F$   $t_{2g}$  states and Cu- $d$  to Ir- $t_{2g}$  transitions, respectively. We have found in our calculation that in addition to

these transitions the Ir- $t_{2g}$  to empty Ir- $e_g$  transition contributes to both the structures. In Fig. 6.4 we have made a comparison of the theoretically evaluated reflectivity spectra with experimentally measured spectra[12]. One can easily notice that the computed spectra are in reasonably good agreement with the experimental spectra. Although there are certain differences in details; e.g., the structure I in experimental spectra is found to be totally masked by the Drude contribution, while structures II and III are shifted a bit to higher energy (by about 0.2 eV) compared to theoretical spectra. Moving to the low-temperature reflectivity spectrum, shown in the right-hand side panels of Fig. 6.4, the very first thing one can notice that the low-temperature reflectivity drops down to about 60% signaling the insulating character of the LT electronic structure. In LT phase structure I becomes more pronounced which is contributed by the transition between Ir bonding and antibonding subbands. At the same time the structures II and III remain more or less similar to the HT structure. The dip preceding structure II is more pronounced in the case of HT spectra compared to LT spectra, which primarily arises due to the fact that the formation of bonding-antibonding bands in LT pushes the quasi-1D-like portion of the  $t_{2g}$  manifold more toward the broad filled part of the  $t_{2g}$  manifold, compared to the HT electronic structure.

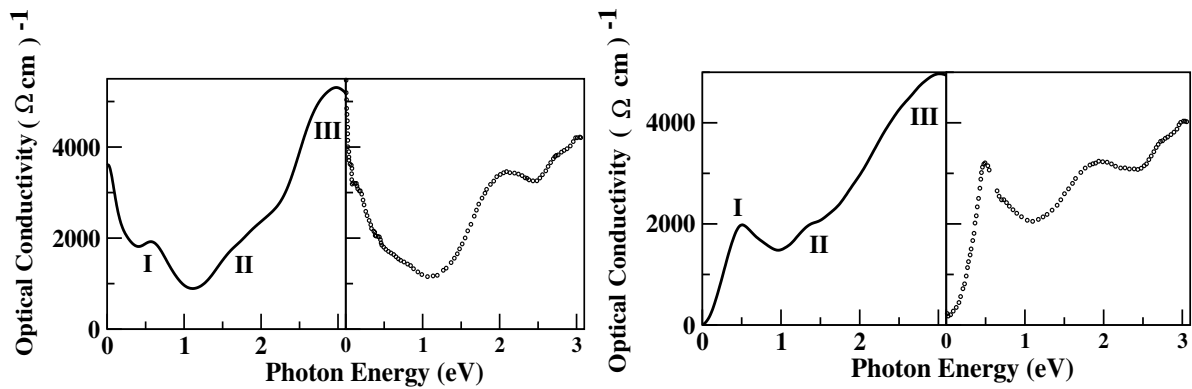


**Figure 6.5** Absorptive part of the calculated diagonal optical conductivity of  $\text{CuIr}_2\text{S}_4$  at high-temperature and low-temperature phases, respectively. Figure convention is same as Fig. 6.4

Fig. 6.5 shows the real part of the computed diagonal conductivity for HT and LT phases of  $\text{CuIr}_2\text{S}_4$  in comparison with experimental spectra. The diagonal conductivity follows the same trend as the cor-

responding reflectivity spectra. Experimental report associates Ir  $t_{2g}$ - $e_g$  transitions to the peak II, while our first-principles calculations show that peak to originate primarily from the transition related to Ir- $t_{2g}$ -Ir- $t_{2g}$ , with the Ir  $t_{2g}$ - $e_g$  transition contributed spectral weight moved mostly to structure III. An optical gap of about 60 meV is obtained from our calculated optical spectrum. This is not apparent in the experimental spectrum presumably because of instrumental broadening. The dc resistivity measurements, however, have yielded an activation energy which is at the most 47 meV [12], at a much better agreement with our calculated value of 20 meV, obtained from band structure.

## 6.4 Conclusion

We have studied the electronic and optical properties of spinel compound  $\text{CuIr}_2\text{S}_4$  at high-temperature and low-temperature phases using the first-principles DFT calculation. Our study finds that correlation has very less effect on the MIT observed in this spinel compound. The transition from HT to LT crystal structure with complex ordering pattern, therefore, may be rationalized in terms of formation of one-dimensional bands which gives rise to an orbitally driven Peierls state. Our theoretically computed reflectivity and conductivity spectra based on the GGA electronic structure are in good agreement with measured spectra. We find the electronic structure to be highly sensitive on the crystal structure data. The observed differences in the details between the theoretical and experimental spectra, we believe, therefore can be improved in terms of better refined crystal structure data at low temperature.

# Bibliography

- [1] A. Damascelli, Z. Hussain, and Z.-X. Shen, *Rev. Mod. Phys.* **75**, 473–541 (2003).
- [2] C. N. R. Rao, A. K. Cheetham, and R. Mahesh, *Chemistry of Materials* **8**, 2421–2432 (1996).
- [3] A. I. Poteryaev, J. M. Tomczak, S. Biermann, A. Georges, A. I. Lichtenstein, A. N. Rubtsov, T. Saha-Dasgupta, and O. K. Andersen, *Phys. Rev. B* **76**, 085127 (2007).
- [4] N. Tsuda, K. Nasu, A. Fujimori, and K. Siratori, *Electronic Conduction in Oxides (Springer Series in Solid-State Sciences)* (Springer, 2000).
- [5] S. Nagata, T. Hagino, Y. Seki, and T. Bitoh, *Physica B: Condensed Matter* **194–196, Part 1**, 1077 – 1078 (1994).
- [6] T. Furubayashi, T. Matsumoto, T. Hagino, and S. Nagata, *Journal of the Physical Society of Japan* **63**, 3333–3339 (1994).
- [7] P. G. Radaelli, Y. Horibe, M. J. Gutmann, H. Ishibashi, C. H. Chen, R. M. Ibberson, Y. Koyama, Y. S. H. V. Kiryukhin, and S. W. Cheong, *Nature* **416**, 155–158 (2002).
- [8] M. Croft, W. Caliebe, H. Woo, T. A. Tyson, D. Sills, Y. S. Hor, S.-W. Cheong, V. Kiryukhin, and S.-J. Oh, *Phys. Rev. B* **67**, 201102 (2003).
- [9] C. Sommers and S. Doniach, *Solid State Communications* **28**, 133 – 135 (1978).
- [10] K.-i. Kumagai, M. Sasaki, K. Kakuyanagi, and S. Nagata, *Hyperfine Interactions* **159**, 181–185 (2004), 10.1007/s10751-005-9094-3.

- 
- [11] D. I. Khomskii and T. Mizokawa, *Phys. Rev. Lett.* **94**, 156402 (2005).
- [12] N. L. Wang, G. H. Cao, P. Zheng, G. Li, Z. Fang, T. Xiang, H. Kitazawa, and T. Matsumoto, *Phys. Rev. B* **69**, 153104 (2004).
- [13] T. SASAKI, M. ARAI, T. FURUBAYASHI, and T. MATSUMOTO, *Journal of the Physical Society of Japan* **73**, 1875–1880 (2004).
- [14] H. Ishibashi, T. Sakai, and K. Nakahigashi, *Journal of Magnetism and Magnetic Materials* **226-230, Part 1**, 233 – 234 (2001), proceedings of the International Conference on Magnetism (ICM 2000).
- [15] W. Sun, T. Kimoto, T. Furubayashi, T. Matsumoto, S. Ikeda, and S. Nagata, *Journal of the Physical Society of Japan* **70**, 2817–2820 (2001).
- [16] T. Oda, M. Shirai, N. Suzuki, and K. Motizuki, *Journal of Physics: Condensed Matter* **7**, 4433 (1995).
- [17] S.-H. Lee *et al.*, *Phys. Rev. Lett.* **93**, 156407 (2004).
- [18] T. Maitra and R. Valentí, *Phys. Rev. Lett.* **99**, 126401 (2007).
- [19] J. Matsuno, T. Mizokawa, A. Fujimori, D. A. Zatsopin, V. R. Galakhov, E. Z. Kurmaev, Y. Kato, and S. Nagata, *Phys. Rev. B* **55**, R15979–R15982 (1997).
- [20] I. Leonov, A. N. Yaresko, V. N. Antonov, U. Schwingenschlögl, V. Eyert, and V. I. Anisimov, *Journal of Physics: Condensed Matter* **18**, 10955 (2006).

## Chapter 7

# Orbital ordering in spinel compound with two orbitally active sites<sup>†</sup>

### 7.1 Introduction

Through the discussions of the previous chapters, it has been clear that spinel compounds have attracted considerable attention in recent times due to the intricate interplay among charge, spin, and orbital degree of freedom, giving rise to fascinating properties. In literature several of the spinel compounds are reported to undergo structural transitions from cubic to tetragonal symmetries, accompanied by orbital ordering as well as magnetic ordering at low temperature[1]. It is interesting to note that theoretical investigations have been mostly restricted to spinels having either an orbitally active B site or A site. For example,  $\text{MnV}_2\text{O}_4$ [2] has the orbitally active B site,  $\text{V}^{3+}$ . We have seen in chapter 3,  $\text{V}^{3+}$  as B-site ion in spinel compound, has  $d^2$  configuration in a threefold degenerate manifold of octahedrally split  $t_{2g}$ , which gives rise to orbital degeneracy. Similar situation can be found in case of another spinel compound  $\text{ZnV}_2\text{O}_4$  [3]. On the other hand in chapter 4, we have studied  $\text{FeCr}_2\text{S}_4$  which exhibits long-range orbital ordering [4]. There the A-site ion Fe has the orbital degree of freedom. In case of  $\text{FeCr}_2\text{S}_4$ ,  $d^6$  configuration of  $\text{Fe}^{2+}$ , with a local  $S = 2$  moment and one hole in twofold degenerate

---

<sup>†</sup>This chapter is based on *Phys. Rev. B* 84, 235112 (2011)

manifold of tetrahedrally split  $e$  states, gives rise to the orbital degeneracy. Similar orbital degree of freedom at A-site ion, has been reported in case of  $\text{FeCr}_2\text{O}_4$  [5] also.

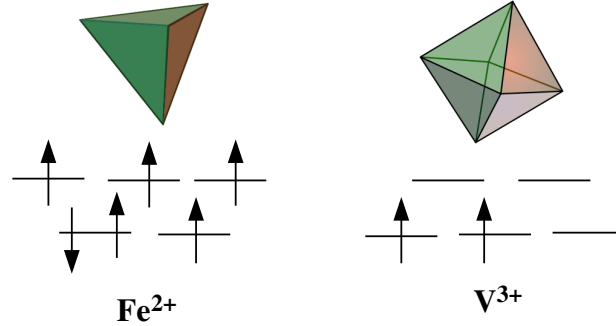


**Figure 7.1** Orbital degeneracy of octahedrally and tetrahedrally split  $\text{Fe}^{2+}$  and  $\text{V}^{3+}$   $d$  levels respectively in spinel compound

It can be interesting to study a case where both the A and B site have orbital degree of freedom. Such a situation arises in case of  $\text{FeV}_2\text{O}_4$ , where A and B site ions are  $\text{Fe}^{2+}$  and  $\text{V}^{3+}$  respectively.

## 7.2 Motivation of the present work

$\text{FeV}_2\text{O}_4$  is reported[6] to exhibit two tetragonal phases (space group  $I4_1/amd$ ), one at relatively higher temperature (140-110 K) and another at relatively lower temperature ( $<70$  K). The symmetry above 140 K is cubic with  $Fd\bar{3}m$  space group. It is interesting to note that for the high-temperature tetragonal (HT-T) phase the  $c$  axis is shorter than the other axis ( $a = b$ ), where as low-temperature tetragonal (LT-T) phase exhibits the opposite trend, with the  $c$  axis being longer than the other axis[7]. The opposite nature of the  $c/a$  ratio in the HT-T and LT-T phases is accommodated by the presence of an orthorhombic phase in the intervening temperature range of 110-70 K. The presence of two tetragonal phases of two different shapes is in contrast to the situations of only A site or only B site orbitally active spinels, for which the tetragonal phase is either compressed as in  $\text{MnV}_2\text{O}_4$  [2] and  $\text{ZnV}_2\text{O}_4$  [3] or elongated as in  $\text{Mn}_3\text{O}_4$  and  $\text{CoMn}_2\text{O}_4$ [8, 9]. It is interesting to study from microscopic point of view the orbital ordering pattern of such a spinel compound with two orbitally active ions, and the driving

mechanism behind the existence of two different tetragonal phases, one at high temperature and other at low temperature.

### 7.3 Crystal structure

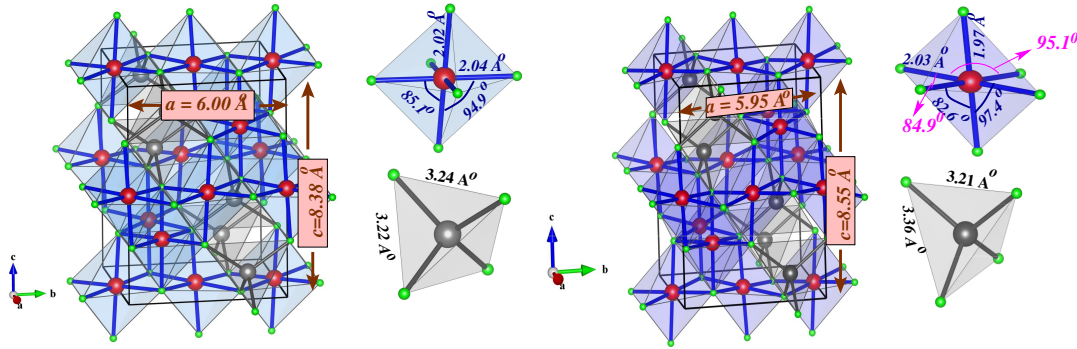


**Figure 7.2** The crystal structures of HT-T (left side panel) and LT-T (right side panel) phases of  $\text{FeV}_2\text{O}_4$ . O sites are indicated with small balls, while Fe and V sites are indicated with grey and red medium-sized balls. The cubic (a, c) and tetragonal (A, C) setting of lattice parameters are related by  $a = \sqrt{2}A$  and  $c = C$ , giving rise to  $c/a = 0.988$  and  $1.016$  for HT-T and LT-T structures, respectively. The  $\text{VO}_6$  and  $\text{FeO}_4$  structural units for both structures are shown separately, along with the various bond lengths and bond angles.

Fig. 7.2 shows the unit cell of the two tetragonal phases of  $\text{FeV}_2\text{O}_4$ . Apart from the HT-T and LT-T phases,  $\text{FeV}_2\text{O}_4$  also exists in cubic (above 140 K) and orthorhombic (110-70 K) phase. We have carried out calculations only on the tetragonal phases. The cubic (a, c) and tetragonal (A, C) setting of lattice parameters are related by  $a = \sqrt{2}A$  and  $c = C$ . This gives rise to  $c/a = 0.988$  and  $1.016$  for HT-T and LT-T structures, respectively. Therefore at high temperature the tetragonal phase is compressed and low temperature tetragonal phase is elongated. In both the tetragonal phases  $\text{VO}_6$  octahedra are compressed. V-O bond length along the  $\langle 001 \rangle$  direction being smaller than that along the  $\langle 100 \rangle$  direction. In addition to this, the octahedra exhibits trigonal distortion, which makes the O-V-O angle deviate from  $90^\circ$ . Interestingly  $\text{FeO}_4$  tetrahedral unit behaves differently in HT-T and LT-T phases.  $\text{FeO}_4$  tetrahedral unit is elongated in the LT-T phase, whereas in HT-T phase the scenario is

opposite *ie.*, FeO<sub>4</sub> tetrahedral unit is compressed there. The tetragonal distortion of FeO<sub>4</sub> tetrahedra is measured in terms of O-O bond lengths ( $d_{O-O}$ ) along  $\langle 110 \rangle$  and  $\langle 101 \rangle$  directions,  $\frac{d_{O-O}\langle 101 \rangle}{d_{O-O}\langle 110 \rangle}$ . Value of this distortion is  $\sim 0.99$  for the HT-T phase and  $\sim 1.05$  for the LT-T phase. While discussing the crystal field splitting of Fe and V  $d$  levels in FeV<sub>2</sub>O<sub>4</sub>, we shall again come to this structural distortion issue.

## 7.4 Results and Discussions

Calculations are carried out in the linear augmented plane wave basis set as implemented in the Wien2K code, as well as the muffin-tin orbital(MTO) based Nth order MTO (NMTO) method as implemented in the Stuttgart code. The density of states and electron-density plots as well as structural optimization are obtained with LAPW calculations with no shape approximation for the potential. For the LAPW calculations, the number of plane waves is restricted using the criteria of muffin-tin radius multiplied by  $k_{max}$ , yielding a value of 7. The Brillouin zone is sampled with 196 irreducible k points for self-consistent calculations. The exchange correlation functional is chosen to be that of generalized gradient approximation (GGA). Strong electron-electron correlation effects are expected to be present in the unfilled  $d$  shell of transition metal sites of a transition metal oxide spinel, which are insufficiently captured by GGA. It is reported that methods like self-interaction-corrected local spin density[10] or hybrid functional[11] have been used to include correlation effects in spinels. In our calculations, the missing Coulomb interaction beyond GGA is supplemented through additional on-site Coulomb interaction, expressed in terms of Coulomb  $U$  and the Hund's rule coupling,  $J_H$  through GGA +  $U$  calculations[12]. For calculations including spin-orbit coupling (SOC), it is included in scalar relativistic form as a perturbation to the original Hamiltonian. The NMTO-downfolding calculation is used to determine the crystal field splitting at Fe and V sites. For this purpose, NMTO-downfolding calculations are carried out keeping only the Fe- $d$  and V- $d$  states active and downfolding all the other states, including O- $p$  states. The on-site block of the real-space Hamiltonian in the Fe- $d$  and V- $d$  bases gives the crystal field splitting.

### 7.4.1 Crystal field splitting

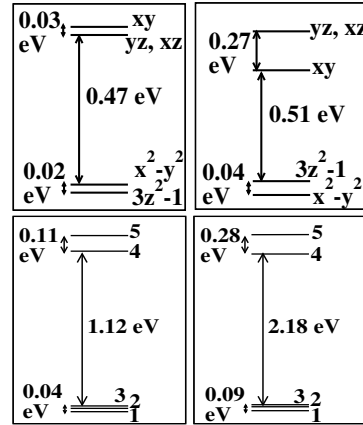


**Figure 7.3** The crystal field splittings of Fe- $d$  (top panels) and V- $d$  (bottom panels) states, computed by the NMTO-downfolding technique. The left and right panels correspond to plots for HT-T and LT-T respectively. For V, due to mixed  $d$  characters, the positions of levels  $|1\rangle \dots |5\rangle$  are shown.

As discussed earlier, the NMTO-downfolding calculation is used to determine the crystal field splitting at Fe and V sites, which is shown in Fig. 7.3. Let us first consider the crystal field splitting at Fe site. The tetragonal distortion of FeO<sub>4</sub> tetrahedra, which is  $\sim 0.99$  for the HT-T phase and  $\sim 1.05$  for the LT-T phase (see section 7.3), lifts the degeneracy between two  $e$  states. Due to different nature of this distortion in HT-T and LT-T phase,  $3z^2 - r^2$  remains below  $x^2 - y^2$  for HT-T and reverse happens in case of LT-T. The tetragonal distortion also leads to splitting within  $t_2$  states, with doubly degenerate  $yz$ ,  $xz$  states and singly degenerate  $xy$ . The relative positioning of the states is shown in Fig. 7.3. Focusing on the V- $d$ -derived states, due to the octahedral splitting V- $d$  levels get split into two major groups  $e_g$  and  $t_{2g}$  with the later being lower in energy. The trigonal distortion coupled with tetragonal distortion not only lifts the degeneracy of V- $d$  states completely but also mixes them. The lowest three levels (referred to as  $|1\rangle, |2\rangle, |3\rangle$ ) are given by predominant contributions of  $xy$ ,  $yz$ , and  $xz$  characters, as listed

below for HT-T and LT-T:

$$|1\rangle^{HT} = -0.239|xz\rangle + 0.969|xy\rangle + 0.050|3z^2 - r^2\rangle$$

$$|2\rangle^{HT} = -0.060|x^2 - y^2\rangle - 0.998|yz\rangle$$

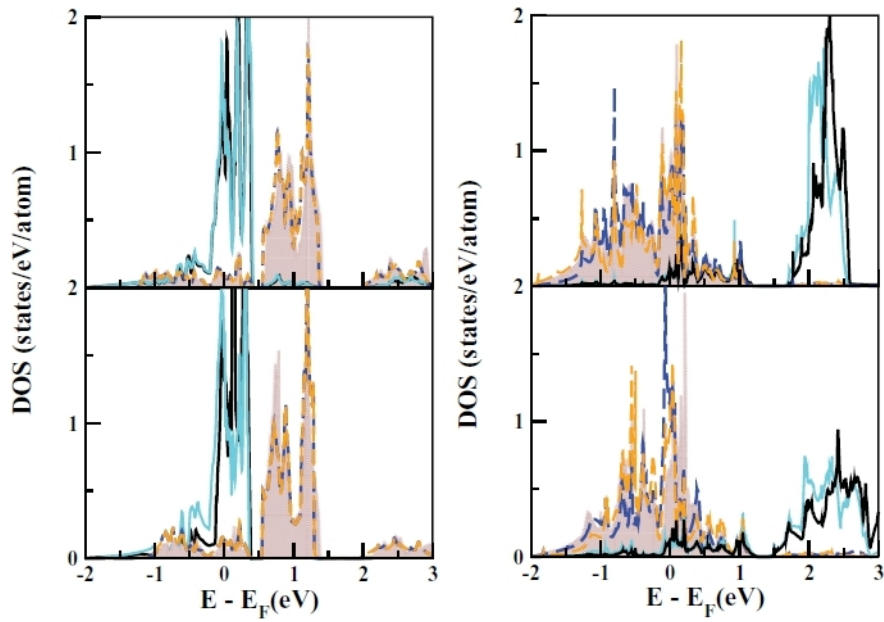
$$|3\rangle^{HT} = 0.970|xz\rangle + 0.240|xy\rangle - 0.020|3z^2 - r^2\rangle$$

$$|1\rangle^{LT} = -0.239|yz\rangle + 0.970|xy\rangle$$

$$|2\rangle^{LT} = 0.119|x^2 - y^2\rangle + 0.990|xz\rangle$$

$$|3\rangle^{LT} = 0.970|yz\rangle - 0.238|xy\rangle + 0.025|3z^2 - r^2\rangle$$

#### 7.4.2 Density of states within GGA



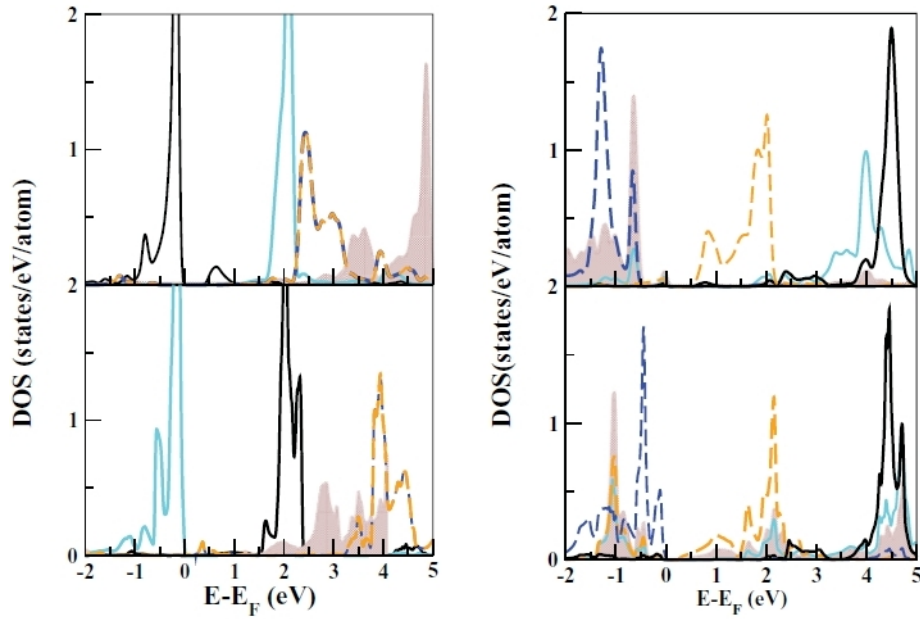
**Figure 7.4** GGA DOS projected onto Fe-*d* (left panel) and V-*d* (right panel) states for HT-T (top panel) and LT-T (bottom panel). Contributions of  $3z^2 - r^2$ ,  $x^2 - y^2$ ,  $xz$ ,  $yz$ , and  $xy$  are represented by black, cyan, dashed blue, dashed orange, and shaded gray regions respectively.

Fig. 7.4 shows the spin-polarized density of states (DOS) calculated within GGA corresponding to

HT-T and LT-T phases, projected on to Fe- $d$  and V- $d$  states. According to magnetic measurements, the magnetic ordering with anti-parallel alignment of Fe and V spins takes place at  $T_C \approx 110$  K. The HT-T phase is, therefore, in paramagnetic (PM) state. In PM state for a transition metal oxide compound, the local moment at transition metal sites orient randomly. Within periodic DFT calculations, as in the present study, it is not possible to simulate the PM state with randomly oriented local moments. Hence, we have carried out spin-polarized calculations for both HT-T and LT-T phases, which is expected to provide knowledge of correct spin states of Fe and V and correct occupations of various  $d$  levels in the presence of local moments. This gives rise to ferrimagnetic alignments of Fe and V moments, which is in accordance with experimental observation[6] of ferrimagnetism at low temperature. We show DOS of majority spin channel of V and minority spin channel of Fe, as the states in the other spin channel are either completely empty or completely occupied (see Fig. 7.1). Focusing on the Fe- $d$ -derived states, one can find clear grouping of states, one around Fermi energy ( $E_F$ ) and another above  $E_F$ , at  $\sim 1$  eV. The first and second grouping are of  $e$  and  $t_2$  characters of Fe- $d$  states respectively. Moving to the V- $d$  derived states, as expected from crystal field splitting, there are two major grouping of states,  $e_g$  and  $t_{2g}$ , with later being lower in energy. The DOS also shows that V- $d$  states gets mixed among themselves substantially.

### 7.4.3 Calculation within GGA+ $U$

Fig. 7.5 shows the GGA+ $U$  DOS for Fe- $d$  and V- $d$  projected states, respectively. We have carried out calculations considering several choices of  $U$  values. The calculations presented here, are carried out with choice of  $U$  values of 4.5 eV at Fe and V sites and  $J_H$  is chosen to be 1 eV. We have seen that variations of  $U$  values do not change the essential results related to orbital ordering, though they do affect the details, for example, the size of the gap. The above choice of  $U$  values leads to an insulating solution for both HT-T and LT-T phase. From theoretical point of view, the effect of  $U$  makes the more occupied states completely occupied and less occupied states empty. Therefore in the minority spin Fe  $3z^2 - r^2$  states get completely occupied and  $x^2 - y^2$  states become completely empty for HT-T phase. The reverse scenario happens in LT-T phase, there  $x^2 - y^2$  states gets fully occupied, leaving  $3z^2 - r^2$



**Figure 7.5** GGA +  $U$  DOS projected onto Fe- $d$  (minority spin channel) (left panel) and V- $d$  (majority spin channel) (right panel) states for HT-T (top panel) and LT-T (bottom panel). The conventions of different line styles are the same as in Fig. 7.4

states completely empty. This leads to a ferro-orbital ordering of  $x^2 - y^2$  type with the hole residing in the  $x^2 - y^2$  orbital in the HT-T case and of  $3z^2 - r^2$  with the hole residing in the  $3z^2 - r^2$  orbital in the LT-T case, as shown in Fig. 7.6.

The low-energy states of V- $d$  GGA+ $U$  DOS show the major peaks corresponding to the mixed  $t_{2g}$  states,  $|1\rangle, |2\rangle$  and  $|3\rangle$ , which get filled by two  $d$  electrons of V. The corresponding orbital ordering at the V site is shown in Fig. 7.7. This ordering looks very similar to what we find in case of  $\text{MnV}_2\text{O}_4$  (see Fig. 3.5). Like  $\text{MnV}_2\text{O}_4$ , in case of  $\text{FeV}_2\text{O}_4$  also, it represents a ferro-orbital ordering with formation of orbital chains in which the orbital rotates from one site to another both between and within the chain. Our calculations show that the rotation of orbital happens due to the presence of a co-operative type of local trigonal distortion at the V site, which we find in case of  $\text{MnV}_2\text{O}_4$  also.

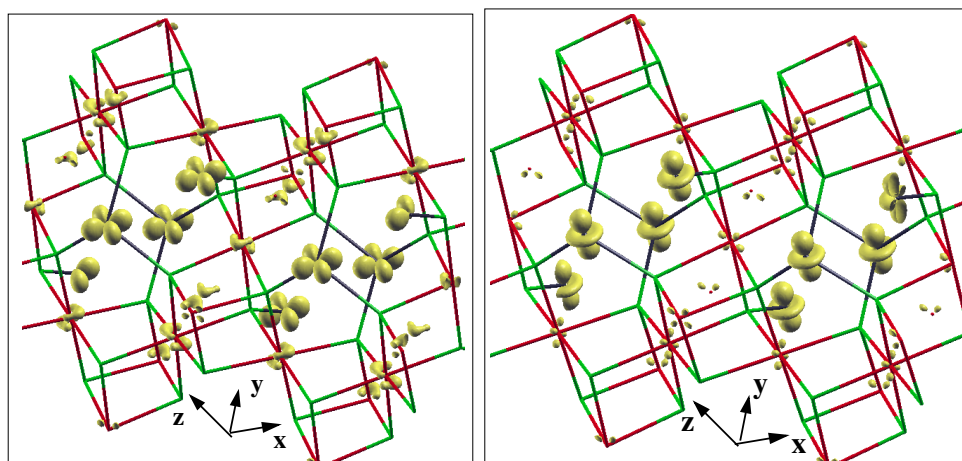


**Figure 7.6** The plot of charge density calculated within GGA +  $U$ , demonstrating the orbital ordering at the Fe site for HT-T (left panel) and LT-T (right panel).

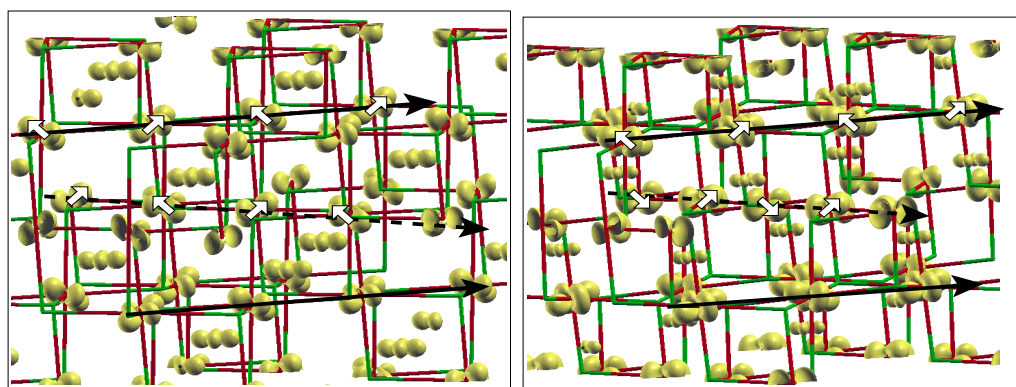


**Figure 7.7** The plot of charge density calculated within GGA +  $U$ , demonstrating the orbital ordering at the V site for HT-T (left panel) and LT-T (right panel). The arrows mark the rotation of the orbitals as one moves to neighbouring V sites within a given orbital chain, while the solid and dashed lines mark the orbital chains.

#### 7.4.4 Spin-Orbit interaction

The spin-orbit coupling (SOC) has been often considered to play an important role in orbital ordering in spinel compounds[13]. It has been seen that SOC within the  $t_{2g}$  manifold produces orbital polarization for  $t_{2g}^n$  configurations with  $n = 1, 2, 4, 5$  [14]. For V-based spinel compounds like  $\text{MnV}_2\text{O}_4$  with two

electrons in the  $t_{2g}$  manifold, the orbital moment is found to be significant in our calculation. The counterintuitive and rather large orbital moment has been reported for  $e$  levels of Fe in  $\text{FeCr}_2\text{S}_4$ . We explain that this happens through coupling with empty Fe  $t_2$  orbitals. Therefore, in order to probe the effect of SOC, we carried out GGA +  $U$  + SO calculations. The orbital moments at the Fe site are found to be  $\sim 0.11-0.12 \mu_B$  pointed in the same direction as the spin moment of magnitude  $\sim 3.4-3.5 \mu_B$ , while that at V site is found to be  $\sim 0.09-0.1 \mu_B$  directed in the opposite direction of the spin moment of magnitude  $\sim 1.6-1.7 \mu_B$ . This is in agreement with more than half-filled and less than half-filled  $d$  occupancies of Fe and V, respectively. Since our calculation shows significant orbital moments at both Fe and V sites, we investigate the possible role of SOC in the structural aspects. For this purpose, we carried out GGA +  $U$  + SO calculations considering tetragonal structures of varied  $c/a$  ratios, from values less than 1 to values greater than 1. For each  $c/a$  ratio, all the atomic positions as well as volume are optimized. Two sets of calculations are carried out, one with the spin quantization axis pointed along the [001] direction and another with the spin quantization axis pointed along the [110] direction. The result of these several optimization calculations is summarized in Fig. 7.8. It should be noted that calculated total energies at  $T = 0$  K showed the  $c/a > 1$  structure to be more stable with spin quantization axis pointed along the [001] direction compared to the  $c/a < 1$  structure with spin quantization axis pointed along the [110] direction by about 10 meV/f.u.

Interestingly, we find that while  $c/a < 1$  is favored with the spin quantization axis pointed along the [110] direction, beyond a critical value of  $c/a$ , which turns out to be 1.016,  $c/a > 1$  is favored with the spin quantization axis pointed along the [001] direction. In addition to this, the  $c/a > 1$  structure does contain elongated  $\text{FeO}_4$  tetrahedral units and compressed  $\text{VO}_6$  octahedral units, as shown in the inset of Fig. 7.8, similar to experimental observation. This leads to a situation where the single-ion anisotropy influences the shape of the solid. This kind of effect has been observed recently in rare-earth-based magnetic shape memory (MSM) materials like  $\text{RCu}_2$  ( $R$ =rare earth)[15]. There the single-ion anisotropy-driven effect is operative even in the paramagnetic phase. Therefore we expect this phenomenon to be operative for the HT-T phase of  $\text{FeV}_2\text{O}_4$ . In our calculations, the single-ion anisotropy at the Fe site in  $\text{FeCr}_2\text{S}_4$ , is found to be in plane while that of the V site in  $\text{MnV}_2\text{O}_4$  is found

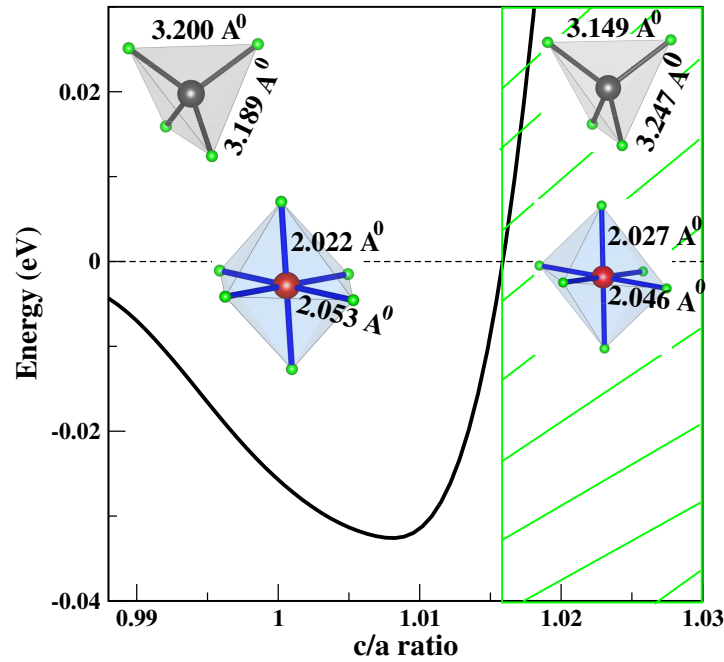


**Figure 7.8** The difference of GGA +  $U$  + SO energies, with spin quantization axis pointed along [110] and [001], plotted for various  $c/a$  ratios. The  $\text{VO}_6$  and  $\text{FeO}_4$  units of the optimized structures for  $c/a = 0.99$  and  $c/a = 1.02$  are shown in the unhatched and hatched regions, respectively.

to be out of plane. The interplay of the single-ion anisotropies of Fe and V, which gets influenced by the magnetic exchange between Fe and V below  $T_c$ , leads to change in the overall spin quantization axis from in plane to out of plane in moving from HT to LT and subsequent change in the shape. The change of structure therefore is caused by the change in the direction of magnetic anisotropy from in plane to out of plane, helped by the setting up of magnetic exchange between Fe and V, introducing a somewhat different mechanism of magnetostriction than in commonly known examples. It is worth to mention that the single-ion anisotropy-driven rare-earth MSM materials have been reported in literature[15] to exhibit giant magnetostrain of the order of 1%. Interestingly a similar effect has been also reported for  $\text{FeV}_2\text{O}_4$ [7].

## 7.5 Conclusion

Using DFT calculations we have investigated the orbital ordering in  $\text{FeV}_2\text{O}_4$ , which contains both orbitally active A and B sites. usually the spinel compounds with single site which posses orbital degree of freedom, exhibits single tetragonal phase. In contrast to those compounds, this compound is reported to show two tetragonal phases, one compressed at high temperature and another elongated at low temperature. We find that the orbital ordering at the Fe site is a ferro-orbital ordering of the  $x^2 - y^2$  kind at high temperature and of the  $3z^2 - r^2$  kind at low temperature. On the other hand, at the V site it forms orbitally ordered chains driven by staggered trigonal distortion. We further find that the spin quantization axis pointed along the [110] direction is favored for compressed tetragonal shapes, while beyond a critical value of  $c/a$  with elongated tetragonal shape the spin quantization axis pointed along the [001] direction is favored. The switching of overall magnetocrystalline anisotropy from out of plane to in plane below  $T_c$  therefore causes a change in the shape of the tetragonal unit cell.

# Bibliography

- [1] P. G. Radaelli, *New Journal of Physics* **7**, 53 (2005).
- [2] S. Sarkar, T. Maitra, R. Valentí, and T. Saha-Dasgupta, *Phys. Rev. Lett.* **102**, 216405 (2009).
- [3] T. Maitra and R. Valentí, *Phys. Rev. Lett.* **99**, 126401 (2007).
- [4] N. Büttgen, J. Hemberger, V. Fritsch, A. Krimmel, M. Mücksch, H.-A. K. von Nidda, P. Lunkenheimer, R. Fichtl, V. Tsurkan, and A. Loidl, *New Journal of Physics* **6**, 191 (2004).
- [5] A. Wold, R. J. Arnott, E. Whipple, and J. B. Goodenough, *Journal of Applied Physics* **34**, 1085–1086 (1963).
- [6] M. Tanaka, T. Tokoro, and Y. Aiyama, *Journal of the Physical Society of Japan* **21**, 262–267 (1966).
- [7] T. Katsufuji, T. Suzuki, H. Takei, M. Shingu, K. Kato, K. Osaka, M. Takata, H. Sagayama, and T. hisa Arima, *Journal of the Physical Society of Japan* **77**, 053708 (2008).
- [8] P. J. Wojtowicz, *Phys. Rev.* **116**, 32–45 (1959).
- [9] R. Tackett, G. Lawes, B. C. Melot, M. Grossman, E. S. Toberer, and R. Seshadri, *Phys. Rev. B* **76**, 024409 (2007).
- [10] Z. Szotek, W. M. Temmerman, D. Ködderitzsch, A. Svane, L. Petit, and H. Winter, *Phys. Rev. B* **74**, 174431 (2006).

- 
- [11] G. Giovannetti *et al.*, Phys. Rev. B **83**, 060402 (2011).
- [12] V. I. Anisimov, I. V. Solovyev, M. A. Korotin, M. T. Czyżyk, and G. A. Sawatzky, Phys. Rev. B **48**, 16929–16934 (1993).
- [13] O. Tchernyshyov, Phys. Rev. Lett. **93**, 157206 (2004).
- [14] C. Jia, S. Onoda, N. Nagaosa, and J. H. Han, Phys. Rev. B **76**, 144424 (2007).
- [15] S. Raasch, M. Doerr, A. Kreyssig, M. Loewenhaupt, M. Rotter, and J.-U. Hoffmann, Phys. Rev. B **73**, 064402 (2006).

## Chapter 8

# Conclusion and scope for future study

The aim of this thesis was to study of microscopic origin of many exciting and intriguing physical properties of different spinel compounds via first-principles calculations. In chapter 3-7, we have considered five different spinel compounds, which exhibit different interesting properties, due to the orbital activity of either of A-site or B-site or both ion. In each chapter, the individual summary of results and discussions have been presented at the end. In this chapter we shall summarize the important results that emerge out from our calculations on each of the five spinel compounds, namely  $\text{MnV}_2\text{O}_4$ ,  $\text{FeCr}_2\text{S}_4$ ,  $\text{FeSc}_2\text{S}_4$ ,  $\text{CuIr}_2\text{S}_4$  and  $\text{FeV}_2\text{O}_4$ .

### 8.1 Conclusion

**$\text{MnV}_2\text{O}_4$**  : The nature of the orbital ordering in  $\text{MnV}_2\text{O}_4$  is closely associated with the structural transition exhibited by this compound. The geometry optimization calculation shows a strong influence of correlation effects in the choice of the correct low temperature structure of this compound. The orbital ordering at V site follow the site symmetry of vanadium which is four-fold rotation times inversion to give rise to orbital chains with orbitals rotated with respect to each other both within and between the chains. V-V magnetic exchange has been computed which are in good agreement with experimental results and this provides an explanation of the controversy between antiferro-orbital ordering versus

the strong exchange between the orbital chains [1]. We further show that our proposed orbital ordering is capable of predicting correctly the non-collinear spin structure as observed experimentally[2].

**FeCr<sub>2</sub>S<sub>4</sub> :** Our study shows that low temperature insulating state of FeCr<sub>2</sub>S<sub>4</sub> is driven by spin-orbit coupling operative within Fe *e* states which gets renormalized in presence of Coulomb correlation. This adds FeCr<sub>2</sub>S<sub>4</sub> to the list of compounds exhibiting Coulomb enhanced spin-orbit coupling[3, 4]. The possible role of low-temperature structural distortion of this sulphide spinel has been explored. Our total-energy calculation shows tendency of both S and Cr movements in the low temperature phase of FeCr<sub>2</sub>S<sub>4</sub>. Comparison of calculated reflectivity spectrum with experimentally measured data [5] shows improved agreement in the mid infra-red regime upon inclusion of the structural distortion.

**FeSc<sub>2</sub>S<sub>4</sub> :** FeSc<sub>2</sub>S<sub>4</sub> and FeCr<sub>2</sub>S<sub>4</sub>, these two spinel compounds are exactly same in their chemical composition and structure except the presence of different chemical elements at the B-site. Nevertheless, they behave very differently. Our study reveals that this difference in behaviour originates from the difference in the hybridization between Fe *d* states and B (B=Cr/Sc) *d* states and S *p* states. This not only affects the magnitude of magnetic exchanges but also the relative importance of different magnetic exchanges. Moreover, it turns out that the *J*'s are antiferromagnetic for the Sc systems and ferromagnetic for the Cr system. This leads to important frustration effects in the Sc compound which are absent in the Cr compound [6].

**CuIr<sub>2</sub>S<sub>4</sub> :** There exist two different school of thoughts regarding the mechanism of metal to insulator transition of CuIr<sub>2</sub>S<sub>4</sub> at low temperature. Croft *et. al.* [7] has explained it in terms of formation of correlated spin singlet dimers. There exists an alternative explanation of this metal to insulator transition, proposed by Khomskii and Mizokawa,[8] in terms of the orbitally driven *Peierls* state. Our first-principles study finds that correlation has very less effect on this metal to insulator transition observed in this spinel compound. The transition from high temperature to low temperature crystal structure with complex ordering pattern, therefore, may be rationalized in terms of formation of one-dimensional bands which gives rise to an orbitally driven *Peierls* state.

**FeV<sub>2</sub>O<sub>4</sub> :** FeV<sub>2</sub>O<sub>4</sub>, the last one of the five spinel compounds we have studied, is special in the sense that it posses orbitally active ion at both A-site and B-site. Previously we have studied spinel compounds with orbitally active ion at either B-site (MnV<sub>2</sub>O<sub>4</sub>) or A-site (FeCr<sub>2</sub>S<sub>4</sub>). In addition, this compound is reported to show two tetragonal phases, one compressed at high temperature and another elongated at low temperature. We find that the orbital ordering at the Fe site is a ferro-orbital ordering of the  $x^2 - y^2$  kind at high temperature and of the  $3z^2 - r^2$  kind at low temperature. On the other hand, at the V site it forms orbitally ordered chains driven by staggered trigonal distortion, very similar to what we have seen in case on MnV<sub>2</sub>O<sub>4</sub>. We find that the single-ion anisotropy effect with hard and easy  $c$  axis favours the compressed and elongated tetrahedral shapes, which gives rise to magnetocrystalline anisotropy-dependent shape changes, similar to that reported in the context of rare-earth-based magnetic shape memory alloys [9].

## 8.2 Scope for future work

Spinel compounds exhibiting many fascinating and intriguing properties, form an active field of research in material science for the last few decades. Microscopic understanding of these complex phenomena, involving several degrees of freedom, not only shed light on the underlying physics, but also helps in search for new materials with desired functional properties. In this present thesis, we have studied few of the relevant compounds, out of the vast field of spinel compounds. This dissertation covers very little, yet important part of this vast field. In all reality, this is just touching the tip of the iceberg. There are few issues concerning the spinel compounds we have studied which can be taken up for further studies. Here we list few of such possibilities which can be considered as a future continuation of the present study.

- In our analysis of comparative study of FeCr<sub>2</sub>S<sub>4</sub> and FeSc<sub>2</sub>S<sub>4</sub>, we have not considered the effect of Jahn-Teller (JT) interactions. It should be mentioned that crystallographically no signature for static JT order has been found in these systems. In spite of that there could be dynamic JT effects. This could be a interesting topic for future work.

- While estimating the band gap of low temperature structure of  $\text{CuIr}_2\text{S}_4$ , it has been seen that gap value is sensitive on the structural details. Due to the low symmetry and large unit cell of  $\text{CuIr}_2\text{S}_4$  at low temperature, structural optimization was hindered. With the advancement of computer power, structural optimization can be taken up as a future project.
- Many of interesting properties of spinel compound have been studied through model calculations, which can provide a qualitative understanding of those complex phenomena in a semi-classical approach. For example, the metal-insulator transitions exhibited by a number of spinel compounds with partially filled  $t_{2g}$  orbitals at B-site, can be explained as orbitally driven *Peierls* instabilities. The possibility of formation of such orbitally driven states has been studied within a simplified theoretical model, a two-dimensional checker-board lattice<sup>†</sup> with two orbitals per atomic site[10]. Orbital ordering and inter-atom electron-phonon interactions have been treated self-consistently within a semi-classical approximation, and onsite intra-orbital and inter-orbital electron-electron interactions are treated at the Hartree-Fock level. A stable, orbitally induced Peierls bond-dimerized state for carrier concentration of one electron per atom has been found. The Peierls bond distortion pattern continues to be period two bond dimerization even when the charge density in the orbitals forming the one-dimensional band is significantly smaller than 1. Interestingly, it has been found that for carrier density of half an electron per atom the Peierls instability is absent within one-electron theory as well as mean-field theory of electron-electron interactions, even for nearly complete orbital ordering. Similar kind of calculation can be carried out to model the orbital ordering of  $\text{FeV}_2\text{O}_4$ , where both A and B site contains orbitally active ion.

---

<sup>†</sup>Projection of B-site only sub-lattice of spinel compound, on to either of crystallographic planes gives rise to checker-board pattern. See Fig. 1.2

# Bibliography

- [1] J.-H. Chung, J.-H. Kim, S.-H. Lee, T. J. Sato, T. Suzuki, M. Katsumura, and T. Katsufuji, *Phys. Rev. B* **77**, 054412 (2008).
- [2] V. O. Garlea, R. Jin, D. Mandrus, B. Roessli, Q. Huang, M. Miller, A. J. Schultz, and S. E. Nagler, *Phys. Rev. Lett.* **100**, 066404 (2008).
- [3] H. J. Xiang and M.-H. Whangbo, *Phys. Rev. B* **75**, 052407 (2007).
- [4] G.-Q. Liu, V. N. Antonov, O. Jepsen, and O. K. Andersen., *Phys. Rev. Lett.* **101**, 026408 (2008).
- [5] K. Ohgushi, Y. Okimoto, T. Ogasawara, S. Miyasaka, and Y. Tokura, *Journal of the Physical Society of Japan* **77**, 034713 (2008).
- [6] N. Büttgen, J. Hemberger, V. Fritsch, A. Krimmel, M. Mücksch, H.-A. K. von Nidda, P. Lunkenheimer, R. Fichtl, V. Tsurkan, and A. Loidl, *New Journal of Physics* **6**, 191 (2004).
- [7] M. Croft, W. Caliebe, H. Woo, T. A. Tyson, D. Sills, Y. S. Hor, S.-W. Cheong, V. Kiryukhin, and S.-J. Oh, *Phys. Rev. B* **67**, 201102 (2003).
- [8] D. I. Khomskii and T. Mizokawa, *Phys. Rev. Lett.* **94**, 156402 (2005).
- [9] S. Raasch, M. Doerr, A. Kreyssig, M. Loewenhaupt, M. Rotter, and J.-U. Hoffmann, *Phys. Rev. B* **73**, 064402 (2006).
- [10] R. T. Clay, H. Li, S. Sarkar, S. Mazumdar, and T. Saha-Dasgupta, *Phys. Rev. B* **82**, 035108 (2010).